Lehrstuhl für Akustik Mobiler Systeme

Flexible Multi-Body Simulation of a Complex Rotor System Using 3D Solid Finite Elements

Theo Fabian Kiesel

Vollständiger Abdruck der von der Fakultät für Maschinenwesen der Technischen Universität München zur Erlangung des akademischen Grades eines

Doktor-Ingenieurs (Dr.-Ing.)

genehmigten Dissertation.

Vorsitzender:	Prof. dr.ir. Daniel J. Rixen
Prüfer der Dissertation:	1. Prof. Dr.-Ing. Steffen Marburg
	2. Prof. Sergio De Rosa

Die Dissertation wurde am 12.06.2017 bei der Technischen Universität München eingereicht und durch die Fakultät für Maschinenwesen am 14.11.2017 angenommen.

Acknowledgements

The present thesis is the outcome of an industrial PhD project of the Chair of Vibro-Acoustics of Vehicles and Machines of the Technical University of Munich in cooperation with the Hilti Group, where I worked as a development engineer at that time.

During the project, I was supported by many wonderful people, and I am deeply obliged to them. First of all, I would like to thank my wife Irina for her unconditional love and support. Without her, I would never have been able to finish the task.

On the universitarian side, I am deeply grateful to my supervisor, Prof. Dr.-Ing. Steffen Marburg, who not just guided me on my way with unparalleled commitment, but who became a mentor to me in many ways. I would like to express my sincere gratitude to Prof. Sergio De Rosa from the University of Naples Frederico II, who took on the role of being the second examiner, who traveled from the shores of southern Italy to Munich in the depth of winter, and who provided me with reassurance and swiftness, when I desperately needed it. Many thanks go to Prof. dr.ir. Daniel J. Rixen for being the chairman at my doctoral exam. With my fellow research associates Patrick Langer, Markus Mäder, Christian Geweth, Lennart Moheit, Magdalena Scholz, Ferina Saati Khosroshahi, and Johannes Henneberg, I shared many expert discussions, as well as beer and friendship.

On Hilti's side, I am especially grateful to Uta Renneberg and Josef Obermeier, who made the contractual setup possible in the first place. I thank my managers Dr. Andrés Wellmann Jelic and Lars Melzer, who gave me enough freedom for academic research. The team surrounding Martin Lammersköter and Oliver Koslowski provided me with outstanding support regarding the application example of this thesis. I am especially thankful to my colleagues and friends Quirin Wahle, Helene Kaps, Ali Shadavakhsh, Marianna Vivolo, and Michael Götzfried, who did not abandon me, even when I was banned to the deepest cellar. The same applies to my external colleagues Raf Delen and Dominiek Sacré from Siemens, as well as to Olivier Kirten from Kraken Engineering. My research profited greatly from our discussions, as well as from Tripel Karmeliet and Leonidas, but I will say no more than: what happened in the cellar shall remain in the cellar.

Finally, I thank Linkin Park for providing me with enough energy to stay awake during the night shifts.

Munich, December 2017

Abstract

Upon the emergence of general-purpose FE-codes in the 1980s, 3D solid modeling became widely available and can by now be considered as a standard approach in the mechanical design verification of stationary structures. With regard to rotordynamics, however, implementation of FEM is lagging behind, and beam-element models are still widely in use. Beam-models are compact and come at reasonable computational costs, yet they are afflicted with a number of limitations, making them insufficient for the analysis of more complex rotor systems.

The current thesis investigates the question of whether general-purpose FE-codes currently offer sufficient capabilities to perform challenging rotordynamic analyses. The research is carried out on a special industrial diamond coring system acting as an application example. It is a two-level rotor system in which the inner subsystem is not only spinning around its axis of rotation, but, in addition, performs an overlayed tumbling motion to increase drilling performance. Due to the complex mechanical design, nonlinear characteristics and the fact that it is operated hand-held, the coring system already provides a challenge with regard to rotordynamics in its serial configuration. For the purpose of academic research, the system is further modified to intentionally exceed the clamping force in the force-locked connection between core bit and driving shaft when running-up the system through a bending resonance. Exceeding the clamping force during operation results in strong nonlinear effects and finally produces a mode-locking phenomenon in which the core bit performs a relative motion inside the supporting chuck in order to stay in resonance, even if the rotational speed no longer matches the original frequency of the bending resonance. Due to the complex geometry of the interacting parts, such a system cannot be represented by beam-element models, but rather requires 3D solid modeling.

ABAQUS is used as a representative example for a general purpose FE-code to construct a flexible multi-body simulation using 3D solid finite elements. Extensive experimental investigations provide the basis to validate and update the model. The comparison to simulation results show good consistency, and even the mode-locking phenomenon is well represented by the model.

Contents

List of Figures

List of Tables

List of Symbols

$[]'$	in reference to a co-rotating coordinate system
$[]^c$	in reference to a coordinate system fixed to the center of gravity and aligned with the body's principal axes of inertia
$[]_r$	reduced system (subspace projection)
$[a]$	normalized acceleration
$[d]$	normalized displacement
$[f]$	normalized frequency
$[F]$	normalized force
$[r]$	normalized rotational speed
$[T]$	normalized torque
[Meas]	indicating measurement data
[Sim]	indicating simulation results
$\mathbf{A}$	real matrix (state space representation)
A_{res}	substitutive area of the pressure cone
a	material-specific constant
$\mathbf{B}$	real matrix (state space representation)
b	a constant
$\mathbf{C}$	matrix of Coriolis forces
c	a constant
$\mathbf{D}$	damping matrix
D_1	outside diameter of outer bearing ring
D_2	inside diameter of inner bearing ring
D_h	basic housing bore
D_s	basic shaft diameter
d_2	thread pitch diameter
d_h	diameter of through hole
d_k	effective diameter of friction in the screw head pad
d_{res}	substitutive diameter of the pressure cone
d_w	head contact diameter of the bolt
$\mathbf{E}$	modulus of elasticity
$\mathbf{F}$	external force vector
F_{VM}	clamping force in a screw connection due to a tightening torque
$\mathbf{F}_\Omega$	centrifugal force vector

$\mathbf{G}$	gyroscopic matrix
$\mathbf{I}$	inertia tensor
$\mathbf{I}$	interference
$\mathbf{K}$	stiffness matrix
$\mathbf{K}_S$	spin-softening effect due to centrifugal forces
$\mathbf{K}_\Omega$	geometric stiffness matrix
$\mathbf{L}$	angular momentum
l_k	clamped depth of the two parts
$\mathbf{M}$	mass matrix
m_e	rotor mass
$\mathbf{N}$	circulatory matrix in reference to an inertial frame
n	ratio between rotational speed of shaft and tumble sleeve
P_d	nominal radial bearing clearance before mounting
$\mathbf{q}$	displacement vector of generalized coordinates
$\mathbf{T}$	vector of external moments
T_A	tightening torque
T_C	frictional drag torque
T_d	overall drag torque
T_Ω	speed-dependent drag torque
t	time
$\mathbf{U}$	vector of imbalance forces
$\mathbf{z}$	state vector

α	thread pitch angle
Δ_h	clearance reduction due to press-fitting of bearing in housing
Δ_s	clearance reduction due to press-fitting of bearing on shaft
Δ_t	time increment
ΔP_d	reduction of bearing clearance due to mounting
ϵ	eccentricity
$\boldsymbol{\lambda}$	eigenvalues
$\boldsymbol{\lambda}_s$	eigenvalues (state space representation)
μ_k	coefficient of friction of the support area
σ'	thread angle of friction
φ	tumble angle

$\boldsymbol{\phi}^R$	eigenvector of subspace-projected system
$\boldsymbol{\varphi}^R$	eigenvector
ξ	Poisson's ratio
$\boldsymbol{\psi}^R$	eigenvector (state space representation)
$\boldsymbol{\Omega}$	angular velocity vector
Ω_0	spin speed
ω	undamped natural angular frequency

List of Acronyms

1D	One-Dimensional
2D	Two-Dimensional
3D	Three-Dimensional
AIAA	American Institute of Aeronautics and Astronautics
CAD	Computer Aided Design
CAE	Computer Aided Engineering
EMA	Experimental Modal Analysis
DIN	Deutsche Industrienorm (German Industrial Standard)
DOF	Degree of Freedom
FE	Finite Element
FEM	Finite Element Method
HHT	Hilber-Hughes-Taylor
ISO	International Organization for Standardization
MBS	Multi-Body Simulation
MIF	Mode Indicator Function
MPC	Multi-Point Constraint

1 Introduction

1.1 Motivation

Across all industries, engineers experience increasing pressure to shorten development time, while product complexity simultaneously increases due to customers demanding innovation or as a consequence of variant diversity accompanying a global, multi-market strategy. Under such circumstances, verification of the mechanical design purely by building physical prototypes and testing them for lifetime in a so-called "make & break" approach is out of the question, as it costs too much time and money. With the rise of computer-aided engineering (CAE), nowadays significant parts of the verification process can be done in a virtual environment before going into hardware. Many companies share a common vision in which only one physical prototype is needed at the end of the development process, with the sole objective of confirming the design obtained in previous virtual loops. Accurate and efficient CAE techniques are the prerequisites for this vision to come true.

At present, the finite element method (FEM) is the most accepted and widely used virtual prototyping tool [155]. Since its development in the 1950s, FEM has become a standard procedure for solving practical engineering problems in virtually every field of engineering analysis [6]. With regard to structural dynamics, FEM offers systematic rules for the discretization of geometrically complex structures and for the solution of the underlying differential equations. In many industries, FEM has developed into a key indispensable technology for the modeling and simulation of mechanical systems [87].

With regard to rotordynamcis, however, the implementation of FEM is lagging behind the progression in other fields [113]. While today stationary structures are usually modeled using 3D continuum finite elements, the standard approach in rotordynamics still consists of using beam-element models [37], referred to by some authors as *shaft-line models* [33]. This is a linearized, 1D approach in which the rotor system is separated into a "shaft", which is represented by finite beam-elements, and into one or more "disks", which are considered rigid and which are represented in the model as point masses with inertia properties to account for the gyroscopic effects. The name arises from the process of generating the mesh by placing nodes along the shaft line. Spring elements and joints can be attached to the nodes to account for elastic bearing or stator behavior. Such models represent a great improvement compared to classical Jeffcott rotor models, which simply divide a rotor system into a massless, elastic shaft and a (single) rigid disk.

For a rough estimation in the early conceptual design phase, shaft-line models might be sufficient, providing the advantages of intuitive geometric interpretation and low computational costs. The necessary simplifications, however, render such models unfit for final verification of the mechanical design in the case of most real-world rotor systems. Limitations of shaft-line models will be discussed more detailed in Chapter 2.3 of the current thesis. In brief, shaft-line models are afflicted by the following shortcomings:

- Lack of accuracy in mathematical model representation: Regardless of the underlying beam theory, finite beam elements assume the shaft's cross-section to remain fixed and plain in deformed configuration. This assumption is violated at sections with sudden changes in diameter, such as bearing seats [119, 128, 142].
- Lack of physical model representation: First, it is a 1D approach, therefore it does not couple the lateral with the torsional and axial behavior of the rotor. It is well known, that large bending vibrations lead to torsional excitation [90], while, on the other hand, fluctuation in the driving torque can cause lateral instability of the rotor [100]. Second, the stiffening effect of the disk on the shaft and vice versa is ignored. Generally, representing a rotor system as an elastic shaft with attached rigid disks is an oversimplification that cannot correctly describe many real-world rotors. Third, the approach represents a partial linearization that cannot represent centrifugal stiffening or spin-softening effects [41, 98, 99].
- High effort generating the model: Virtual prototyping is based on three-dimensional CAD-data. One of the main advantages of 3D solid FE-models is the fact that already existing geometric models can be reused for generating the mesh. This is in contrast to shaft-line models, in which the model needs to be created manually by representing the different axial sections of a rotor by finite beam-elements that correctly describe its length and diameter, or the shape of the cross-section, respectively. Over the years, beam-elements have been developed for typical shapes, i.e. circular, conical, hollow or rectangular. At rotor sections corresponding exactly to such "standard" shapes, model generation is straightforward. Real-world rotors, however, will always contain sections that do not resemble such simple geometric forms. For instance, these sections can be found at feather key connections to enable torque transfer to mounting parts, at interfaces to adjacent parts or at gear wheels. Here, the real geometry needs to be approximated by a standard form. For instance, a section containing a keyway in an otherwise circular cross-section can be represented by beam-elements with a purely circular cross-section in which the diameter is reduced until the bending stiffness

is correctly met. Adjusting the model typically requires specific and labor-intensive computations that are not easily automated [41].

In an environment of high labor costs and time being a crucial factor, it is especially the last of the aforementioned drawbacks that counts against a shaft-line model. The effort of manual model creation and adjustment should not be underestimated. When dealing with more complex systems, it might become necessary to set up a detailed 3D solid FE model with the sole purpose of validating the shaft-line model in non-rotating condition, i.e. [5, 56, 86, 92]. On the other hand, in many cases a 3D model is required anyway to perform a lifetime calculation, which cannot be delivered by a shaft-line model. Either way, it leads to a situation in which two different models of the same rotor system are created. Figure 1.1 visualizes the interaction of the two models described in what follows: The major purpose of the shaft-line model is to ensure functionality of the rotor system. Typically, one is interested in critical rotor speeds, bearing forces and the maximal deflection of the rotor to make sure there is no contact to the stator in any operational condition. Generally speaking, the focus of interest lies on the global behavior of the rotor system. Apart from ensuring functionality, design verification also contains lifetime prediction. This is done under the use of a 3D solid FE model, in which the focus of interest lies on local stress distribution instead of global behavior. The 3D model does not contain the actual rotation of the rotor system, but receives the necessary load cases from the shaft-line model in order to perform a static calculation. If one of the two models indicates a necessary design change, both models need to be updated, the shaft line model needs to be validated anew, and the procedure starts over again. Since the two models are usually implemented using two different software programs, often operated by different persons, the whole procedure is not only very time consuming, but also prone to errors. This gives rise to the question, why not use a single model for each task, functionality and lifetime? This would have to be the 3D model, since a shaft-line model is unable to deliver the local stress distribution needed for lifetime prediction of complex real-world geometries.

1.2 Current State of Knowledge

The following section presents a brief overview of the current state of knowledge regarding the use of 3D solid FE-models for rotordynamics. The topic will be discussed more in-depth in the theory part of the current thesis.

In the 1980s, 3D solid modeling became generally available by the emergence of commercial,

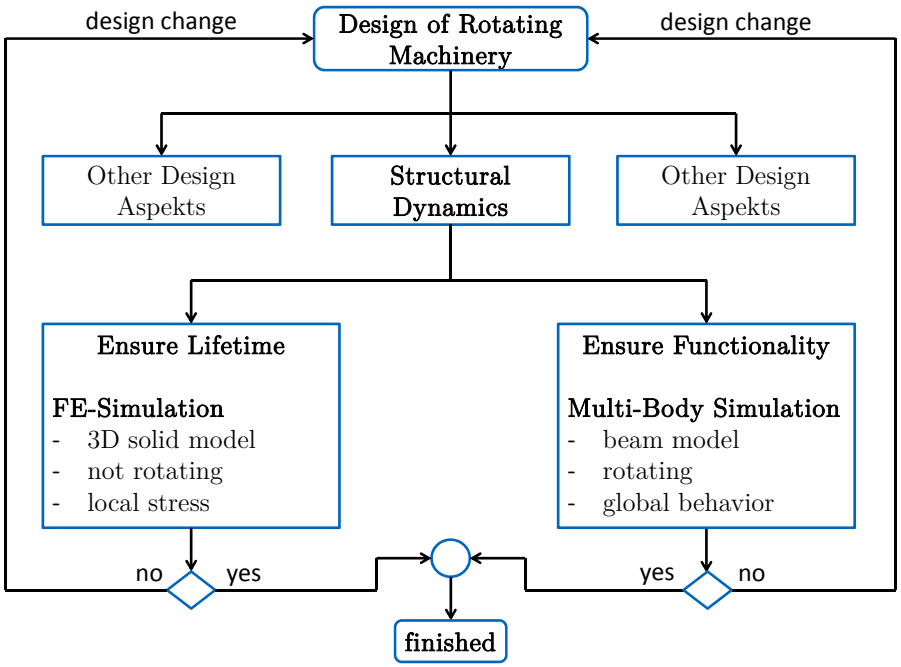

Figure 1.1: Flow chart of interaction between FEM and MBS in the design process of rotating machinery

general purpose FE-codes such as ANSYS, ABAQUS and NASTRAN [88, 126]. The reasons why 3D solid modeling has not yet prevailed in rotordynamcis are multilayered and range from limited computational resources to a lack of adequate computational solution techniques and mathematical element formulations. In general, rotordynamic problems can be solved in the time or in the frequency domain, depending on the specific problem. Through direct time integration of the underlying equations of force equilibrium, a model consisting of 3D continuum finite elements is automatically capable of taking into account rotordynamic effects, such as gyroscopic coupling, stress stiffening due to centrifugal forces or even non-axial symmetry of the rotating parts. When solving the equation of motion in the frequency domain, those effects need to be accounted for by additions to the finite element formulations.

When direct time integration was first used to solve FE-models of rotating systems in the 1970s, researches where surprised of the downright ridiculous small time steps necessary to ensure numerical stability [65, 66, 72, 73]. One of the reasons for this is that the used integration schemes did not contain artificial numerical damping, therefore the number of elements dictate the critical time step. Typically, such a determined upper border is several orders smaller in magnitude than would be expected from the frequency range of interest, thereby significantly slowing down the solution procedure [17]. Moreover, those early models

did not even contain 3D finite elements, but rather consisted of axisymmetric, massless beam-elements and corresponding lumped masses. Still, the lack in computational power limited the number of elements down to no more than a few dozen until even the nineties. Therefore, the use of 3D solid models for rotordynamic problems that require a solution through direct time integration was long out of question, and most research was directed on solutions in the frequency domain and on model reduction, or more generally speaking, on solutions with lower computational costs [145]. Since the first steps in using direct time integration for rotordynamic problems, however, things have changed significantly: First, the reasons for numerical instabilities of rotating systems are much better understood [111], and general purpose FE-codes are nowadays equipped with efficiently implemented time-integration algorithms that provide the necessary numerical damping, such as the *Hilber-Hughes-Taylor method* (HHT method) [55] and the so-called *Generalized-α method* [18]. Second, in accordance with *Moore's Law* [120], computational power has grown exponentially over the last decades and by now rates several dimensions higher than in the early years of noteworthy computers. Nevertheless, the process of automatic mesh generation from three-dimensional CAD geometry as described above, leads to a large number of degrees of freedom (DOFs) even when measured with todays standards. Whether a model with a mesh fine enough to accurately predict local stress for life time calculation can also be used for a rotordynamic analysis remains to be seen in the further course of this thesis.

When solving the equations of motions of a rotating system in the frequency domain, the effects of gyroscopic couples are introduced in terms of a gyroscopic matrix when using a stationary coordinate system, and in terms of a matrix containing coriolis forces when using a co-rotating coordinate system. Although FEM dates back to the 1950s, it was not before 1976 that a gyroscopic matrix was first developed for finite beam elements by *Nelson* and *McVaugh* [102]. Since then, a large number of finite beam-elements fit for rotordynamic analysis have been developed based on different types of beam theory. It comes as no surprise that developing the necessary formulations for 3D finite elements is significantly more difficult, and it took until the beginning of the new millennium for the first steps to be laid by *Nandi* and *Neogy* [99]. Given the fact that for almost thirty years 3D solid modeling has been sought as the (metaphorically speaking) "Holy Grail of rotordynamics" [40], the number of publications following the pioneering works described above is surprisingly small. Considerable progress, however, can be observed in the rotordynamic capabilities of general purpose FE-codes. First, the necessary additions for rotordynamics were implemented in a rotating frame, since this turned out to be significantly less complex than in a stationary reference frame. The capabilities for using a stationary coordinate system have been added

only in the last couple of years, therefore the number of applications is still limited.

1.3 Objectives and Structure of this Thesis

The main objective is to investigate, whether general purpose FE-codes at present are capable of performing demanding rotordynamic analyses using a 3D solid modeling approach. The investigation is carried out on a special industrial diamond coring system which acts as an application example throughout the whole thesis. The diamond coring system is unique due to its kinematics that superimpose a tumbling movement on the spinning motion of the core bit in order to increase drilling performance. With regard to rotordynamics, this coring system already represents a challenge in its serial condition, since it contains complex mechanical design and shows highly non-linear system behavior. Within the underlying research, it has been strongly modified in order to create certain dynamic effects such as *mode-locking* that require the use of 3D solid modeling and cannot be addressed accurately by a shaft-line model. However, it must be clear that the effects outlined in the further course of this thesis are the result of heavy modifications to the serial product in order to provide the opportunity for academic research and do in no way occur in normal operation.

The structure of the thesis is as follows:

The theory part in **Chapter 2** first outlines how rotordynamic effects are represented in the equations of motion, and in turn, how this affects the requirements with regard to computational solution techniques. This is followed by an overview of the current state of knowledge regarding the use of FEM for rotordynamics and the capabilities of common general purpose FE-codes.

Chapter 3 outlines the diamond coring system which provides the application example of the current thesis. The focus of interest will be the crossing of a bending resonance when running up the tool, meaning transient behavior with regard to rotordynamics. The force-locked connection between the core bit and the actual power tool is of particular importance. For the purpose of academic research, the coring system will be modified (with regard to rotordynamics: intentionally "worsened"), i.e. by artificially increasing the imbalance of the core bit or by reducing the clamping force of the afore mentioned force-locked connection. The goal is to exceed the clamping force during run-up. This creates strong non-linear behavior and results in a *mode-locking* phenomenon, in which the core bit performs a relative motion inside its supporting chuck during run-up in order to stay in resonance, even if the rotational speed no longer matches the original frequency of the bending resonance. Another

challenge for simulation arises from the fact that the diamond coring system is operated hand-held, requiring one to represent the human operator in an adequate way.

Extensive experimental data provides the basis for evaluating the quality of the simulation model. **Chapter 4** explains the experimental setup and selected post-processing operations.

Chapter 5 introduces the simulation model of the diamond coring system. Although it is a comparatively small tool fit for hand-held operation, the mechanical complexity should not be underestimated, since it contains more than one-thousand individual parts. While in theory it is possible to fully represent every single part and the corresponding interactions in an FE-model, the modeling effort and the computational solution costs are neither acceptable nor necessary. With regard to the focus of interest being a run-up through the first bending resonance, the model approach chosen makes use of the multi-body capabilities of modern general purpose FE-codes: Parts that undergo elastic deformation during run-up are fully represented by a 3D solid FE-approach, while other parts that behave rigidly are considered lumped masses. The model is implemented in ABAQUS, which is not a special rotordynamic software but rather a general purpose FE-code. ABAQUS is chosen because it offers extensive multi-body capabilities as well as excellent contact algorithms. The latter are necessary to describe the relative motion of the core bit inside the force-locked chuck when the clamping force is intentionally exceeded during run-up to provoke mode-locking as described above.

Chapter 6 explains how experimental modal analysis (EMA) is used to validate and update the model representation of single components. EMA at non-rotating condition is also used to validate the model of the rotor system as a whole and to identify certain parameters such as damping introduced by the bearings or by the human operator.

Eventually, **Chapter 7** compares the simulation results of the run-up to measurement data. First, the global dynamic system behavior of the diamond coring system is introduced by using experimental data. This data provides the basis for identifying certain parameters that could not be acquired by measurements at non-rotating condition, as described in Chapter 6. The actual evaluation of the quality of the model is then performed regarding two cases: Initially for normal operation in which the clamping force of the force-locked chuck is sufficient to hold the core bit in place during run-up. The subsequent section deals with the case in which the clamping force is intentionally exceeded by reducing the pre-load, while at the same time artificially increasing the imbalance of the core bit or increasing the amount of the additional tumbling movement. When the clamping force is exceeded during run-up, the core bit performs a relative movement inside the chuck that is a combination of sliding and rolling, permanently changing the contact situation in the interface. The

experimentally observed mode-locking effect can only be represented by the model by taking into account the exact geometry of the interface between the chuck and the connecting end of the core bit, thereby requiring the use of 3D solid modeling.

1.4 Normalization of Data

The diamond coring system providing the basic hardware to act as an application example within this thesis is a serial product from an industrial manufacturer. The kinematics that superimpose a tumbling movement on the spinning motion of the core bit are unique on the market and create unrivaled drilling performance. To protect the manufacturer's expertise in this field, all data presented in this thesis are normalized towards certain reference values. The abbreviations used are shown in Table 1.1.

Table 1.1: Symbols of normalized quantities

symbol	normalized quantity
$[a]$	acceleration
$[d]$	displacement
$[f]$	frequency
$[F]$	force
$[r]$	rotational speed
$[T]$	torque

2 Selected Theoretical Foundations of Rotordynamics

The current chapter first outlines how rotordynamic effects are represented in the equations of motion, and, in turn, how this affects the requirements with regard to computational solution techniques. This is followed by an overview of the current state of knowledge regarding the use of FEM for rotordynamics and the capabilities of common general purpose FE-codes.

2.1 Equation of Motion

In rotordynamics, the equation of motion can be written in a stationary (inertial) coordinate system that is not rotating, or in a rotating coordinate system that is fixed to the spinning object. The choice between inertial and rotating frame depends on the properties of the rotor and its foundation, as will be explained in what follows when discussing the system matrices.

In the inertial frame, the equation of motion describing a discretized model of a rotor can be expressed in the following general form (i.e. [35, 37, 76, 90]):

$$\mathbf{M}\ddot{\mathbf{q}} + [\mathbf{D} + \mathbf{G}(\Omega)]\,\dot{\mathbf{q}} + [\mathbf{K} + \mathbf{N}(\Omega)]\,\mathbf{q} = \mathbf{F} \tag{2.1}$$

where $\mathbf{M}$ is the mass matrix, $\mathbf{D}$ is the damping matrix, $\mathbf{K}$ stands for the stiffness matrix. The influence of the gyroscopic forces are considered in matrix $\mathbf{G}$; matrix $\mathbf{N}$ represents the circulatory Matrix. Vector $\mathbf{F}$ describes the time-varying external forces, while vector $\mathbf{q}$ contains the translational displacements and (depending on the type of model) rotations of the generalized coordinates in reference to an inertial frame. With regard to Equation (2.1) one speaks of a representation in configuration-space, wherein the generalized coordinates define the configuration of a system, mathematically expressed by a system of n coupled second-order differential equations. This is in contrast to a state-space representation, which will be introduced in chapter 2.2.1, and wherein the configuration of a system is defined by a set of input, output and state variables, forming a set of of $2n$ first-order differential equations [91].

In the rotating frame, Equation (2.1) becomes:

$$\mathbf{M}'\ddot{\mathbf{q}}' + [\mathbf{D}' + \mathbf{C}(\Omega)]\,\dot{\mathbf{q}}' + [\mathbf{K}' + \mathbf{N}'(\Omega)]\,\mathbf{q}' = \mathbf{F}' \tag{2.2}$$

where **C** stands for the matrix containing the forces due to coriolis acceleration.

While the matrices M, D and K are fundamental to describe the dynamics of any oscillatory system, the circulatory matrix N and especially the gyroscopic matrix G, or C respectively, are a characteristic of a rotating system. In the further course of this chapter the system matrices will be described in order to point out some peculiarities that arise from rotation. Furthermore, the influence of certain physical parameters of the rotor system on the miscellaneous system matrices will be discussed. This is done, on the one hand, to explain the necessary capabilities that a general purpose FE-program must be able to provide in order to solve rotordynamic problems. On the other hand, the goal lies in evaluating the mathematical effort necessary when solving the equation of motion.

The discussion begins with the **stiffness matrix K**, which describes not only the stiffness of the rotor itself, but also that of the rotor support, consisting of the stator and the bearings. From a mathematical point of view, it is crucial to distinguish between the *isotropic* and *anisotropic* stiffness behavior of these three components forming the rotor system. Under the premise of isotropic material behavior, the stiffness characteristic of the rotor depends on whether it is axially symmetrical or not. If it is not, the lateral stiffness of the rotor in one plane will differ from the stiffness in other planes [33]. In that case, the use of an inertial (non-rotating) frame will result in stiffness coefficients that vary sinusoidally due to the rotation of the rotor, and therefore lead to a periodic coefficient differential equation [37]. This can be avoided if the equation of motion is written in a rotating coordinate system. In the case of an isotropic rotor support, the use of a rotating frame on an asymmetric rotor will lead to differential equations with coefficients that are constant in time. However, if the rotor is asymmetric and the support is anisotropic, the differential equation will have periodically varying coefficients in both the inertial and the rotating frame, which produces a parametric excitation. In that case, *Floquet theory* or other approximate techniques can be used to assess stability by looking at perturbations from the steady-state solution.

The presence of a **circulatory matrix N** is not restricted to rotating systems. However, in the field of rotordynamics, the circulatory matrix is one possibility to take into account the stiffness behavior of fluid-film bearings, if the rotor should be equipped with such kind of bearings. Fluid-film bearings can be described as a spring-damper system, but due to the pressure distribution within the lubrication gap of the bearing, the rotor displacement and the returning force of the bearing do not appear in the same direction [76]. This may lead to instabilities at higher rotational speed, and more generally speaking, to different resonance behavior when compared to a rotor with rigid bearings.

From a mathematical point of view, the circulatory matrix N contains non-conservative forces that depend on the position and the rotational speed of the rotor, rendering the matrix skew-symmetric:

$$\mathbf{N} = \mathbf{N}(\Omega) \qquad \text{with} \quad n_{ij} = -n_{ji} \ , \quad n_{ii} = 0 \tag{2.3}$$

Since the examples that will be presented within the current thesis do not contain fluid-film bearings, the circulatory matrix will not be discussed in more detail. Further reading can be found, amongst others, in [35].

The **damping matrix** $\boldsymbol{D}$ plays an important role for the stability of a system. Usually, the presence of damping in an oscillatory system is quite desired, as it reduces the amplitude in the case of resonance. On the other hand, if the goal is to isolate the vibrations of parts of the system, damping can be counterproductive. In rotordynamics, damping plays a likewise ambivalent role. Many rotor systems are operated supercritically, meaning at a rotational speed that lies above the (first) critical speed. Consequently, a resonance needs to be crossed during run-up. When crossing the critical speed, damping is highly appreciated, while in the supercritical area it can turn the system unstable. In this respect, it is important to distinguish between external and internal mechanical damping - which, in the case of rotation, is the equivalent of differentiating between non-rotating and rotating damping. *External damping* "is related to energy dissipation due to material crystalline and/or surface friction or micro-stick-slip friction occurring in stationary elements (like in rotor supports) and/or between stationary and rotating elements" [96]. *Internal damping* refers to the rotating parts and is caused by material damping as well as structural damping in the case of a conglomerated rotor, resulting from friction between the interfaces of the various rotor parts. The impact of internal and external damping on the rotor is very different and will be explained with the help of Figure 2.1, visualizing the effects of the different damping mechanisms. If the rotor is standing still, both damping mechanisms work in the opposite direction of the movement. If, however, the rotor is spinning, external damping causes forces that are dependent on the absolute velocity of the rotor, while in the case of internal damping, the forces are dependent on the relative velocity in a co-rotating coordinate system [26, 35]. In the case of imbalance excitation, the rotor bends in the direction of the imbalance and spins around in the deformed configuration [27]. Since there is no relative movement of the rotor (except for the spinning motion), internal damping does not contribute at all to the restoring forces, while external damping fully adds to the restoring forces.

With regard to stability, external damping usually has a stabilizing effect in the whole

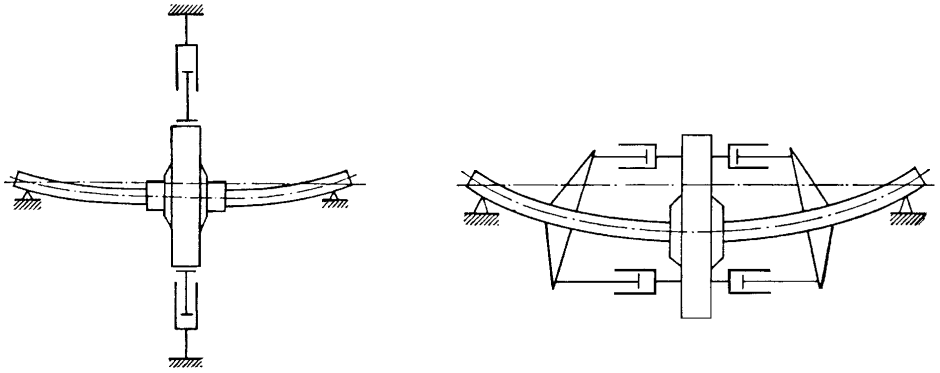

(a) non-rotating damping (b) rotating damping

Figure 2.1: Models to explain the effect of rotating and non-rotating damping (from [35] with permission of Springer Nature)

working range of a machine [37], whereas internal damping must be considered carefully. At critical speeds, internal damping contributes to the overall damping and has a stabilizing effect. Above critical speed, on the one hand, internal damping can cause instability by transferring energy from the rotation into the lateral oscillation of the rotor. This is a very critical process, as the kinetic energy stored in the rotation is usually vastly larger than the elastic energy the rotor can endure before failing. A detailed review on rotor instability due to internal damping can be found in [64]. On the other hand, apart from destabilizing the rotor system, the work of [52] indicates that damping can stabilize a former unstable system in which the instability arises from nonconservative terms of a circulatory matrix - depending on the structure of the damping matrix that arises from internal and external damping.

Regarding the structure of the damping matrix, with the presence of discrete damping elements, for example, such as the bearings, matrix D is typically not symmetric. Of course, it is possible to assume mass or stiffness-proportional damping to enforce a symmetrical shape of the matrix to allow for easier solving of the equation of motion by modal computations in the configuration space. Apart from being unphysical in probably most cases, the assumption of proportional damping also takes away the important distinction between internal and external damping. An unsymmetrical damping matrix, however, requires the transformation of the equation of motion from configuration space into state space, as will be explained in Chapter 2.2.1. Since the gyroscopic matrix is generally unsymmetrical, this is unavoidable anyhow, as will be shown in what follows.

The **gyroscopic matrix G** describes forces that arise when the rotor performs rotational movement normal to its axis of rotation. Apart from movement of the rotor support, normal rotation to the spinning axis can also occur when the rotor is experiencing lateral bending

due to external forces or due to imbalance excitation. The presence of the gyroscopic forces can be explained by using the *principle of conservation of angular momentum*:

$$\mathbf{T} = \frac{d\mathbf{L}}{dt} = \mathbf{I} \cdot \dot{\mathbf{\Omega}} + \mathbf{\Omega} \times (\mathbf{I} \cdot \mathbf{\Omega}) \tag{2.4}$$

where $\mathbf{L}$ is the angular momentum, $\mathbf{I}$ is the inertia tensor, $\mathbf{\Omega}$ is the vector of the angular velocity and $\mathbf{T}$ stands for the external moments acting on the rotating body. Equation (2.4) is formulated in the inertial frame and, without limiting the generality, it is rather complicated because of the fully populated inertia tensor. Due to the nonlinearity of Equation (2.4), it cannot directly be used to calculate the coefficients g_{ij} for Equation (2.1), even when considering such a simple system as a single, rotating rigid body. However, things become significantly simpler, if the same assumptions can be applied to the rotor system that are used to derive *Euler's equation of motion*:

$$\begin{aligned} T_1^c &= I_1^c \dot{\Omega}_1 - \Omega_2 \Omega_3 (I_2^c - I_3^c) \\ T_2^c &= I_2^c \dot{\Omega}_2 - \Omega_3 \Omega_1 (I_3^c - I_1^c) \\ T_3^c &= I_3^c \dot{\Omega}_3 - \Omega_1 \Omega_2 (I_1^c - I_2^c) \end{aligned} \tag{2.5}$$

Euler transforms Equation (2.4) to a coordinate system $(\vec{e}_1, \vec{e}_2, \vec{e}_3)$ that is fixed to the rotating body and in which the coordinate axes fall on the body's central principal axes of inertia (superscript c stands for the reference to the center of gravity). By doing so, the products of inertia in the inertia tensor I^c vanish and allow one to represent Equation (2.4) in the much reduced form of Equation (2.5). Yet, for modeling a rotor system and being able to use Equation (2.1), this means that the rotor must have a well-defined axis of rotation, which in addition must coincide with one of the baricentrical principal axes of inertia [37]. This condition is only fulfilled if the rotor is perfectly balanced, which, in practice, is never the case. Yet, if the amount of imbalance is small, it can be treated as a disturbance that acts on the rotor as an external force F, as will be shown later. But even if the rotor's spinning axis matches a principal axis of inertia, writing the equation of motion in a stationary reference frame will result in similar problems discussed with regard to anisotropic stiffness behavior: If the rotor is not axially symmetrical, the use of a stationary reference frame will lead to periodically varying coefficients g_{ij} in the gyroscopic matrix. Furthermore, since Equation (2.5) is still nonlinear in the rotational speed $\vec{\Omega}$, its use for Equation (2.1) requires linearization and therefore the assumption of small displacements and rotations, except for the rotation about the spinning axis. If all three conditions of small imbalance, axial

symmetry and small rotations are met, the gyroscopic matrix will have constant coefficients. Matrix G is skew-symmetric and dependent on the rotational speed:

$$G = G(\Omega) \qquad \text{with} \quad g_{ij} = -g_{ji} \ , \quad g_{ii} = 0 \tag{2.6}$$

At first glance, matrix G resembles the damping matrix D, since the gyroscopic forces $G\dot{q}$ are speed proportional, like in the case of viscous damping. Some authors even call the gyroscopic matrix G a *pseudo-damping matrix* [19, 46]. One must be aware, however, that, in contrast to the damping forces, the gyroscopic forces do not contribute to the balance of energy of the system. The gyroscopic forces do not perform mechanical work and are therefore no damping terms [90]. A gyroscopic system can still be conservative in the absence of damping forces and without non-conservative terms in the circulatory matrix [154].

Vector F contains all force functions that act on the rotor. The excitation by the imbalance of the rotor is of special interest. As mentioned above, the existence of an imbalance means that the rotor is in fact not rotating around a baricentrical principal axis of inertia. In that case, the requirements that allow for the principal axes transformation, which have been discussed in regard to the gyroscopic matrix, are not fulfilled and the fully populated inertia tensor has to be used to calculate the gyroscopic forces of the rotor. Keeping the inertial frame leads to position-dependent system matrices and, in combination with a constant spinning speed Ω of the rotor, to time-dependent system matrices. However, if the imbalance is small, it can be treated as an external force $\mathbf{U}$ that acts on the rotor in the form:

$$\mathbf{U} = m_e \epsilon \Omega_0^2 \begin{bmatrix} cos(\Omega_0 t) \\ sin(\Omega_0 t) \\ 0 \end{bmatrix} \tag{2.7}$$

where m_e stands for the mass of the rotor, which is considered to be a point mass, and e describes the lateral distance between imbalance mass m and the axis of rotation. A stationary coordinate system has been assumed in which the first two axes are orientated perpendicular to the axis of rotation, while the third axis falls together with the spin axis of the rotor. The cosine and sine terms cause the imbalance force to rotate at spin speed Ω_0 in the stationary frame.

The approach of treating the imbalance as an external force can represent a strong simplification. In the real world, any rotor is nonlinear to a greater or lesser extent. When considering bending resonances, the imbalance force will cause the rotor's center of gravity to displace

even further from the axis of rotation, thereby increasing the imbalance. This geometrical nonlinearity is not accounted for in the approach described above, as the imbalance force is considered to be a function of time

$$\mathbf{U} = \mathbf{U}(t) \quad \text{, but not of displacement} \quad \mathbf{U} = \mathbf{U}(t, q) \ . \tag{2.8}$$

Depending on the rotor system to be analyzed, the assumption of a small imbalance may or may not be be appropriate. In many cases, the rotor is well balanced or the lateral displacement is limited by the housing or adjacent parts. In other cases, like in the rotor system presented in Chapter 3, it is essential to incorporate the geometrical nonlinearity caused by lateral displacement due to the imbalance force.

2.2 Computational Solution Techniques

A non-problem-specific summary of solution techniques for Equations (2.1) and (2.2) can be found in [144]. Generally speaking, it is important to distinguish between solving the analysis in the *time domain* by direct integration of the equilibrium equations or by solving the problem in the *frequency domain*, for example, by using modal computations [37]. In what follows, the two different approaches will be outlined briefly with regard to peculiarities that arise from rotation.

2.2.1 Solution in the Frequency Domain

A frequency solution is only possible when the system matrices are time-independent. Summarizing the previous section, this is only true if the following assumptions are met:

- the rotor has a well defined axis of rotation,
- the rotor is rotating at a constant spin speed Ω_0 (steady-state),
- all rotations and displacements are small except for the rotation about the axis of rotation,
- the imbalance of the rotor is small,
- either the rotor or the supports show isotropic stiffness behavior,
- in an inertial reference frame, the rotor needs to be axial symmetric.

In other words, a solution in the frequency domain is only possible with linear systems (or at least linearized systems) operating in a steady state.

Most frequency domain approaches use the eigenvalues and mode shapes to calculate the free and the forced vibrations of a rotor system. The eigenvalues (λ) and mode shapes (φ^R) are obtained by solving the characteristic polynomial of Equations (2.1) and (2.2), which is in the inertial frame:

$$\left[\boldsymbol{\lambda}^2\mathbf{M} + \boldsymbol{\lambda}\left(\mathbf{D} + \mathbf{G}(\Omega)\right) + \left(\mathbf{K} + \mathbf{N}(\Omega)\right)\right]\boldsymbol{\varphi}^R = \mathbf{0} \tag{2.9}$$

Equation 2.9 describes a quadratic eigenvalue problem that is difficult to solve directly. One solution is to transform the equation of motion from the configuration space into a *state-space* representation, thereby converting the system of n coupled second-order differential equations into a set of $2n$ first-order differential equations [91]:

$$\mathbf{A}\dot{\mathbf{z}} + \mathbf{B}\mathbf{z} = \mathbf{R} \tag{2.10}$$

with

$$\mathbf{z} = \begin{bmatrix}\mathbf{q}\\ \dot{\mathbf{q}}\end{bmatrix}, \qquad \mathbf{R} = \begin{bmatrix}\mathbf{F}\\ \mathbf{0}\end{bmatrix} \tag{2.11}$$

and

$$\mathbf{A} = \begin{bmatrix}\mathbf{D} + \mathbf{G}(\Omega) & \mathbf{M}\\ \mathbf{M} & 0\end{bmatrix}, \qquad \mathbf{B} = \begin{bmatrix}\mathbf{K} + \mathbf{N}(\Omega) & 0\\ 0 & -\mathbf{M}\end{bmatrix} \tag{2.12}$$

The characteristic polynomial to calculate the eigenvalues (λ_s) and mode shapes (ψ^R) becomes accordingly:

$$\left[\boldsymbol{\lambda}_s\mathbf{A} + \mathbf{B}\right]\boldsymbol{\psi}^R = \mathbf{0} \tag{2.13}$$

Due to the non-symmetrical system matrices, which are a special characteristic of rotordynamic analyses, the eigenvalues and mode shapes appear in conjugate complex pairs. Solving Equation (2.13) therefore requires a complex eigensolver, which is nowadays available in many but not necessarily in all programs.

A common alternative to converting the problem description into a state-space representation is to use the *subspace-projection method* in order to extract the complex eigenvalues and complex mode shapes (see i.e. [1, 23, 105]). Here, in a first step, the symmetric eigenvalue problem is solved by ignoring matrices D and G in Equations (2.1), respectively, matrix C in Equation (2.2), as well as any unsymmetric contributions to the stiffness matrix K. In doing so, the eigenvalues λ_r of the reduced system become purely imaginary numbers $\lambda_r = i\omega$, in

which ω stands for the undamped natural frequencies, and the eigenvalue problem is now:

$$\left(-\boldsymbol{\omega}^2\mathbf{M} + \mathbf{K}\right)\boldsymbol{\varphi}_r = \mathbf{0} \tag{2.14}$$

In the next step, the following transformation prescription is used to project the original matrices on the subspace spanned by the real eigenvectors φ_r of the reduced system:

$$\begin{aligned}
\mathbf{M}_r &= \left[\boldsymbol{\varphi}_{r,1}, \boldsymbol{\varphi}_{r,2}, ..., \boldsymbol{\varphi}_{r,n}\right]^T \mathbf{M} \left[\boldsymbol{\varphi}_{r,1}, \boldsymbol{\varphi}_{r,2}, ..., \boldsymbol{\varphi}_{r,n}\right] \\
\mathbf{D}_r &= \left[\boldsymbol{\varphi}_{r,1}, \boldsymbol{\varphi}_{r,2}, ..., \boldsymbol{\varphi}_{r,n}\right]^T \mathbf{D} \left[\boldsymbol{\varphi}_{r,1}, \boldsymbol{\varphi}_{r,2}, ..., \boldsymbol{\varphi}_{r,n}\right] \\
\mathbf{K}_r &= \left[\boldsymbol{\varphi}_{r,1}, \boldsymbol{\varphi}_{r,2}, ..., \boldsymbol{\varphi}_{r,n}\right]^T \mathbf{K} \left[\boldsymbol{\varphi}_{r,1}, \boldsymbol{\varphi}_{r,2}, ..., \boldsymbol{\varphi}_{r,n}\right] \\
\mathbf{G}_r(\Omega) &= \left[\boldsymbol{\varphi}_{r,1}, \boldsymbol{\varphi}_{r,2}, ..., \boldsymbol{\varphi}_{r,n}\right]^T \mathbf{G}(\Omega) \left[\boldsymbol{\varphi}_{r,1}, \boldsymbol{\varphi}_{r,2}, ..., \boldsymbol{\varphi}_{r,n}\right] \\
\mathbf{N}_r(\Omega) &= \left[\boldsymbol{\varphi}_{r,1}, \boldsymbol{\varphi}_{r,2}, ..., \boldsymbol{\varphi}_{r,n}\right]^T \mathbf{N}(\Omega) \left[\boldsymbol{\varphi}_{r,1}, \boldsymbol{\varphi}_{r,2}, ..., \boldsymbol{\varphi}_{r,n}\right]
\end{aligned} \tag{2.15}$$

Now, the projected eigenvalue problem can be expressed in the following form:

$$\left[\boldsymbol{\lambda}_r^2\mathbf{M}_r + \boldsymbol{\lambda}_r\left(\mathbf{D}_r + \mathbf{G}_r(\Omega)\right) + \left(\mathbf{K}_r + \mathbf{N}_r(\Omega)\right)\right]\boldsymbol{\phi}_r^R = \mathbf{0} \tag{2.16}$$

Since rotordynamics is typically interested in the lower vibration modes, high-frequency modes can be ignored, thereby reducing the problem size. "Typically, the number of eigenvectors is relatively small; a few hundred is common" [23]. This reduction method is called *Rayleigh-Ritz condensation* by some authors [19]. Equation (2.16) can be solved by using the QZ algorithm, which is a solution method for a generalized unsymmetrical eigenvalue problem [93]. The such obtained complex eigenvalues λ_r of the projected system are an approximation of the eigenvalues λ of the original system in Equation (2.9). The eigenvectors of the original system are approximated likewise by:

$$\boldsymbol{\varphi}_k^R = \left[\boldsymbol{\varphi}_{r,1}, \boldsymbol{\varphi}_{r,2}, ..., \boldsymbol{\varphi}_{r,n}\right]\boldsymbol{\phi}_{r,k}^R \tag{2.17}$$

where φ_k^R is the approximation of the k-th eigenvector of the original system.

2.2.2 Solution through Direct Time Integration

The previous chapter summed up the requirements that need to be fulfilled, or rather the simplifications that need to be acceptable, when performing the rotordynamic analysis in the frequency domain. In the case of a nonlinear system or in a transient analysis, the solution must be obtained through direct time integration. Since the equation of motion of

a rotating system contains matrices that depend on the spin-speed, and, in general, contains additional matrices compared to a structure at rest, this is computationally very costly, but is sometimes unavoidable.

The most commonly used numerical integration algorithms for rotordynamics are the *Newmark* family methods and the *Wilson-θ* method [14]. The former is widely used for implicit integration in terms of the average acceleration method, as well as for explicit integration in terms of the central difference method.

2.3 The Finite Element Method in Rotordynamics

The current FE approaches used for rotordynamic problems can be classified into three different categories:

- 1D beam-element models,
- 2D axisymmetric elements,
- 3D solid modeling.

In what follows, the development history of the different approaches will be briefly outlined, together with their capabilities and limitations.

2.3.1 1D Beam-Element Models

1D beam-element models intellectually divide a rotor system into a shaft, which is represented by finite beam-elements, and into rigid "disks", which are represented as point masses with lateral and rotational inertia to account for gyroscopic moments. Spring elements can be added to account for bearing compliance. The accuracy of these types of models strongly depends, on the one hand, on the suitability of the finite beam-elements used. The works of *Jones* [63], *Rao* [113] and *Nandi* [98, 99] contain detailed information about the development history as well as a critical assessment of the capabilities of finite beam-elements for rotordynamic problems. Therefore, only pioneering discoveries will be repeated here.

It was not until 1972 that the finite element method was established for rotordynamic analysis by *Ruhl* and *Booker* [118], providing an FE-model of a turbo-rotor system based on Euler-Bernoulli beam theory, representing the blade ring as a rigid disk. This first approach neglected the effects of rotary inertia, gyroscopic moments and axial loads, which was upgraded in 1976 by *Nelson* and *McVaugh* [102] using cubic shape functions to develop the

gyroscopic element matrices. The authors first used Rayleigh beam theory, thereby neglecting the influence of shear deformation. Later, *Nelson* [101] developed, amongst others, a finite beam-element using Timoshenko beam theory and, in doing so, also accounting for shear deformation.

In 1985, *Genta* [36] demonstrated that taking into account shear deformation has a strong influence on the calculation of critical speeds of a rotor: While rotary inertia increases critical speeds, the effect of shear deformation is in the opposite direction, thereby exceeding the effect of rotary inertia in magnitude. As a consequence, models that account for rotary inertia but ignore shear deformation are less accurate than models ignoring both effects.

Until today, a large number of finite beam-elements has been proposed, taking into account, on the one hand, typical rotor geometries such as hollow or conical cross-sections, and, on the other hand, accounting for various effects such as internal viscous or hysteretic damping, axial or torsional loads and the important influence of shear deformation (i.e. [39, 48, 116] in addition to the afore mentioned sources).

When creating a shaft-line model, the procedure provides a representation of the different sections of a shaft with finite beam-elements that correctly describe length and diameter or cross-section, respectively, of the specific sections. Most real-world rotors, however, contain abrupt changes in diameter, i.e. at the position of bearing seats, or contain changes in the form of their cross-section, for instance, at key flats to enable torque transfer to mounting parts. At these positions, all beam-models derived from classical beam theory are inaccurate, as they assume plain cross-sections to remain plain during bending deformation [119, 128, 142]. This assumption is valid for a uniform shaft, but is violated at stepped diameter changes or at changes in cross-section where distortions occur and bending stress is no longer linear to the radius. These distortions in bending stress lead to a decrease in lateral stiffness, and since beam-models do not account for this effect, their model representation of the rotor tends to be too stiff. In 1989, *Stephenson*, *Rouch* and *Arora* demonstrate on a laboratory rotor with three disks taken over from [141] that the error in calculating natural frequencies using classical beam-elements can easily reach more than ten percent within the first five modes [128]. A possible solution was suggested in 1990 by *Vest* and *Darlow* [142], who proposed a method to use the governing equations of a conical beam-element and locally alter the Young's modulus to improve the effective beam stiffness. A detailed 3D solid FE-model is used to update the modulus-corrected beam-model.

With regard to the capabilities of beam-element models, it can be noticed that the approach offers a structured model generation and intuitive representation of the geometry. The pro-

cedure results in a model that can be solved with reasonable computational effort. However, this comes at the price of a number of disadvantages, which can be divided into limitations in mathematical model accuracy and in limitations in physical model representation. As already addressed in the introduction of the current thesis, apart from limitations in accuracy, the most significant drawback of beam-element models from today's point of view is the fact that shaft-line models need to be generated by hand in a time consuming and tedious process without the possibility to reuse CAD-data.

A tabular overview of limitations in the mathematical model accuracy resulting from the choice of beam-elements to represent the shaft of a rotor is given by *Nandi* in [98] and is repeated in Table A.1 of Appendix A. Mainly two things are still solved only unsatisfactorily: Beam-elements with reasonable effort of implementation are, on the one hand, inaccurate at positions with abrupt change in cross-section, and, on the other hand, require axial symmetry. Theoretically, both problems can be solved by using modulus-corrected beam-elements as described above. Practically, the effort to update single elements by yet another detailed 3D FE-model of the rotor is unrealistically high, which is probably the reason why the approach by *Vest* and *Darlow* [142] has not prevailed until today.

However, even when leaving aside the problems in mathematical model accuracy, beam-element models are still a linearized, one-dimensional approach with significant limitations in physical model representation. By representing disks as rigid, the approach uncouples the behavior of the shaft from the dynamic behavior of the disk. Representing attachments to the rotor, such as blade rings of turbo-systems, as rigid disks neglects:

- the stiffening effect of the disk on the shaft and vice versa,
- the effect of centrifugal stiffening of the disk,
- interaction between axial, lateral and torsional behavior of shaft and disk.

Especially in the field of turbo machinery, it is well known that the flexibility of a blade ring ("disk") can have a strong influence on the natural frequencies of lateral bending of the whole system [12, 60]. For an accurate prediction of critical speeds in the early phase of the design process, a coupled model is needed that cannot be delivered by 1D beam-element models. With advances in computational power and progress in FEM, 2D axisymmetric finite elements have been proposed as an alternative. This will be discussed briefly in the next section, before changing to true 3D solid modeling.

2.3.2 2D Axisymmetric Elements

This approach exploits the fact that many rotors are axially symmetric, which allows for the use of a Fourier series method as described, amongst others, in [20]. The first publication on using axisymmetric finite elements for rotordynamic problems was probably presented in 1984 by *Geradin* and *Kill* [45]. The authors formulate the kinetic and strain energy in the rotating as well as in the inertial frame and use Hamilton's principal to derive the equations of motion. With regard to finite element discretization, the authors use cylindrical coordinates (r,θ,z) and Fourier expansion of the displacement field in the circumferential direction of the following form:

$$\begin{aligned} q_r &= \sum_{n=0}^{\infty} \sum_{m=0}^{1} q_r^{n,m} \cos\left(n\theta + m\frac{\pi}{2}\right) \\ q_\theta &= \sum_{n=0}^{\infty} \sum_{m=0}^{1} q_\theta^{n,m} \sin\left(n\theta + m\frac{\pi}{2}\right) \\ q_z &= \sum_{n=0}^{\infty} \sum_{m=0}^{1} q_z^{n,m} \cos\left(n\theta + m\frac{\pi}{2}\right) \end{aligned} \tag{2.18}$$

"With this approach, the model is only required to represent the r-z plane, and the circumferential variation is cared for in the element itself. The 2D form of the element can be thought of as a complete ring in its mathematical representation. The three-dimensional problem is converted into a two-dimensional problem, with all of the geometry effects in the cross-section retained" [128]. This reduction of the mathematical problem dimension, however, comes at the price of exchanging a single, three-dimensional problem for a series of two-dimensional problems: Each term of Equation (2.18) is calculated in a separate analysis and the final solution is obtained by superimposing the successive harmonics. Still, the exchange is usually worthwhile with regard to computational costs [20]. Since the use of 2D axisymmetric finite elements leads to equations with a significantly larger number of DOFs than classical beam-element models, *Geradin* and *Kill* introduce a system reduction in the form of the classical component mode method. Therefore, the rotor model is split into a number of substructures.

With regard to the importance of the subject, less work than could be expected was published on using 2D axisymmetric finite elements for rotor dynamic problems [41]. It is also noticeable that the focus lays more on techniques to reduce the number of system equations than to improve the functionality of FE approaches, which is understandable taking

into account the limited computational resources of those times. In 1993, *Stephenson* and *Rouch* [127, 128] adopted the approach of using Fourier expansion to generate axisymmetric elements, but suggested the Guyan reduction technique as an alternative method to reduce the system's degrees of freedom. In 1996 and 1997, *Genta* and *Tonali* suggested a so-called $1\frac{1}{2}$D-approach by combining finite beam-elemts to model the shaft with 2D axissymetric elements to account for the flexibility of disks [42] and blade arrays [43]. The authors use *complex coordinates* to reduce the number of DOFs [38].

Although 2D axisymmetric finite elements, in comparison to classical beam-element models, are capable of taking disk flexibility into account, their angular shape is still a strong simplification that does not fulfill the modeling requirements of many real-world rotor systems. In the field of turbo machines, researchers tend towards 3D solid modeling and try to make use of the cyclic symmetry of blade rings in order to obtain models of smaller size [12, 13, 60, 138, 139]. "However, the axisymmetric and cyclic assumptions usually fail to model the response of bladed rotor systems with unsymmetric loading scenarios due to system imbalance, fluid-structural interactions, and blade-out scenarios, and cannot represent structures that do not have that specific geometry to exploit" [145]. Complex geometries or non-axisymmetric rotors require the use of true 3D solid modeling [41].

2.3.3 3D Solid Modeling

Although 3D solid modeling became generally available in the 1980s with the emergence of (commercial) general purpose FE-codes [126], the computers of those times lacked the power to solve rotordynamic models through direct time integration, thereby automatically taking into account rotordynamic effects, such as gyroscopic coupling, stress stiffening or even non-axial symmetry of the rotating parts. Therefore, research was directed on solutions in the frequency domain and on model reduction, or more generally speaking, on solutions with lower computational costs. A recent overview on model reduction methods in rotordynamics is presented by *Wagner et al.* in [145].

One of the first works on 3D solid finite elements for rotordynamics was presented in 2001 by *Nandi* and *Neogy* [99]. The authors develop the necessary kinematic equations to describe the virtual work due to elastic deformation and due to inertia forces. The formulation of the gyroscopic effects requires the shaft cross-section to have two axes of symmetry. The effect of a deformed cross-section due to bending, which causes the centrifugal forces to create a torque further affecting the bending, is taken into account. From the principal of virtual work, the authors develop finite element equations for 3D solid 20-node elements

in the rotating frame but not in the inertial frame, which is significantly more difficult to implement. In 2003, *Nandi* upgrades the afore mentioned approach by including the effect of *centrifugal stiffening*, which causes natural frequencies to increase due to in-plane stress caused by the centrifugal forces [98]. Instead of modifying the governing equations (writing the centrifugal force on the right side of the equation of motion), Nandi suggests solving the equations of motion in the deformed configuration.

Other early works on using 3D solid modeling in rotordynamics were published by *Rao et al.*, reporting a strong *centrifugal softening* or *spin softening* effect [113–115]. The spin-softening effect is typically overcompensated by the centrifugal stiffening effect so that the natural frequencies increase likewise with increasing rotational speed [41]. In disk-like axisymmetric rotors, the spin softening effect is mathematically stronger than the centrifugal stiffening only at non-physically high rotational speeds.

The use of 3D solid modeling is capable of including geometric nonlinearities, centrifugal stiffening and spin softening. Therefore, Equation (2.1) is extended to the following form (see i.e. [41]) in the inertial frame:

$$\mathbf{M}\ddot{\mathbf{q}} + [\mathbf{D} + \boldsymbol{\Omega}\mathbf{G}]\,\dot{\mathbf{q}} + \left[\mathbf{K} + \boldsymbol{\Omega}^2\mathbf{K}_\Omega + \boldsymbol{\Omega}^2\mathbf{K}_S + \boldsymbol{\Omega}\mathbf{N}\right]\mathbf{q} = \mathbf{F} + \boldsymbol{\Omega}^2\mathbf{F}_\Omega \tag{2.19}$$

where $\mathbf{K}_\Omega$ is the geometric stiffness matrix accounting for the effect of stress stiffening due to the centrifugal forces, $\mathbf{K}_S$ (negatively defined) contains the aforementioned spin-softening effect due to centrifugal forces, and $\mathbf{F}_\Omega$ describes the vector of the centrifugal loads.

In the rotating frame, Equation (2.2) is extended likewise (see i.e. [19]):

$$\mathbf{M}'\ddot{\mathbf{q}}' + [\mathbf{D}' + \boldsymbol{\Omega}\mathbf{C}]\,\dot{\mathbf{q}}' + \left[\mathbf{K}' + \boldsymbol{\Omega}^2\mathbf{K}'_\Omega + \boldsymbol{\Omega}^2\mathbf{K}'_S + \boldsymbol{\Omega}\mathbf{N}'\right]\mathbf{q}' = \mathbf{F}' + \boldsymbol{\Omega}^2\mathbf{F}'_\Omega \tag{2.20}$$

where $\mathbf{K}'_S$ is the centrifugal (negative) stiffness.

The corresponding element matrices are calculated using energy methods. A comprehensive overview of different rotor configurations (i.e. unsymmetric, axial symmetric, cyclic symmetry) is presented in [71].

Given the importance of 3D solid modeling for accurate rotordynamics, the number of publications following the pioneering works described above is surprisingly small. Considerable progress, however, can be observed in the rotordynamic capabilities of general purpose FE-codes, which will be described in the subsequent chapter.

2.4 Using General-Purpose FE-Programs for Rotordynamic Problems

With regard to 3D solid modeling, general-purpose FE-programs nowadays offer mainly three different approaches with regard to solving rotordynamic problems:

- solution in the frequency domain in the rotating frame,
- solution in the frequency domain in the inertial frame,
- solution in the time domain by direct integration in an arbitrary coordinate system.

The different approaches will be outlined in what follows.

2.4.1 Solution in the Frequency Domain in the Rotating Frame

As mentioned above, implementing finite element equations of 3D continuum elements is significantly more difficult in the inertial reference frame than in the rotating frame [99]. Therefore it is no wonder that rotordynamic capabilities of general purpose FE-programs were first established in the rotating frame.

Calculating the eigenvalues and eigenvectors of Equation (2.20) typically consists of three subsequent steps: First, the eigenvalues and eigenvectors of the undamped system are calculated when the system is at rest, causing all speed-dependent matrices to vanish and leaving only the stiffness matrix K and the mass matrix M. In the second step, the centrifugal force and the coriolis force are applied as volume forces in a nonlinear static analysis, thereby deriving the other system matrices. To apply the volume forces, an axis of rotation and a (constant) spin speed has to be defined. Step three is a complex eigenvalue extraction that requires a corresponding complex eigensolver. ABAQUS, for instance, uses the subspace projection method described in Chapter 2.2.1 and the QZ-algorithm to solve Equation (2.16).

In a rotating coordinate system, the rotor does not necessarily need to be axial symmetric or isotropic. If it is not, however, the user has to make sure that the non-rotating part of the rotor system has isotropic stiffness behavior, as described in Chapter 2.1.

2.4.2 Solution in the Frequency Domain in the Inertial Frame

Implementing the finite element formulations of a rotating system in the inertial frame is significantly more difficult than in the rotating frame. Most general purpose FE-codes have acquired this capability only very recently. For example,

- ANSYS started to offer rotordynamic capabilities for 3D solid finite elements (SOLID 185-187) in the inertial frame with release 11.0 in the year 2007 [103],
- ABAQUS followed with release 6.12 in 2012 [22],
- MSC NASTRAN implemented full 3D solid modeling capabilities with release 2016 [94].

The modeling limitations are the same as described in Chapter 2.2.1, which consist in a linearization of the problem around a constant spin-speed and the prerequisites of the rotor being axial symetric and having a well defined axis of rotation.

2.4.3 Solution through Direct Time Integration

High-fidelity FE-models possess a large number of modes in the high-frequency range that have no physical meaning. These high-frequency components can experience excitation either by nonlinearities (i.e. rotor-stator contact, or chattering due to bearing-play) that transfer energy from the low-frequency into the high-frequency range, thereby hindering conversion. Another source of excitation in the high-frequency range results from the fact that acceleration is derived by numerical differentiation, thereby often creating unacceptable numerical noise [57]. Most general purpose FE-codes have implemented extensions of the standard Newmark-β method that are capable of providing numerical damping that does not strongly affect the physically meaningful "low" frequency range, but removes content from the physically unreasonable high-frequency range. These algorithms are namely the *Hilber-Hughes-Taylor method* (HHT method) [55] and the so-called *Generalized-α method* [18].

3 Outlined Rotor System

A special diamond coring system provides the fundamental hardware to test and validate the modeling approach in this thesis. The system is rather complex, both in the sense of mechanical design and in the sense of rotordynamics. The diamond coring system is a serial product of an industrial manufacturer. Within the underlying research, it has been strongly modified in order to create certain dynamic effects, which the simulation model should be able to represent in an appropriate way. However, it must be clear, that the effects that will be outlined in the further course of this thesis are the result of heavy modifications to the serial product in order to provide the opportunity for academic research, and do in no way occur in normal operation.

In the following, Chapter 3.1 provides a general description of the diamond coring system as well as its purpose and main application. Chapter 3.2 focuses on the rotordynamic perspective and goes into the relevant details of the mechanical design.

3.1 General Description

The diamond coring system Hilti DD-30-W provides the fundamental hardware that is used for the experiments in the further course of this thesis. The DD-30-W is an electric power tool, designed to drill through-holes or blind-holes for anchor setting into undergrounds like steel-reinforced concrete, stone or marble. The actual drill bit is hollow and the cutting edges are made out of industrial diamonds embedded in a supporting matrix. With regard to anchor setting, the main advantage of diamond coring over conventional hammer drilling is the ability to drill accurate anchor holes even into steel-reinforced concrete. This feature is especially important when installing the facade of a building in which the anchors need to be positioned exactly and must be fully loadable. Furthermore, diamond coring is impact free, which plays an important role when drilling holes into stone or marble, or when drilling holes close to an edge, like when installing a handrail on a balcony. Also, the emission of structure-borne sound is reduced by several dimensions compared to hammer drilling, which is important in the case of renovation work in hospital, commercial and residential buildings.

A picture of the system is presented in Figure 3.1. The tool allows for hand-held operation as well as the use of a supporting stand. During drilling operation, water streams through the inside of the tool and the hollow core bit for cooling and to flush away excavated material. The water is collected when streaming back out to the surface and is either discharged or

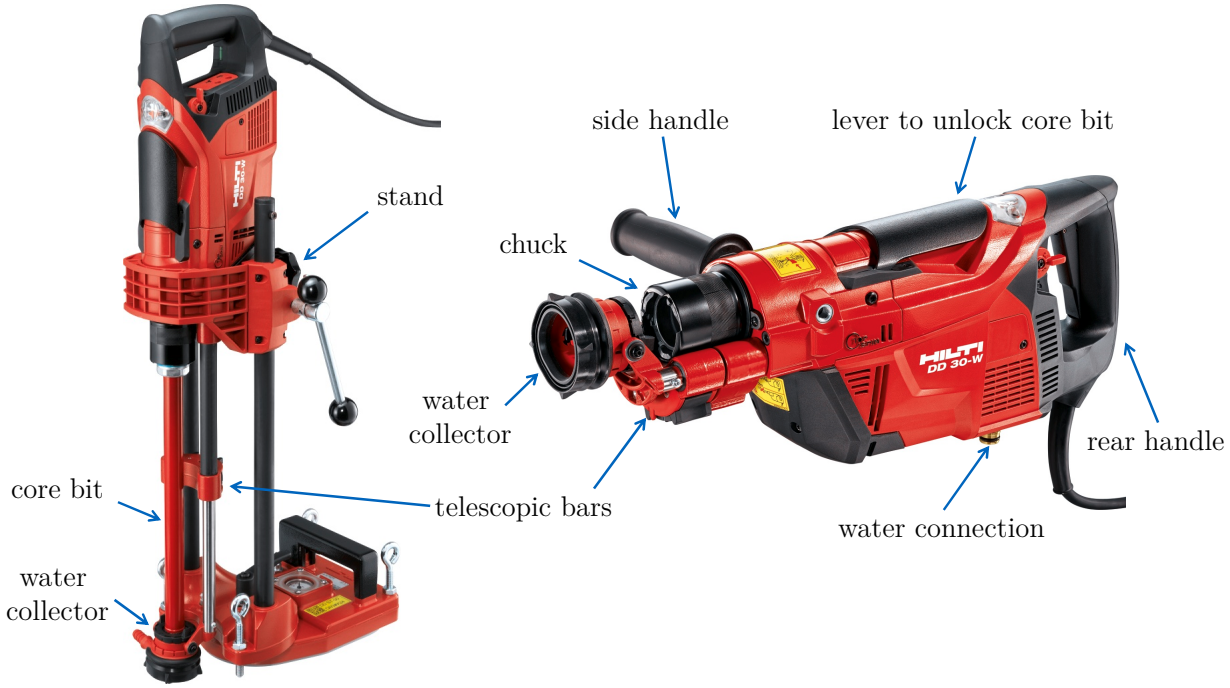

(a) the tool

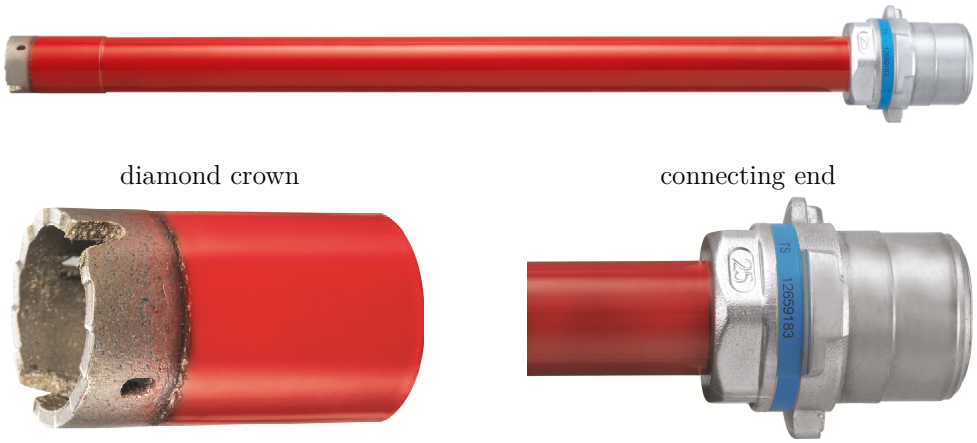

(b) the diamond core bit (here diameter = 25 mm)

Figure 3.1: The diamond coring system acting as an application example

recycled. The tool is designed to hold core bits with diameters between 8 mm and 35 mm. When using core bits within this rather small diameter range for anchor setting (which means drilling blind-holes), the drill core usually brakes off and then remains inside the core bit. Due to the small diameter, the weight of the drill core is not sufficient to simply shake it out of the core bit. To remove the core from the bit, the latter needs to be detached from the drilling machine. Since professional users need to detach and reattach the core bit up to several hundred times during a single working shift, the system is equipped with a quick-release chuck, which allows for a fast and key-less exchange of core bits. The chuck is force-locked and can be operated easily by hand with a lever fixed to the machine, providing an ease of use that is unrivaled on the market.

What makes the Hilti DD-30-W so special in the sense of rotordynamics, and the reason why it was chosen to function as a test example for the modeling approach in Chapter 5 is its *top-spin technology*: The core bit not only rotates around its axis of rotation, but in addition performs a tumbling movement, as will be explained in detail in Chapter 3.2. The top-spin technology is unique and creates an unrivaled drilling performance that is two to three times higher than that of conventional coring systems. With regard to rotordynamics, this overlying tumbling movement has the potential to create remarkable dynamic effects, especially in combination with the previously described force-locked chuck, which holds the core bit.

3.2 Rotordynamic Perspective

This chapter outlines the mechanical design of the diamond coring system by first explaining the overall kinematics in a global manner. After that, some components are discussed in more detail. The focus then lies on the force-locked chuck, which plays an important role for the dynamic system behavior.

3.2.1 Global Description and Kinematics

To start with a global description, Figure 3.2 shows a sectional view of the underlying CAD-model. Figure 3.3 includes a schematic diagram, which is more clearly arranged.

The core bit is connected to a rotating shaft by a force-locked chuck. These three components, *core bit*, *chuck* and *shaft* form a subsystem, which will be referenced as the *drive shaft*, and can be considered as a slender, overhung rotor. The shaft is supported by deep-groove

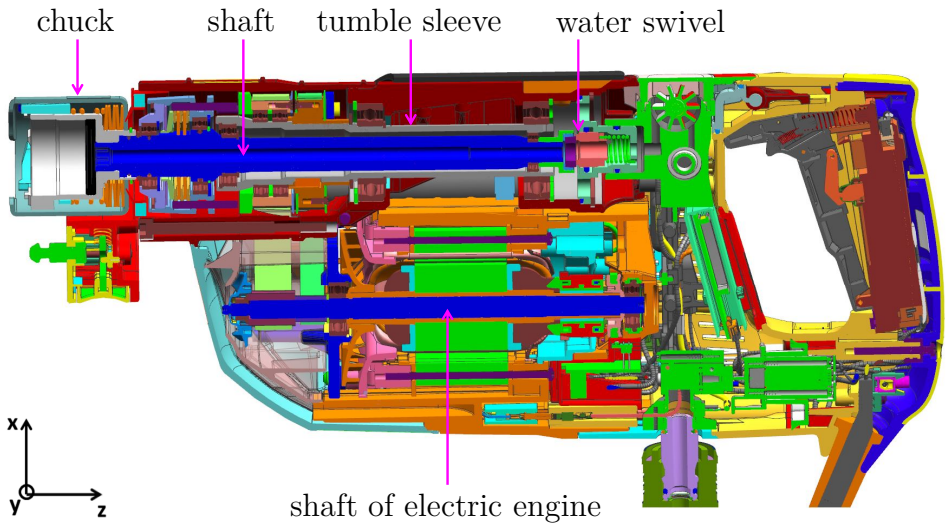

Figure 3.2: Sectional CAD-view of the outlined rotor system

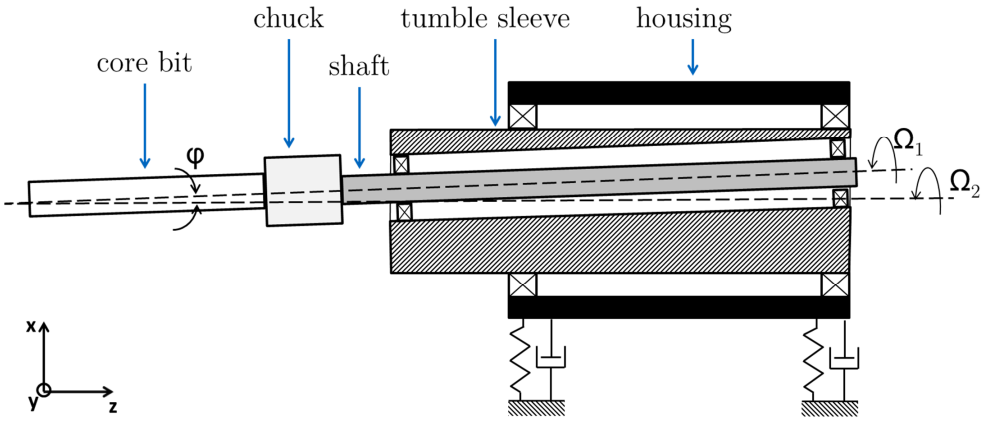

Figure 3.3: Schematic diagram of the outlined rotor system

ball bearings inside a hollow sleeve, which also rotates. The bore of the sleeve in which the shaft rotates is not coaxial to the sleeve's axis of rotation, but has an offset and is twisted by an angle φ. This causes the drive shaft not only to rotate around its own spinning-axis, but, in addition, to perform a tumbling movement around the sleeve's axis of rotation. The sleeve is supported by deep-groove ball bearings in the housing of the machine. Both the shaft and the sleeve are driven by the same electric motor via belt transmissions. The ratio between the turning speed of the shaft (Ω_1) and the sleeve (Ω_2) is fixed, while the turning speed of the shaft is faster:

$$\frac{\Omega_1}{\Omega_2} = n, \qquad \Omega_1 > \Omega_2 \tag{3.1}$$

The shaft, chuck and core bit are hollow, and water is flushed through the drive shaft to cool the system and to wash away excavated material. Since the relative movement between the shaft and the housing of the machine is not only a rotation but also a tumbling movement, a sealing concept is required that allows for relative movement in all six DOFs between the shaft and the housing. The problem is solved by using a mechanical seal, as shown in Figure 3.4, which contains three sealing points. The sealing between the shaft and the housing is provided by two sliding rings. The stationary ring on the housing side is axially movable and preloaded by a spring, thereby accommodating any axial movement between shaft and housing. The sealing between this ring and the housing is provided by a simple o-ring gasket. The rotating sliding ring on the shaft side is resiliently mounted in a holder, which in turn is press-fitted to the end of the shaft. The resilient mount of the rotating sliding ring accommodates any perpendicular relative movement. Aside of being able to compensate for relative movement between rotor and stator, a mechanical sealing offers the advantage of low friction and thereby of low power losses.

3.2.2 Power Train

Next, the focus is directed on the power train, explaining the torque transfer from the rotor of the electric engine to the different rotating parts. Figures 3.5 and 3.6 show the rotating parts of the power train. In Figure 3.5 the single parts have different colors to be able to separate them, while in Figure 3.6 the parts rotating at the same rotational speed are colored in the same way.

The rotor of the electric engine drives the tumble sleeve via a toothed belt. The toothed belt disk on the tumble sleeve side is firmly attached to it. There is no problem here, since

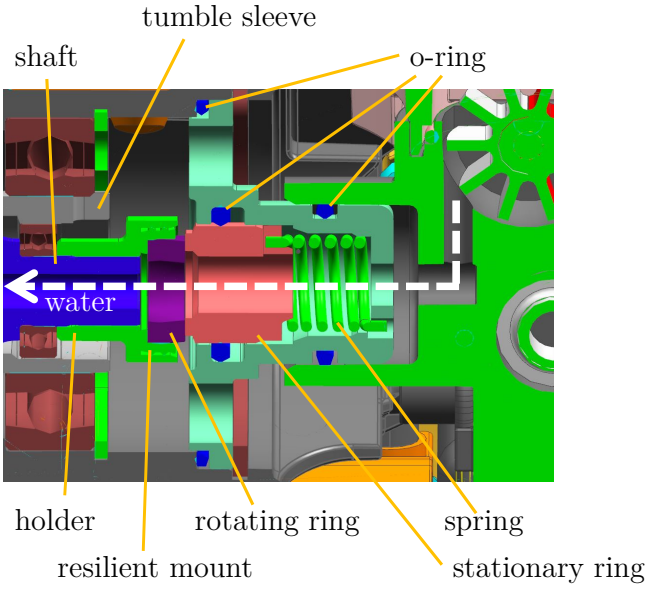

Figure 3.4: Schematic diagram of the mechanical sealing

the outside of the sleeve is coaxial to its spinning axis and the tumble sleeve simply rotates. In contrast, the torque transfer to the drive shaft is more complicated and involves more parts than just another toothed belt disk. The major problem in the torque transfer arises from the fact that the shaft not only spins around its own axis of rotation, but, in addition, performs a tumbling movement around the axis of rotation of the tumble sleeve. Since the rotor of the electric drive rotates parallel to the spinning axis of the tumble sleeve, the tumbling movement of the shaft must somehow be compensated in the driving elements. This is done by an elastic rubber joint. First, the electric rotor drives another toothed belt disk, which is also fitted to the tumble sleeve but is not firmly mounted; rather it is supported on roller bearings. These bearings experience the difference in rotational speed between the tumble sleeve and the shaft, but since the outside of the tumble sleeve is coaxial to its spinning axis, which in turn is parallel to the spinning axis of the electric engine, there is no other relative movement that needs to be compensated. For the further torque transfer to the shaft, the rubber joint comes into play: It connects the toothed belt disk to a slip-clutch that is mounted on the shaft. Thereby the rubber joint compensates the relative movement between the shaft and the sleeve in the radial direction and in the rotational DOFs perpendicular to the spinning axis of the tumble sleeve. The difference in rotational speed is compensated by the roller bearings on which the toothed belt disk is mounted on the tumble sleeve.

As previously explained, the rubber joint is not directly connected the shaft, but rather

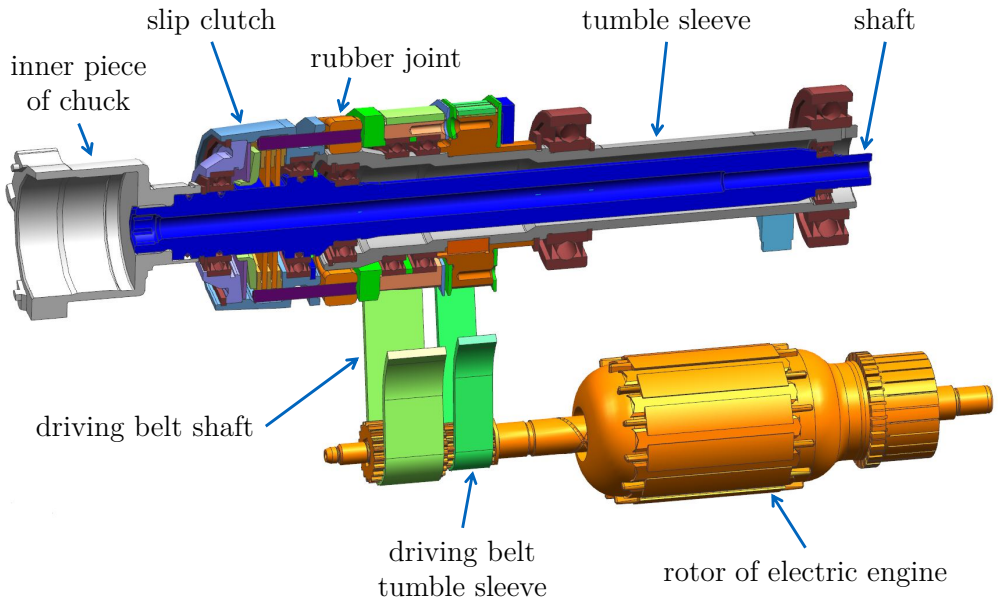

Figure 3.5: Sectional CAD-view of the rotating parts

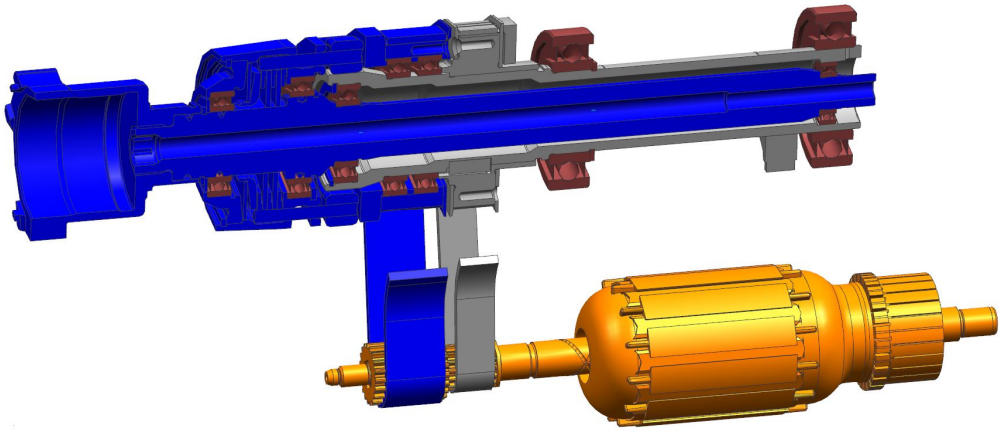

Figure 3.6: Sectional CAD-view of the rotating assembly groups (color according to rotational speed)

through a slip-clutch. This slip-clutch is an important safety feature, but in the context of this thesis, its functionality is not activated so it does not have a large influence on the dynamic system behavior, except for its mass and added stiffness to the shaft. For the sake of completeness, its role in the torque transfer will be outlined briefly. The purpose of the slip-clutch is to protect the operator in the case of a sudden deadlock of the core bit in the drilling hole, by separating the electric engine from the drive shaft. The working principal is that of a friction disk clutch, in which half of the disks have a form-locking connection to the shaft and are frictionally engaged with the other half of the disks, which in turn have a form-locking connection to the housing of the slip clutch. A pre-stressed spring ensures that there is enough friction between the disks to transfer the torque of normal operation, but allows slipping if the core bit should jam during drilling operation. The housing of the clutch is mounted to the shaft on roller bearings. In normal operation, the slip-clutch is rotating together with the shaft, and there is almost no relative movement, except for some play in the bearings and in the form-locking connection between the disks and the shaft. Yet, if the core bit jams and the clutch is slipping, the housing of the clutch will continue to rotate with the translated speed of the electric engine, while the whole drive shaft will come to a sudden halt. Without the slip-clutch the machine could be ripped out of the hands of the operator, due to the high torque and rotational inertia of the drive.

3.2.3 Force-Locked Chuck

The force-locked chuck, which connects the core bit to the shaft, has a strong influence on the dynamic system behavior and will be discussed in detail. Figure 3.7 presents a sectional CAD-view of the chuck equipped with a 25 mm core bit.

The chuck consists of an inner and an outer part, which are pressed axially together by a pre-loaded disk spring pack, thereby clamping the core bit at its connecting end in-between. The inner piece of the chuck is formed like a stepped hollow cylinder and is connected to the shaft with a thread. The mechanical connection of the core bit to the chuck is based on the circular connecting end, which slides axially into the chuck, and three connecting pins on the bit which have their corresponding sockets on the inner piece of the chuck. The outer piece of the chuck has three corresponding clips, which grab the connecting pins and pull them towards the sockets. To dismount the core bit, a lever mechanism presses the outer piece of the chuck axially “forward” against the pre-loaded spring. Doing this creates enough axial play at the connecting pins for the operator to lift the core bit out of the sockets, turn it by 60 degrees and then pull it out between the clips of the outer piece of the chuck.

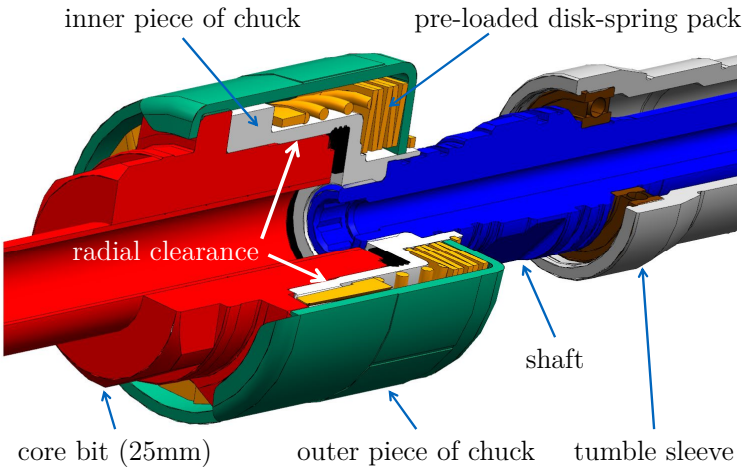

Figure 3.7: Sectional view of the two-piece chuck

Although not visible in Figure 3.7, the circular connecting end of the core bit is a little smaller in the outer diameter than the corresponding bore of the inner part of the chuck. With regard to rotordynamics, a transition fit between the connecting end of the core bit and the chuck would be desirable, with as little clearance as possible. However, such a solution would never be rugged enough for operation on a construction site: The slightest dirt, corrosion, or a small dent on the connecting end would make it impossible to mount the core bit by hand. Figure 3.8 shows some pictures that were taken on a job-site visit where the coring system is used hand-held to drill holes in railway sleepers to fasten the rails of a tram. When the tool is not used for drilling, the operators literally drop it in the dirt. Customers expect the system to work under conditions like that, which requires a robust design – meaning in the case of an interface between core bit and chuck – to provide some radial clearance. Apart from the circular connecting end, the connection between the core bit and the chuck is obtained by the three connecting pins and their counterparts, the sockets on the inner part of the chuck. In normal operation, the pins only have contact in the axial direction to the sockets, not in the tangential direction. The purpose of the chamfers on the sockets is to help the user guiding the pins into the sockets, thereby aligning the core bit in the right angular position for the clips of the outer part of the chuck to grab the pins and pull them towards the sockets. The chamfers are not intended to function as a positive connection towards the pins in order to transfer torque. The torque transfer is ensured purely by friction. The sockets are a little wider in the tangential direction than the corresponding pins, which leads to tangential play between chuck and core bit.

In the previously described design of the chuck, it is important to notice that, due to the kind of tripod design, a lateral force on the core bit will result in an axial force on the

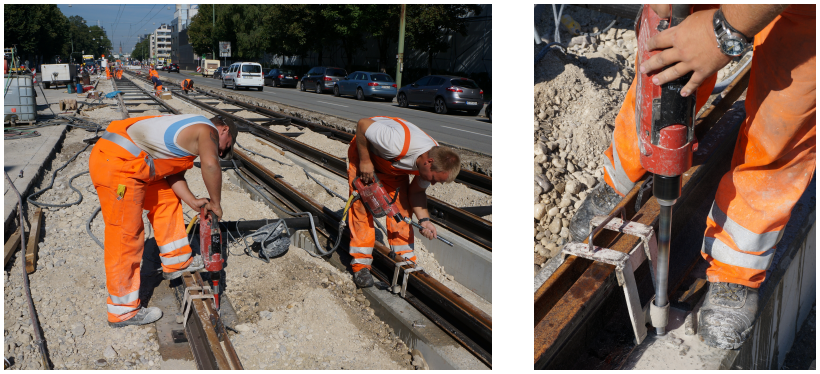

Drilling anchor holes to fasten tram rails using a drill template

Dirts and dents at the interface between core bit and chuck

Figure 3.8: Harsh conditions on a jobsite (pictures show predecessor model DD-EC-1)

connecting pins. Without regarding forces that result from drilling operation, lateral forces occur due to the natural imbalance of the core bit and from inertia forces that result from the tumbling movement. The pre-loaded disk spring pack in the two-piece chuck supplies the axial clamping forces that hold the core bit in place. Yet, if the clamping force is exceeded, the radial and tangential play in the chuck allows the core bit to tilt and slip inside the chuck. This means that the lateral stiffness of the drive shaft is strongly linked to the axial stiffness of the chuck. Furthermore, since the clamping spring is highly pre-stressed, the axial stiffness of the chuck will decrease significantly if the pre-load of the spring is exceeded; thus leading to a decrease in the drive shaft's lateral stiffness as well. In conjunction with rotation, this regressing stiffness characteristic causes strong nonlinear system behavior, leading to interesting dynamic effects like mode-locking, as will be shown in Chapter 7.4. It should be mentioned though, that within the unmodified serial product, the pre-load of the clamping-spring is sufficient to safely hold the core bit and cannot be exceeded. In the context of the underlying research, the imbalance of the core bit as well as tumble angle φ have been

significantly increased, while, at the same time, the pre-load of the clamping spring has been considerably reduced in order to provoke the rotordynamic effects mentioned above.

4 Experimental Setup

The following chapter describes the main experimental setup that is used to gain the necessary information about the dynamic behavior of the rotor system in order to evaluate the quality and the capabilities of the simulation approach outlined in Chapter 5.

At first, Chapter 4.1 focuses on the type of sensors and how they are applied. Two different setups are developed: One allows hand-held operation, the other supports the machine on a stand. The stand-based setup turned out to be necessary out of safety reasons when studying effects that create large displacement amplitudes, or large reaction forces, respectively. Subsequently, Chapter 4.2 describes the way operational measurements and experimental modal analysis is conducted in the current case. Finally, Chapter 4.3 deals with selected post-processing operations. On the one hand, these are necessary, since due to the sensor concept for measuring the rotational speed, the rpm-signals need to be corrected in an offline procedure. On the other hand, post-processing in the form of a vibrational order analysis is a powerful tool to gain a deeper understanding of the dynamic behavior of the rotor system.

4.1 Measurement Setup

The objective of the experimental setup is to study the dynamic behavior of the rotor system and to validate the simulation model outlined in Chapter 5. The focus of interest lies on the movement of the core bit relative to the machine. To study this, two different experimental setups have been used during the course of the underlying work. At first, an additional rig has been attached to the machine, which is able to support displacement sensors to measure the relative movement of the core bit during hand-held operation. Of special interest is the case, when the clamping force in the chuck is exceeded by either increasing the imbalance of the core bit or by increasing the tumble angle of the sleeve. If at the same time the clamping force is reduced, the core bit will tilt inside of the chuck, resulting in large displacement amplitudes. In fact, the amplitudes turned out to be so large, that a human operator can no longer safely hold the tool. Therefore, another experimental setup has been developed in which the machine is held by a stand. In the following, the two different setups will be described.

4.1.1 Hand-held with Additional Sensor Support Rig

Figure 4.1 shows the measurement setup with the additional rig to support the displacement sensors for the core bit. The rig consists mainly of two tubes that are connected with a bridge at their machine-sided end. To attach the rig to the machine, the telescopic bars supporting the water collector, which can be seen in Figure 3.1, are removed. The former interface of the telescopic bars allows for a very rigid connection with the machine. To further stiffen the rig, the bridge is attached with additional bars to rigid screw connections at the housing. The rig is designed in such a way, that its first local mode is located in a frequency range that is well above the maximal rotational frequency of both the tumble sleeve and the drive shaft. As will be shown later, the rig can be considered as almost rigid in respect to the housing.

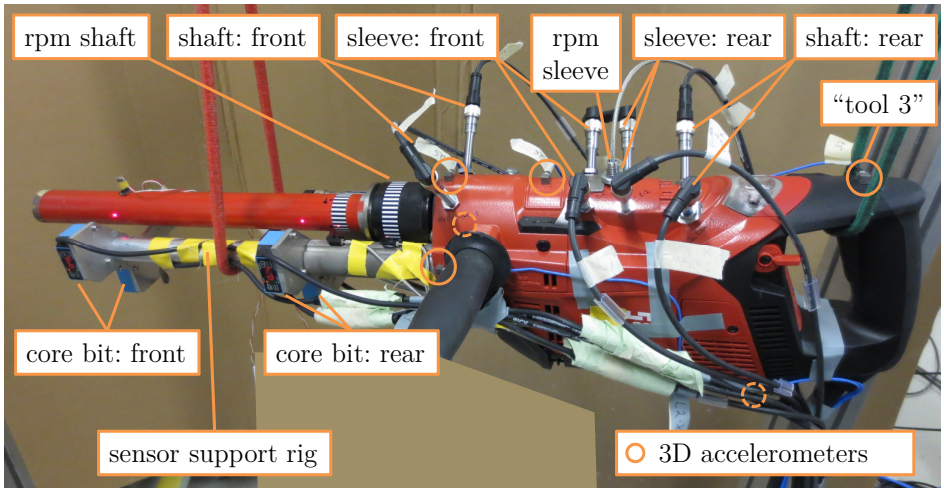

Figure 4.1: Measurement setup with additional rig for hand-held operation

Four triangulation lasers measure the displacement of the core bit relative to the rig, or to the housing, respectively. The lasers are mounted on two plates that are attached to the tubes of the rig and that can be moved alongside the tubes. The two plates carry two lasers each, one for the vertical x-direction and one for the horizontal y-direction. This allows one to track at two axial positions the motion of the core bit in the two directions perpendicular to its spinning axis. However, the use of a single-spot laser to track the motion of an object with a curved surface creates a certain measurement error: A movement of the object that is lateral to the measurement direction of the laser wrongfully creates a signal, indicating that there is also a movement in the direction of the laser, as shown in Figure 4.2a. The dimension of the error depends on the curvature of the object and the amount of lateral movement. In the underlying work, a core bit of the largest possible diameter is used to minimize the

error. Theoretically, a laser line fork light barrier would be a better sensor concept. The working principle is shown in Figure 4.2b; examples for its use on rotor systems can be found in [85, 130]. In the current case, the necessary sensor hardware is too bulky and too heavy to mount it on the rig for hand-held operation. The selected triangulation lasers are more than ten times lighter, which is the main reason they have been selected for the measurement task. Another reason is budget limitations, as the triangulation lasers are significantly less costly.

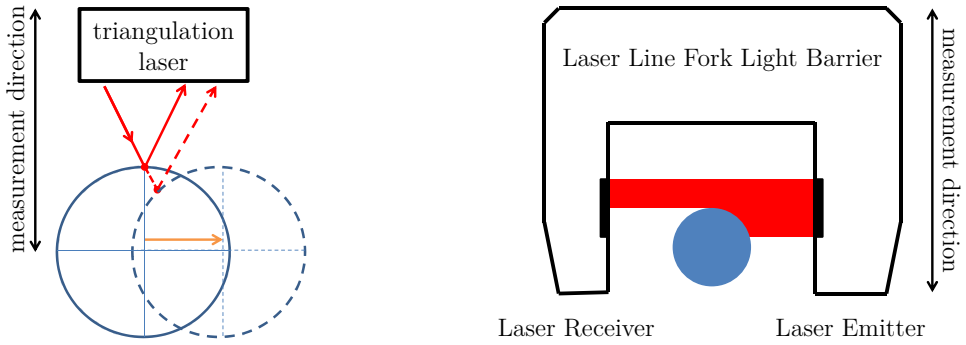

(a) error when using a single-spot laser (b) alternative sensor concept

Figure 4.2: Measuring the lateral movement of a curved object

For measuring the displacement of the shaft and the tumble sleeve, basically the same concept as for the core bit is used, which means spanning a plane perpendicular to the axis of rotation at two different axial positions with two sensors each. With the sole difference that here inductive displacement sensors are applied instead of triangulation lasers. Since the shaft rotates inside the hollow tumble sleeve, it is accessible only at its ends. Figure 4.3 shows the position of the inductive sensors. The “front” side of the shaft is measured at the housing of the slip clutch. The movement at the “rear” end is tracked at the swivel of the water intake. Therefore parts of the swivel that rotate with the shaft are replaced with a steel cylinder to provide a good signal. The tumble sleeve is accessible only within a short range of its total length at positions that are close to the bearings. For both the shaft and the sleeve, the machine design does not allow the sensor to be oriented parallel to the coordinate axes, as in the case of the triangulation lasers. Instead, the inductive sensors are mounted under an angle of 45 degrees with respect to the xz-plane.

In preparation of the measurement setup, a modal analysis revealed that, within the frequency range of the rotational speed, the housing of the machine has no structural modes and mainly performs a rigid body motion. Therefore it is possible to measure the movement of the machine with acceptable precision by using accelerometers. Six triaxial accelerometers

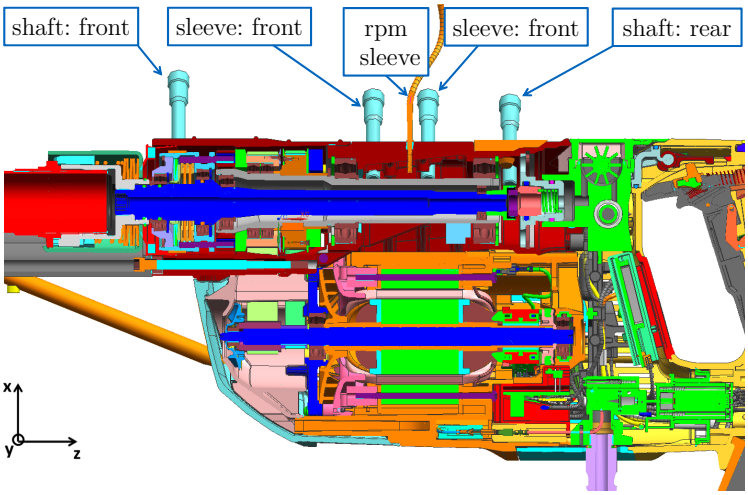

Figure 4.3: Position of the inductive displacement sensors

cover the movement of the housing, while another two triaxial sensors monitor the movement of the rig at the two mounting plates of the triangulation lasers. For modal testing at non-rotating condition, additional accelerometers are used on the core bit and on the chuck.

The rotational speed of the shaft and the tumble sleeve is recorded by the use of optical sensors in combination with striped tape, so-called "zebra tape", which is wrapped around the rotating bodies. The major advantage of this measurement method, compared to an incremental encoder, is the ease of application on any part that is optically accessible. Also, there is virtually no weight added to the rotating parts and no extra space is needed. On the other hand, at the joint of the zebra tape there is always one stripe that is larger (or smaller) than the other stripes, which are evenly distributed. In the underlying work, the larger stripe is used to determine the rotor's absolute angular position. However, the somewhat larger stripe also represents a discontinuity, which creates an artificial fluctuation in the signal of the rotational speed. Partly, this fluctuation can be averaged out with a post-processing algorithm, but not completely. While the tumble sleeve is accessible by drilling a hole in the housing, access to the shaft is more restricted. Therefore the rotational speed of the shaft is taken at the outer piece of the chuck, which rotates at the same speed as the shaft.

On the hardware side, data acquisition is done with a frontend of type SCADAS Lab from manufacturer LMS, using up to 60 measurement channels. The data is then post-processed and analyzed with LMS Test.Lab and Matlab.

4.1.2 Stand Based

Exceeding the clamping force of the chuck during rotation results in large reaction forces that need to be compensated by the human operator. This might easily lead to dangerous situations. Therefore, another test setup has been developed, in which the machine is held by a stand and the displacement sensors for the core bit are placed on the ground. A picture of the setup is shown in Figure 4.4. The stand holds the machine at the screw connections for the side handle, which are available on both sides since the side handle can be mounted either for left or right-handers. Rubber-bonded-to-metal components are used for the connection. At the rear end, the machine is supported by a mount of elastic material, which has been formed by the rear handle in a casting operation. The challenge is to support the machine rigidly enough to ensure safe operation, while, at the same time, keeping the rigid body resonances of the machine in the support low enough in frequency to allow a clear separation between support and structural resonances. The displacement of the core bit is again tracked by triangulation lasers – this time fixed to the stand, therefore measuring in an absolute coordinate system. This is in contrast to the hand-held measurement setup in Chapter 4.1.1, in which the lasers are attached to the machine via the additional rig, and therefore reference a local, machine-based coordinate system.

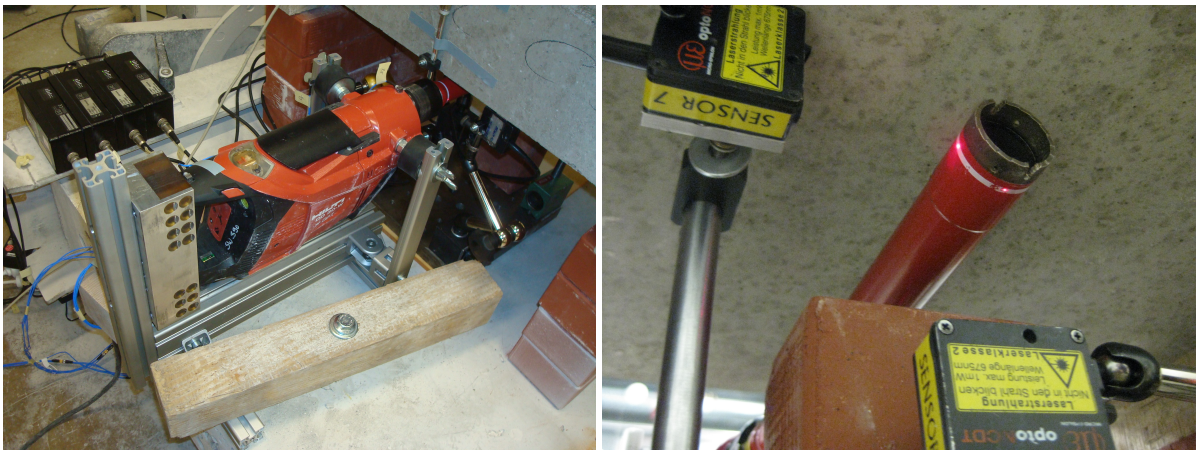

Figure 4.4: Measurement setup in which the machine is supported by a stand

4.2 Test Setup

While in the previous section the experimental setup was described with respect to the applied sensor systems, here the focus lies on how the actual measurements are performed and how the data is post-processed to aggregate the obtained information.

4.2.1 Operational Measurements

One of the main objectives of the underlying research is to study the dynamic system behavior when crossing a bending resonance during run-up and run-down. The tests are performed without a drilling operation, which means that the core bit can rotate freely without any contact with the underground. As a matter of protection, a kind of bunker contains the core bit when the tool is running. Although a person of average physical strength is able to safely hold the tool including the extra weight of rig and sensors, additional elastic cords support the weight of the system in order to relieve the operator during hand-held measurements. Figure 4.5 shows the corresponding test setup. For stand-based measurements, the setup corresponds to that in Figure 4.4.

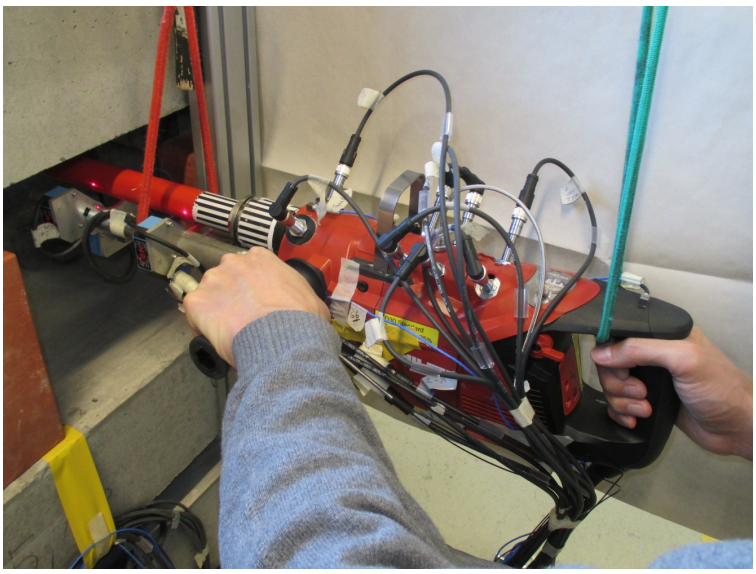

Figure 4.5: Test setup for hand-held measurements

During tests, the rotational speed is indirectly controlled through the voltage supply of the electric drive. To run up the tool, voltage is ramped-up in a linear manner. The same applies accordingly for a run-down. However, even if there is no external load on the core bit, the rotational speed cannot be perfectly controlled through the voltage supply. When crossing the critical speed of the resonance, part of the energy that is fed to the electric drive is transfered into the lateral bending motion, instead of further accelerating the spinning motion. This phenomena is known as the *Sommerfeld-Effect* [28], named after Arnold Sommerfeld (1868 - 1951), and will be discussed in Chapter 7.4.3.

4.2.2 Experimental Modal Analysis (EMA)

Experimental modal analysis (EMA) is a powerful tool to study the dynamic behavior of a vibrating system and to validate and update theoretical models. Nowadays, it can be considered a standard approach in research and in the industry. The procedure is described in many textbooks and will not be repeated here. The works of *Ewins* [31] and of *Maia* and *Silva* [89] are well accepted and frequently cited. In the underlying research, EMA is used to analyze single parts of the rotor system, certain assembly groups, as well as the complete test setup as a whole. This chapter describes, how the FRFs have been measured and how they have been analyzed. Chapter 6 discusses the results of the modal analysis.

EMA generally consists of two steps: First, FRFs need to be measured in decent quality at sufficient positions of the structure to geometrically resolve the mode shapes within the frequency range of interest. In a second step, the modal parameters are extracted by using the appropriate identification methods. In the underlying thesis, the single components are measured in free boundary conditions as described in Chapter 4.2.2. The so-called PolyMAX algorithm is then used to estimate the modal parameters. PolyMAX is a polyreference least-squares complex frequency-domain method that was introduced in [50] and can be considered a benchmark in modal parameter estimation [108, 109]. One of the advantages of the algorithm is the fact that it allows one to separate closely spaced modes. This fact comes in handy with rotordynamic problems, in which, due to the more or less symmetric geometry of typical rotors, double modes are the rule and not the exception.

Single components are measured with free boundary conditions, which is also the most common approach [31, 110]. Figure 4.6 shows, as an example, the test setup for FRF measurements on the shaft. The roving hammer technique is applied, using two accelerometers (two references) to identify the double modes of an (almost) axial symmetric object.

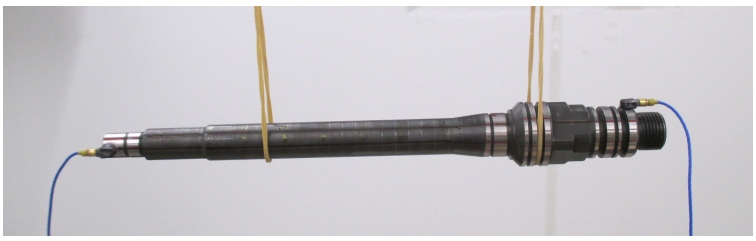

Figure 4.6: Test setup for FRF measurements on the shaft in free boundary conditions

Impact testing is also applied to measure FRFs on the system as a whole. The focus of interest lies on the first bending mode, which is a global mode, as will be shown later. The

roving-hammer method is used to identify the bending mode, as well as to study the dynamic behavior of the housing and the hand-grips of the machine in detail. In total, 156 points are measured. The measurements are performed at a standstill with free boundaries conditions, when the system is simply supported by the elastic cords mentioned before.

In addition, measurements are performed while a human operator holds the tool to catch the influence of the user on the modal parameters. Therefore, an operator grips the tool at first just at the rear handle, then just at the side handle, and, finally, applies a grip at both handles. The measurements are repeated for different amounts of gripping force. To avoid repeating the FRF measurements for all cases at all 156 points, the results of the detailed EMA are first evaluated: The system shows no other modes in the frequency range of interest other than the bending mode mentioned before. That means that the previously described sensor setup for operational measurements allows one to identify the bending mode with a single excitation point. Good excitation points turned out to be the front end of the core bit and the top side of the rear handle.

4.3 Post-Processing of Operational Measurement Data

4.3.1 Deriving the RPM-Signal

Gaining an accurate signal of the rotational speed is essential and also provides the base for any further analysis. In the current project, two optical incremental encoders are used to record the rpm signal of the shaft and of the tumble sleeve. Tape with equidistantly-spaced black and white stripes – so called *zebra tape* – is wrapped around the outer piece of the chuck and around the tumble sleeve. During rotation, the tape acts as a coder: An optical probe detects the passing of the black and white stripes, transferring it into a square wave signal, thereby creating a pulse train, as in Figure 4.7. In a post-processing operation, the pulse train is transferred into a rpm signal by simply dividing the rotational angle that corresponds to one stripe by the time needed to pass the optical sensor. Since the encoder creates several pulses per revolution, this method generates a signal of sufficient accuracy.

Zebra tape is straightforward to install, but has one major disadvantage that needs to be taken care of. At the location where the two endings of the tape come together, it is inevitable to create a stripe that is either slightly smaller or larger than the other stripes. When this so called *butt-joint* passes the optical sensor, it will introduce a discontinuity in the pulse train and thereby also in the rpm signal. This results in two errors. The obvious thing that happens, is the fact that even at constant rotational speed, the butt-joint will have a

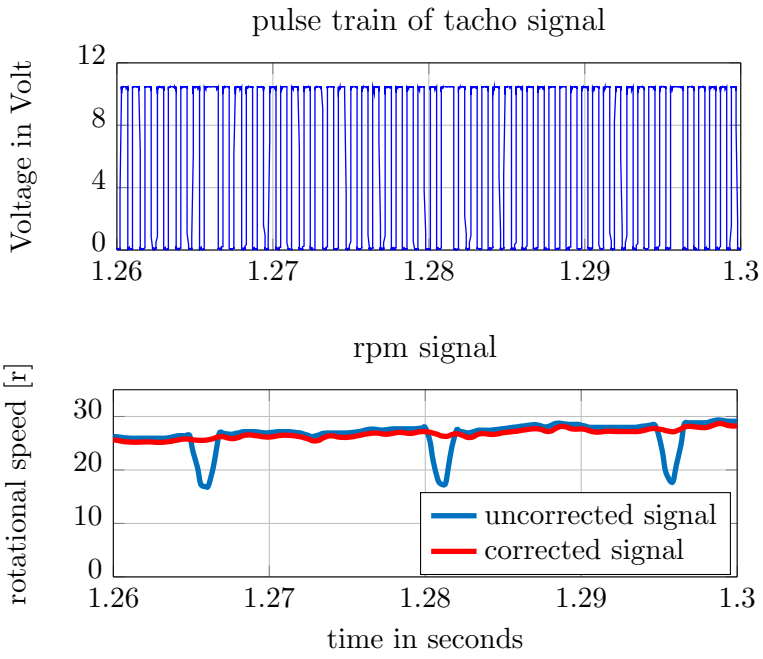

Figure 4.7: [Meas][1]Error in the rpm signal due to the *butt-joint effect* and its correction

different passing time than the other stripes, which is misinterpreted as a fluctuation in the rpm signal. The second error results from the assumption that, in a tape with equidistantly spaced stripes, the peripheral angle corresponding to a single stripe can be calculated by simply dividing 360 degree (respectively 6.28 rad) by the total number of stripes. If one stripe is larger than the others, this assumption is violated because that actually means that all other stripes are in fact smaller than in the calculation just mentioned, leading to an error in which the rpm is calculated as too high. If the butt-joint is smaller than the rest of the stripes, it is the other way around, meaning that the rpm value is wrongfully calculated as too slow. In the underlying thesis, the rpm signal is corrected in a post-processing operation as described in [61]. The method allows one to eliminate both errors as can be seen in Figure 4.7.

The butt-joint issue is, however, not only a nuisance. The discontinuity created by the butt-joint provides information about the absolute position of the corresponding rotor. This way, the optical encoder measures not only the rotational speed, but also allows one to calculate the angular position by dead reckoning after the passing of the butt-joint. This information is essential for determining the imbalance of the drive shaft, as will be described in Chapter 7.2.1.

[1]In the further course of the thesis, captions of result plots will be marked by either [Meas] to indicate measurement data, or by [Sim] to indicate simulation results.

4.3.2 Order Analysis

When dealing with a vibrational problem, measurement data is usually analyzed in time and in frequency domain. In rotordynamics, significant dynamic events might repeat with each revolution and at a specific angle, like in the case of an imbalance excitation. Therefore, the time signal, and more importantly, the frequency content of the signal, depends on the rotational speed of the rotor, making it difficult to assign the dynamic response of the structure to a certain excitation mechanism. A helpful instrument in this case can be a so-called (vibrational) *order analysis*. In rotordynamics, *orders* are considered harmonics of the rotational speed, so the terminus first order refers to a sinusoidal vibration with the same frequency as the rotational frequency of the corresponding rotor. When analyzing the vibrational response of a structure, an order analysis allows one to determine the amount of vibration that is related to the different orders at varying rotational speeds, thereby creating a better understanding of the structural response to the different excitation mechanisms.

A vibrational order analysis usually requires one to record the signal at constant increments of shaft angles. Alternatively, software algorithms can be used to resample data that has been recorded at uniform time intervals Δt to data at constant angular increments [9, 11]. However, both methods require a high-resolution rotary encoder which is not available in the current measurement setup. Therefore, a different approach is used: First, the data is recorded at uniform time intervals. Then, in a post-processing operation, a tracking algorithm determines the instants of time at which the rotor(s) run at a certain rotational speed. Uniform rpm-increments (decrements during run-down) are used, i.e. every 10 rpm. After that, a time interval around the relevant instant of time is cut out of the measurement data and transformed into the frequency domain. Finally, the frequency content corresponding to the order of interest is evaluated.

The applicability of the afore mentioned approach depends very much on the slope of the rpm-curve and on the length of the time interval that is cut out at each rpm-increment to be transformed in the frequency domain. If the slope is very steep and/or the time interval is long, the time blocks will overlap each other and will thereby smooth out peaks in the order-signal. The length of the time interval depends on the desired frequency resolution, which in turn depends on the maximum order of interest. In the current case, the focus of interest lies on the first orders of the three rotors, the drive shaft, the tumble sleeve and the electric engine, as will be shown in Chapter 7.1. Therefore, the necessary length of the time interval can be kept rather short, making the approach described above suitable for the current problem.

5 Simulation Model

The current section outlines the simulation model of the diamond coring system. Starting from a description of the general approach, further explanations consecutively go into modeling details of the rolling element bearings, the force-locked chuck, power train, mechanical sealing and conclude with the model representation of the human operator.

5.1 General Model Approach

Within this thesis, a diamond coring system acts as an application example to demonstrate the capabilities and the need for 3D solid modeling in rotordynamics. In contrast to an academic rotor test stand, the diamond coring system outlined in Chapter 3 is a real-world machine with a rather complex mechanical design consisting of more than one-thousand individual parts. This makes it hardly possible to model each single component and its interaction with surrounding parts in detail. When it comes to generating a model to study the dynamic behavior of such a complex system, certain assumptions and simplifications need to be made. Therefore, it is essential to first define the purpose and system boundaries of the model in order to determine the level of refinement necessary to achieve the objects. Within this thesis, the focus of interest lies on a bending resonance of the rotor system that occurs during operation. The purpose of the model is to correctly describe the global dynamic behavior of the rotor system during run-up and run-down when the machine is either hand-held or supported by a test stand. The research is limited to the case in which the core bit has no contact with the underground. The system boundaries are drawn around the actual power tool including the core bit, but excluding the supporting rig from Figure 3.1.

In the sense of modeling abstraction, the diamond coring system can be regarded as a system of interconnected bodies, parts of which undergo rather large elastic deformations, what makes it fall under the discipline of flexible multibody dynamics [44]. One thing that makes this rotor system special is the fact that one of the two rotor sub-systems – the drive shaft – consists of an assembly group comprising several parts. Within this assembly group, the core bit is connected to the shaft via a force-locked chuck. If the clamping force of that chuck is exceeded during operation, the core bit will perform movement relative to the chuck and the shaft. The model is supposed to correctly describe the dynamic behavior even in the latter case. Due to the complex geometry of the two-piece chuck as well as the connecting end of the core bit, correct interaction between these parts can only be achieved by using 3D solid modeling. This is one of the reasons, why a nonlinear finite element approach is chosen

to model the rotor system. Other reasons to use 3D solid finite elements in rotordynamics are named in Chapter 2.

One of the advantages of 3D solid finite elements is the possibility to directly use the CAD-geometry of the parts, thereby reducing the modeling effort. Still, it is virtually impossible to include every part of the diamond coring system in full detail. The effort for meshing would be too high and the computational costs would render the simulation model unsolvable within reasonable limits. Since the focus of interest lies on the bending resonance and with the help of experimental results from Chapter 4.2.2, detailed modeling can be restricted to those components that undergo elastic deformation in the first bending mode. The result of the modeling process is shown schematically in Figure 5.1 and will be described in what follows. First, a general overview of the model is given, followed by a look into certain specifics, as described in the survey at the beginning of this chapter.

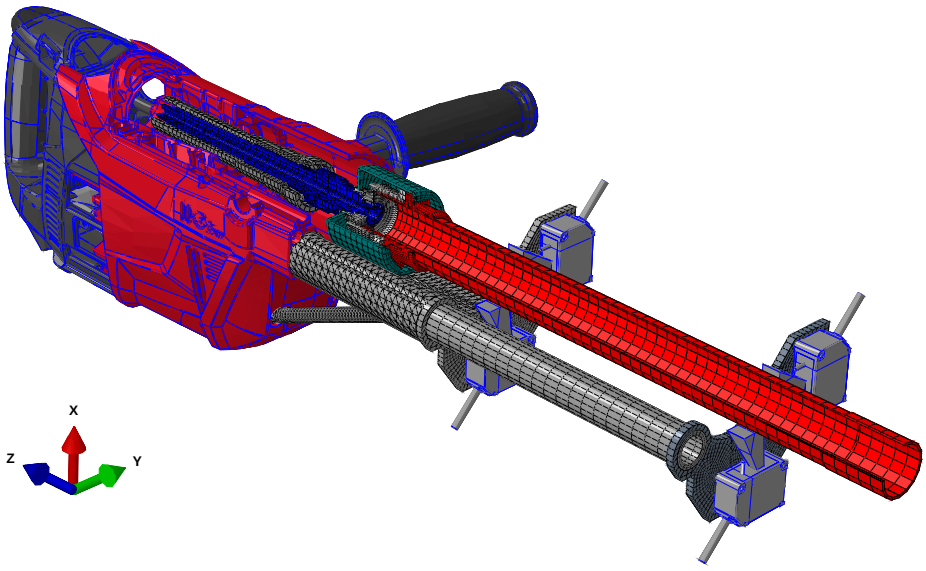

Figure 5.1: Sectional view of the FE-model

On a certain level of abstraction, the components of a rotor system can simply be divided into rotor, stator, bearings and supports. As one can imagine and as will be shown in Chapter 7.1, almost all rotating parts undergo elastic deformation in the bending resonance and are therefore modeled in detail. The way to deal with the interaction between the core bit and the force-locked chuck, as well as the connection between the shaft and the chuck, will be described in Chapter 5.2.3. In the frequency range of interest, the stator – consisting of the casing and generally of all parts that do not rotate – can be regarded as rigid. It is therefore modeled as a point mass with moments of inertia. The sensor rig has been

deliberately designed to behave rigidly in the frequency range of interest and is therefore also represented as a point mass with corresponding moments of inertia. The rolling element bearings turn out to play an important role in the mechanical behavior of the whole system. They are modeled as a spring-damper system with nonlinear stiffness characteristics, as will be explained in detail in Chapter 5.2.2. The fact that the simulation model is supposed to include the boundary conditions provided by a human operator holding the machine in his hands has the potential to cause headaches. However, in this thesis, the operator is represented as a simple spring-damper system with linear characteristics. Why this is justified in the current case will be explained in Chapters 5.2.6 and 6.2.3.

5.2 Modeling Certain Components and Implementation in ABAQUS

Subsequent chapters use visualizations of the finalized FE-model to describe the modeling of certain mechanical details, as of the force-locked chuck or the bearings. Prior to that, the current section deals with the implementation of the model.

The simulation model is implemented in ABAQUS, which is a commercial general-purpose FE-code. ABAQUS offers, amongst other things, superb 3D solid modeling capabilities and all functionalities necessary to deal with nonlinear flexible multibody dynamics, such as, for instance, formulations for joints and contacts.

5.2.1 General Overview

The single components of the rotating subsystems are modeled in full detail, with only small simplifications regarding their geometry, such as ignoring small chamfers and alike. Figure 5.2 shows some sketches of the rotating parts and how they are represented in the FE-model. Regarding mesh and element type: The mesh is structured where reasonable, and it is made mostly out of 20-node brick elements with quadratic shape functions (C3D20). In order to keep a structured mesh, some 15-node quadratic triangular prisms ("wedges", C3D15) are necessary. The use of quadratic elements initially increases the number of nodes, and seemingly with it, the computational effort. However, when compared to linear elements, convergence is much improved, especially in regions with contact to neighboring parts, and a lesser amount of total element numbers is needed. With quadratic elements, for instance, a single layer of elements over the thickness of a hollow pipe-like object is sufficient to adequately represent the lower structural modes. Therefore, the overall computational costs are lower under the use of quadratic elements. Regarding mesh size, it becomes evident that the

mesh in Figure 5.2 is too coarse to evaluate local stress or include plastic material behavior. The primary objective is to accurately describe the global system behavior during run-up and run-down of the rotor system. Therefore, a coarse mesh is used to save computation time in the beginning. Once this is achieved, a finer mesh could be used to correctly compute the local stress distribution, e.g. for lifetime analysis (which is beyond the scope of this thesis).

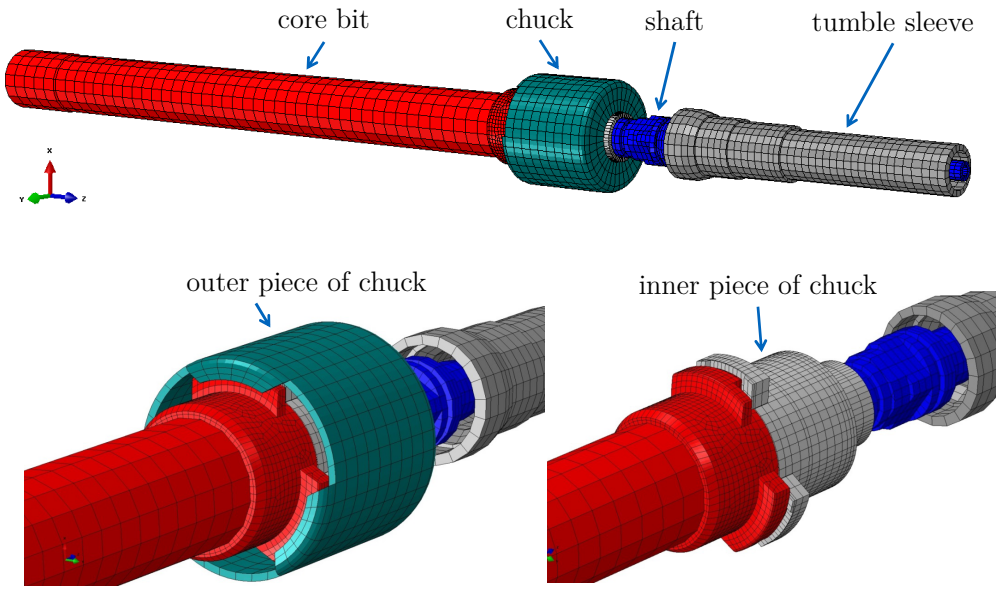

Figure 5.2: Sketches of the rotating parts in the FE-model

The single components of the rotating parts are held together by:

- a clamping mechanism (connection between core bit and two-piece chuck),
- a thread (connection between inner piece of the chuck and shaft),
- and by deep-groove ball bearings (connection between shaft and sleeve as well as between sleeve and housing).

In addition, the drive train contains elastic elements, such as the rubber joint or the two toothed belts. And after all, a human operator needs to be somehow taken into account. In ABAQUS,

- contacts,
- ties,
- multi-point constraints
- and connectors

are used to represent these features, as will be described in detail in the subsequent chapters.

5.2.2 Deep-Groove Ball Bearings

The following sections describe the model approach for the deep-groove ball bearings, the way the load-displacement curves are calculated, and how the damping is estimated.

5.2.2.1 Model Approach

When it comes to modeling bearings in a rotordynamic analysis, one can observe different levels of detail, which will be described in what follows.

In its simplest form, rolling element bearings are described as perfectly rigid boundary conditions for the shaft. This approach is often used to explain the fundamentals of rotor dynamics, for instance, with the help of a Jeffcott rotor model, which assumes the shaft to be flexible and the bearing behavior to be perfectly rigid, as it can be found amongst others in [76]. However, in the real world, all bearings are flexible to a greater or lesser extent, and it is a matter of the stiffness relation between the rotating parts and the bearings, whether the later need to be modeled as flexible or can be considered as rigid. If the stiffness of the bearings is larger by at least one order of magnitude than the stiffness of the shaft, the simplification of rigid bearings can be justified according to [35]. Although at first glance, rigid bearing behavior seems to be easier to account for in the model, a large difference in magnitude between the shaft and the bearing stiffness might result in numerical difficulties [33], and therefore might slow down convergence in an FE-approach.

In many cases, the assumption of rigid behavior is inappropriate, and the bearings are usually described as spring-damper systems. A vast quantity of research has been conducted on how to calculate or measure the dynamic parameters of rolling element bearings, as will be outlined briefly in the next section. For now, a more basic issue of the modeling approach shall be addressed: In many works, rolling element bearings are regarded as purely translational stiffness elements, having no angular stiffness, commonly called *short bearings* [33]. The question is whether such a simple approach is sufficient in the current case. The diamond coring system regarded here is equipped with deep-groove ball bearings. These bearings come naturally with a certain amount of tilting play, which might justify treating the tilting stiffness as zero. However, preliminary experiments have revealed that the system – modified with additional imbalance and reduced clamping force in the chuck – undergoes considerable displacement amplitudes within the bending resonance, most certainly exceeding the tilting play in the bearings. Experiments had also revealed that the bearings play an important role in the global dynamic behavior of the system. Using the same bearing type

but from different manufacturers results in significant differences with regard to core bit tip displacement during run-up and run-down. Therefore, the approach of using short bearings is dropped. This requires one to evaluate the tilting stiffness of the bearings, which can be quite challenging, as seen in the next chapter. First, the implementation of the bearing model in ABAQUS is outlined.

When using beam-elements to represent shafts of a rotating system, implementing the bearings is straight-forward: First, a node is placed at the position of the bearing seat along the shaft. Then, this node is connected to the stator with a spring element. In the case of 3D solid modeling, things are a little more complicated, since the bearing seat is not represented by a single node or element. The solution involves using multi-point constraints (MPCs). First, a so-called master node is created, which single-handedly represents a bearing seat on the shaft. Subsequently, this node is linked to an equivalent node of the stator - or, in the current case, to an equivalent node of the (hollow) tumble sleeve. In ABAQUS, the surface, coupling and connector functionality is used to represent the bearings, as shown in Figure 5.3. First, a surface is defined at the position of the bearing seats. In the center of the bearing seat, a reference point is defined, acting as the master node mentioned above. Then, the DOFs of the surface nodes are linked to the master node, using the coupling function, which formulates the necessary kinematic constraints. In turn, the two reference nodes that belong to a corresponding couple of an inner and outer bearing ring (or rather bearing ring seat) are linked by a connector element, which represents the spring-damper system. In this approach, the bearing itself does not appear as a solid body in the model. The mass and rotary inertia can be distributed on the two master nodes forming a bearing. The two reference points are positioned at exactly the same geometric position (in undeformed configuration); it is just for better visualization that they have been separated in Figure 5.3.

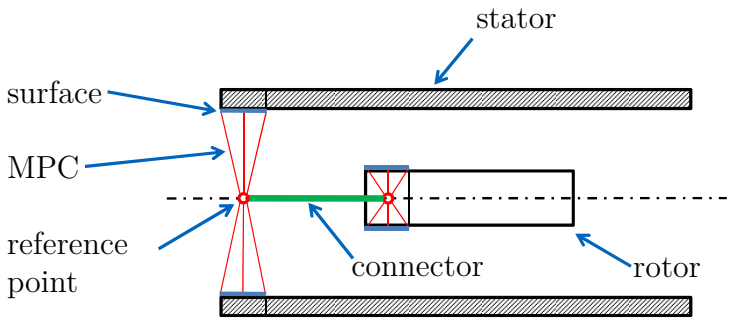

Figure 5.3: Schematic diagram of the bearing model

Going back once more to the coupling function, which creates kinematic constraints between

nodes: Different ways of enforcing the corresponding constraints can be chosen. In ABAQUS, the terminus "kinematic coupling" refers to rigid constraints between the master and the coupling nodes, which would turn parts of the shaft and the stator into rigid bodies, therefore increasing the stiffness significantly, depending on the axial length of the defined surface, or the bearing seat, respectively. As an alternative, ABAQUS offers "distributed couplings" in which the constraints are enforced in an average sense and weighting factors provide control of the load transmission. In the current thesis, distributed couplings are chosen to model the bearings. This still creates a stiffening effect, which, in the end, is well appreciated, since it allows one to take the added stiffness resulting from the press fit of the bearing rings into account.

5.2.2.2 Calculating the Load-Displacement Curves

The dynamic parameters of the spring-damper system representing the bearings can either be identified by experiments or by using theoretical or numerical models. Here, the latter approach is taken. A vast quantity of research has been conducted on how to calculate the dynamic parameters of rolling element bearings. Literature by *Harris* [54], *Jones* [62], *Palmgren* [107] and *Eschmann* [30] on theoretical models is considered to be well accepted by a number of authors. The origins of these works range back to a time without computers or with limited computational resources, resulting in models that can be solved analytically or with manageable numerical or graphical effort. However, this comes at the price of several simplifications in geometry and in assumptions of the contact situation between rolling elements and bearing races. While the models are able to calculate the translational stiffnesses, they lack the capability to accurately estimate the tilting stiffness and the cross-coupling between the different DOFs of a bearing.

The focus of early models lay more on lifetime considerations and in providing boundary conditions in rotordynamic analyses. Current research is often driven by the wish to monitor a machine's condition by analyzing, for instance, structural-born sound on the casing. For that purpose, more refined bearing models are needed that are able to explain the transfer of vibration from the rotating parts onto the housing. This resulted in the widely accepted model by *Lim* and *Singh* [81–84], which was later improved by *Liew* and *Lim* [80]. The authors realized that to correctly describe vibration transmission through rolling element bearings, the model needs not only to include the tilting stiffness, but also the cross-coupling between the different DOFs of a bearing. The result of their works is a model that provides a fully populated [6x6] linearized stiffness matrix (while the line and the column of the DOF of

the spinning axis are zero). An example of the successful application of the approach on a real-world problem can be found in [53]. However, the approach by *Liew*, *Lim* and *Singh* has two major disadvantages with regard to the current problem: First, it cannot take into account some geometric data of the bearing rings, which are known to significantly influence the bearing stiffness [51]. The preliminary experiments described above (using the same bearing type but from different manufactures), had already shown that the diamond coring system reacts very sensitively to the bearing geometry, obviously requiring one to take the exact geometry into account. The second major setback is the fact that the model delivers only a linearized stiffness matrix. With the system being so reactive to the bearing's stiffness characteristic, a nonlinear approach is desired. In the end, none of the abovementioned theoretical models is used. Instead, the load-displacement curves are derived by using substitute 3D solid models of the bearings and performing static load simulations. To determine the exact geometry, the bearings are dissembled and the single parts are measured on a highly precise tactile 3D coordinate measurement machine. This approach even allows one to consider wear on the bearings, as the race curvature does not need to be of circular shape but can in fact have any form.

Once the precise geometry of the bearings is known, the calculation of the load-displacement curves can begin. The analysis consists of three steps:

1. Step one calculates the static stiffness of the machine casing which supports the tumble sleeve.
2. Step two calculates the deformation of the bearing rings due to the press fit.
3. In the third step, a static load is applied and the relative displacement between inner and outer bearing ring is evaluated. For the bearings supporting the tumble sleeve, the outer bearing ring is supported by a spring that is given the stiffness evaluated in step one.

Step one: Calculating the stiffness of the machine casing

The stiffness of the casing is evaluated using a substitute 3D solid FE-model in ABAQUS, as shown in Figure 5.4. The simulation is limited to the part of the casing that actually supports the tumble sleeve. In the model, this part of the casing is rigidly supported at the connecting points to the rest of the machine, consisting mainly of 4 screw domes. The surface of the bearing seats are then linked to a single master node using the *coupling* function, as previously described in Chapter 5.2.2.1. The only difference is the way to enforce the

distributed couplings that link the DOFs of surface nodes of the bearing ring seat to the single master node. Here, *kinematic constraints* are used, assuming rigid behavior of the outer bearing rings. The compliance of the bearing rings is taken into account in step two of the simulation. Finally, a static force is applied to the master node and the displacement is evaluated. This is done sequentially for all 5 DOFs and for both bearings. Since the geometry is rather complex, tetrahedral elements of type C3D10 are used to mesh the casing.

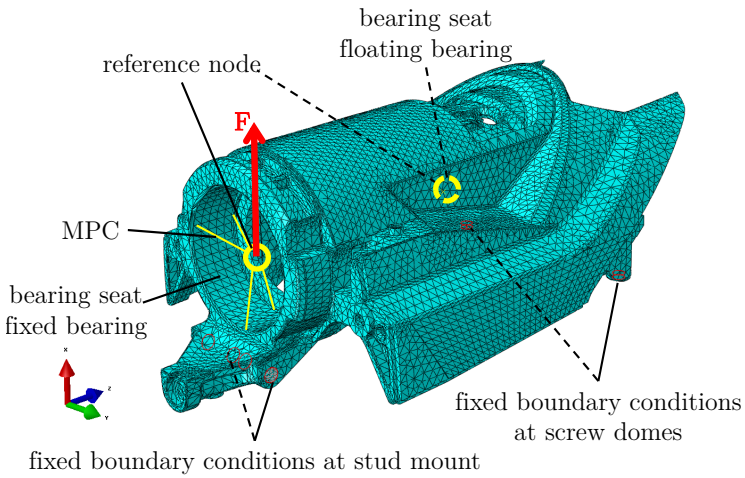

Figure 5.4: FEM sub-model to calculate the stiffness of the machine casing

Step two: Calculating the deformation of the bearing rings due to the press fit

Internal bearing clearance has a crucial influence on the load-displacement curves. However, what really matters is the operating clearance of the bearings and not the clearance in undeformed configuration. The press fit of the bearing rings will cause the outer ring to narrow down, while the inner ring will be widened by the shaft. With common fittings for the bearing seats, the installation clearance is much lower than the internal bearing clearance in undeformed configuration. This must be taken into account when calculating the load displacement curves. In operation, internal bearing clearance can be further reduced if there is a recognizable difference in temperature between the inner and the outer bearing ring. Such a temperature difference might occur if the machine has not yet reached a steady state operating temperature or when the cooling concept produces a nonuniform temperature distribution. In the current case, the latter is not unlikely, since, for example, the shaft is flushed by cooling water, while the rest of the machine is air cooled in an open circuit. However, all experimental tests are performed without cooling water and with the machine well warmed up. Therefore a potential temperature influence on the operating clearance of

the bearings is ignored.

The deformation of the bearing rings due to the press fit can either be calculated by an analytical approach or by another FEM substitute model. To save computational effort, this time an analytical approach comes into play. Often, bearing seats consist of the same material as the bearing ring itself, allowing one to use simple formulas or empirical values as provided from certain bearing manufacturers. In the current case, things are a little more complicated, since the casing is made out of a magnesium-aluminum alloy, which has different material properties than the bearing rings. *Harris* offers an appropriate approximation by using thick ring theory; the following formulas are taken from [54]. A declaration of the variables succeeds the equations.

The contraction Δ_h of the bore of the outer bearing ring due to a press fit can be approximated with

$$\Delta_h = \frac{2I\frac{D_h}{D_2}}{\left[\left(\frac{D_h}{D_2}\right)^2 - 1\right]\left\{\left[\frac{\left(\frac{D_h}{D_2}\right)^2+1}{\left(\frac{D_h}{D_2}\right)^2-1} + \xi_b\right] + \frac{E_b}{E_h}\left[\frac{\left(\frac{D_1}{D_h}\right)^2+1}{\left(\frac{D_1}{D_h}\right)^2-1} - \xi_h\right]\right\}} \tag{5.1}$$

If the bearing outer ring is pressed into a housing of the same material (as is the case with the bearings of the shaft, which are pressed into the tumble sleeve), Equation (5.1) simplifies to

$$\Delta_h = I\left(\frac{D_h}{D_2}\right)\left[\frac{\left(\frac{D_1}{D_h}\right)^2 - 1}{\left(\frac{D_1}{D_2}\right)^2 - 1}\right] \tag{5.2}$$

The increase Δ_s of the bearing inner ring mounted on a shaft can be approximated with

$$\Delta_s = \frac{2I\frac{D_h}{D_2}}{\left[\left(\frac{D_1}{D_s}\right)^2 - 1\right]\left\{\left[\frac{\left(\frac{D_1}{D_s}\right)^2+1}{\left(\frac{D_1}{D_s}\right)^2-1} + \xi_b\right] + \frac{E_b}{E_s}\left[\frac{\left(\frac{D_s}{D_2}\right)^2+1}{\left(\frac{D_s}{D_2}\right)^2-1} - \xi_s\right]\right\}} \tag{5.3}$$

If the bearing inner ring and shaft are made out of the same material, Equation (5.3) simplifies to

$$\Delta_s = I\left(\frac{D_1}{D_s}\right)\left[\frac{\left(\frac{D_s}{D_2}\right)^2 - 1}{\left(\frac{D_1}{D_2}\right)^2 - 1}\right] \tag{5.4}$$

In the equations above, the variables have the following meaning:

Δ_h clearance reduction due to press-fitting of bearing in housing,

Δ_s clearance reduction due to press-fitting of bearing on shaft,

ξ Poisson's ratio (subscripts: b for bearing ring, h for housing, s for shaft),

D_1 outside diameter of outer ring,

D_2 inside diameter of inner ring,

D_h basic housing bore,

D_s basic shaft diameter,

E modulus of elasticity (subscripts: b for bearing ring, h for housing, s for shaft),

I interference.

If a bearing has a radial clearance of P_d before mounting, the reduction of the clearance ΔP_d due to the mounting is given by

$$\Delta P_d = -\Delta_s - \Delta_h \tag{5.5}$$

Step three: Calculating the load-displacement curves of the bearings

Based on the geometry information obtained by using a highly precise tactile 3D coordinate measurement machine, an FE-model of the inner and outer bearing ring and of the steel balls is set up. The cage and the sealings are ignored. Contact formulations are established between the steel balls and the bearing rings. The mesh consists of 20-node brick elements with quadratic shape functions (C3D20). Although the mesh is quite refined, it is still too coarse to correctly calculate the local stress distribution needed for a lifetime calculation. For computing the *relative* displacement between the inner and outer bearing ring, the mesh is well suitable, however. Next, MPCs are applied to the nodes of the inner surface of the inner bearing ring and to the nodes of the outer surface of the outer ring. These surfaces are referenced on a single master node each, as described in Chapter 5.2.2.1 and illustrated in Figure 5.3. The two master nodes can now be used to apply loads and boundary conditions to calculate the desired nonlinear load-displacement curves. In the case of the shaft bearings, the master node of the outer bearing ring is fixated, while the force, or the torque, respectively, is applied to the master node of the inner ring. For the bearings of the tumble sleeve, the master node for the outer bearing ring is attached to a linear spring with the stiffness of the housing, which was calculated in step one of the analysis.

Figure 5.5 shows the FE sub-model in the form of a stress distribution due to a lateral force and a moment. The plot in Figure 5.6 contains the load-displacement curves of different

specimens of bearings of the tumble sleeve: Two of the curves are derived from the same standardized type of bearing, but from two different manufactures. The difference between these two curves is quite noteworthy. The global or local standards, such as i.e. DIN 625 for deep-groove ball bearings, more or less only specify the outer dimensions of a bearing. Parameters like the exact curvature of the raceways or even the diameter of the steel balls is left to the manufacturers. This can create quite some difference in the load-displacement curves, as can be seen here. The third curve in Figure 5.6 belongs to a bearing with increased clearance. Again, the difference is quite noticeable.

It has been known since the 1950s that the compliance of rolling element bearings will vary during operation, depending on the number of rolling elements under load [131]. This means that, due to the limited number of rolling elements, even bearings under constant load will parametrically generate vibrations, no matter how perfectly they are manufactured. This parametric excitation plays an important role in the field of acoustics and machine diagnosis [132]. In the current case, however, the parametric excitation due to the bearings lies in a frequency range that is more than a dimension higher than the frequency range of interest. In addition, the difference in compliance resulting from different load angles is small enough to be neglected for the current problem. Therefore, the dependency of the load-displacement curves on the load angle is ignored, and the curves are calculated from the load case, as indicated in Figure 5.5.

Attentive readers will notice that the load-displacement curves show no jump-behavior at the zero crossing, as should be expected since the bearings contain internal clearance. In a real-world bearing, the reaction force to a load might be very small, but will never be zero. This is due to friction between the steel balls and the cage or due to friction at the sealings, thereby smoothing out the jump at the zero crossing. At the same time, the discontinuity at the zero crossing in form of a jump is numerically quite problematic and significantly slows down the simulation. Therefore, in the current work, the inner and outer bearing ring are connected with a very soft spring in order to prevent the jump behavior in the load-displacement curves. For the physical behavior of the bearings, the additional stiffness of the artificial spring is neglectable, and the load-stiffness curves still correctly describe the nonlinear load-displacement curves. The only reason to introduce the additional spring-stiffness is to prevent numerical difficulties in a model that is already challenging in the sense of computational effort.

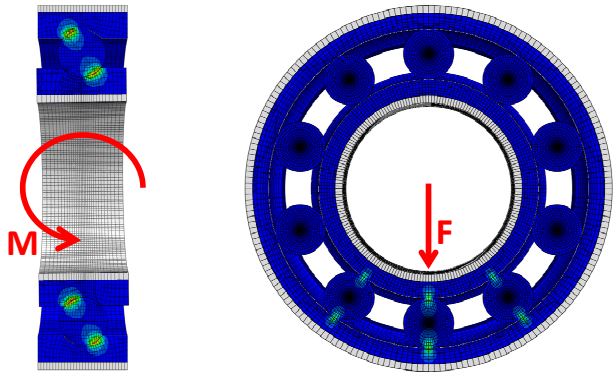

Figure 5.5: FEM sub-model to calculate the load-displacement curves of the bearings

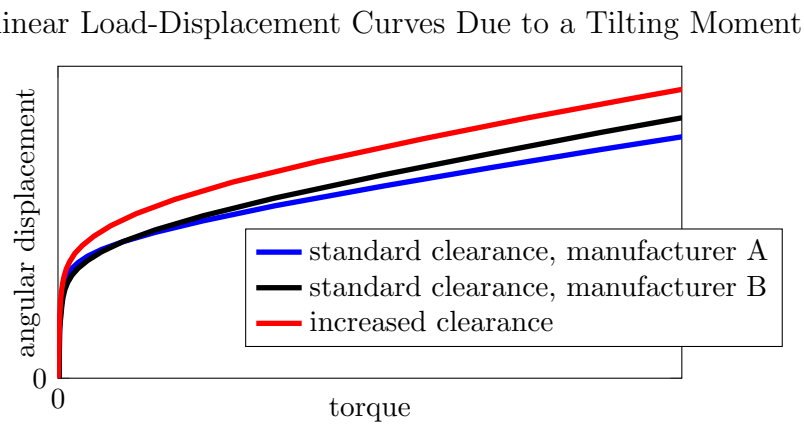

Figure 5.6: Nonlinear load-displacement curves of different bearings

5.2.2.3 Estimating the Damping

The damping of the bearings is an important parameter for the dynamic behavior of a rotor system, as indicated in Chapter 2. In the case of rolling element bearings, damping usually has a stabilizing effect [37], while in the case of lubricated journal bearings, damping can have a destabilizing effect in the overcritical speed range known as “oil whirl and whip” [35]. The danger of this latter phenomenon is most likely the reason why the damping of journal bearings is researched quite well and explains the existence of numerous works on theoretical damping models. A review can be found in [24], which is about tilting pad bearing theories in general, but also contains stability considerations of journal bearings with fixed geometry. In comparison, hardly any theoretical models on the damping of rolling element bearings exist. Most of the available research focuses on experimentally identifying the damping values. A summary and review of relevant works is presented by *Tiwari*, *Lees* and *Friswell* in [137].

Some authors, i.e. [37, 76], consider the damping of roller element bearings to be rather small in general. However, experimental research on the topic by *Walford* and *Stone* showed a much higher damping of the bearings than expected [146, 147]. The authors concluded, and later confirmed in [148], that the damping occurring due to the interaction of the bearing rings with the housing and the shaft is significantly larger than the damping in the bearing itself. They also found out, that the damping due to the tilting movement is larger than that of the radial movement. This might be an important thing to consider with regard to the working example of this thesis: The focus of the research is a bending resonance, which might cause significant tilting movement in the bearings.

Since no suitable theoretical model seems to exist, viscous damping is assumed for the translational and for the tilting movement of the bearings. The damping coefficients are determined experimentally by performing FRF measurements at the core bit tip when the system is at rest, as will be described in Chapter 6.2.2. Before doing so, the drive shaft assembly is updated with the results of EMA in free-free conditions. This so called *in situ* approach offers the advantage of taking into account the damping that occurs due to the interaction of the bearing races with the housing and the shaft, as described above. However, according to *Kraus et al.*, the damping of roller element bearings depends strongly on the rotational speed and decreases with higher speed [77]. Therefore, the bearing damping in the current thesis is probably overestimated, since it is evaluated at standstill condition. Furthermore, a possible dependency of the damping from the load condition of the bearing is ignored. Or more precisely, the damping is evaluated at "no load". In the bending resonance, the load on the bearings will be significantly higher. According to the experimental results of [148] and [77], the damping of a rolling element bearing decreases with an increasing preload. Thus, ignoring the load-dependent damping characteristic might also lead to overestimating the damping.

Until now, the damping behavior has been discussed only for the translational and the tilting movement. With regard to instationary rotational speed and with regard to the torsional behavior of the rotor system, the damping and friction of the bearings in the spinning direction is of importance. A review of relevant methods on how to calculate the drag torque of rolling element bearings is presented, amongst others, by *Fritz* [34]. According to that, the widely used approaches by manufactures like *INA/FAG* or *SKF* are based on the work of *Palmgren*, published in 1957 in [106]. Based on experimental data, *Palmgren* developed a rather simple-to-use formula that phenomenologically describes the drag torque. The main finding is, that the overall torque can be described as a combination of a part that is purely

dependent on rotational speed, and another part that is purely load-dependent. This is due to the fact that the effects of friction in the rather complicated interaction within a rolling element bearing can range from pure *Coulomb friction* [21] to hydrodynamic friction, as expressed by *Stribeck* [59]. Recent approaches by bearing manufactures are more refined and set up different mathematical terms for moments resulting from rolling and from sliding of the rolling elements, as well as moments resulting from friction due to contacting seals and from flow losses in the lubrication medium. Even in these more refined approaches, it is possible to distinguish between moments that depend purely on the rotational speed and moments that are speed-independent, since they depend on the bearing load. The problem with these recent approaches is the fact that they are still partly phenomenological and use bearing type specific coefficients that are derived by experiments or by experience. For most standard bearings, these coefficients are available in the catalogs published by the manufactures, such as, for example, in [32, 125]. Unfortunately, the diamond coring system regarded in this thesis is not equipped with standard bearings, which makes it difficult to apply the abovementioned formulas. Having the necessary coefficients measured by a third party is out of the scope of this thesis. However, instead of estimating the necessary coefficients, a different approach is adopted. The idea is to derive the overall drag torque T_d from a run-down of the system. Once the drag torque is known, it is approximated by a combination of a speed-dependent term T_Ω and a load-dependent term T_C, as described above:

$$T_d = T_\Omega + T_C \tag{5.6}$$

Since it is hardly possible to do the run down with different loads, the load-dependent term T_C is replaced by a constant frictional torque (which is independent of the rotational speed):

$$T_C = c \ , \qquad \text{with} \quad c = \text{const.} \tag{5.7}$$

For the sake of simplicity, T_d is assumed to be linear in the rotational speed:

$$T_\Omega = b \cdot \Omega \ , \qquad \text{with} \quad b = \text{const.} \tag{5.8}$$

The overall drag torque in the machine is not only caused by the friction of the bearings, but also by losses in the driving belts and by friction in the water swivel. The influence of the later is assessed by simply repeating the run-down without a swivel mounted. Evaluating the losses of the driving belts, however, is not so straightforward. To keep the effort reasonable, the losses in the belts are charged on the bearings. Once the drag torque resulting from the

bearings is known, and therefore the constants b and c in Equations 5.7 and 5.8, constant c is distributed evenly on the eight rolling element bearings (two each for the electric drive, the shaft, the tumble sleeve and finally the toothed belt disk that drives the shaft). Constant b is distributed on the eight bearings according to their speed ratio. The implementation of this approach follows in Chapter 7.2.2.

5.2.3 Force-Locked Chuck

Chapter 3.2.3 illustrated the mechanical setup of the force-locked chuck. The current section deals with the way the chuck is represented in the simulation model. Three things need to be considered here:

- The thread that connects the inner piece of the chuck to the shaft.
- The contact between the connecting end of the core bit and the two-piece chuck.
- The clamping spring in the force-locked chuck.

5.2.3.1 Connection Between Chuck and Shaft

The inner piece of the chuck is connected to the shaft with a screw thread. The representation of a bolted connection in an FE-model can range from modeling every single detail of the thread and the contact situation, requiring hundreds of thousands of DOFs, to simply tying the two pieces together at the contact zone. With regard to computational costs, the latter method is clearly in favor. If a tie constraint is to be used on the contact zone, the question that needs to be answered is how much of this area needs to be included in the constraint. This depends on the ratio between pre-tension due to the bold load, compared to stress inflicted by external loads acting on the rotor systems during operation. At areas of the contact zone, which stay pre-stressed at all times, the nonlinear contact behavior can be ignored and a tie constraint can be seen as a justified simplification. At areas where the two objects diverge due to bending deformation at the rim of the circular contact zone, a tie constraint would mean a stiffer joint in the model than in the physical object. When representing bolted connections with tie constraints, in industrial practice, usually the area of the contact zone is tied, that lies within the pressure cone of the bolts. The diameter of these pressure cones can be calculated by the following analytical formula (ignoring macroscopic

relative movement) [152]:

$$d_{res} = d_w + \frac{l_k}{a} \qquad \text{and} \qquad A_{res} = \frac{\pi}{4} \cdot \left[\left(d_w + \frac{l_k}{a} \right)^2 - {d_h}^2 \right] \tag{5.9}$$

in which the variables have the following meaning:

- d_{res} substitutive diameter of the pressure cone (area to enforce tie constraint upon),
- d_w head contact diameter of the bolt,
- l_k clamped depth of the two parts,
- a material specific constant,
- d_h diameter of through hole,
- A_{res} substitutive area of the pressure cone (area to enforce tie constraint upon).

In the current case, the contact zone between the shaft and the inner piece of the chuck is rather small. As can be expected, Equation 5.9 comes to the conclusion that the diameter of the contact zone is actually smaller than the substitutive diameter of a pressure cone, as it would manifest in a wide-spread area of support. Therefore, modeling the connection between shaft and chuck using tie constraints might be justified. However, Equation 5.9 assumes a bolting connection with standard machine elements. The current geometry, though, is different: The shaft is hollow to allow water to flush through, and the tightening torque prescribed by the manufacturer is different from a standard thread of this diameter. To be on the safe side, the connection between shaft and chuck was first modeled using contact and taking into account the pre-tension of the screw-thread. Once it became clear that the two parts do not diverge during operation, the model approach was simplified to just tying the two parts together.

The more refined modeling approach uses contacts, couplings (distributed constraints) and the connector function to represent the connection between shaft and chuck in ABAQUS. Figure 5.7 shows a schematic diagram of the approach. The geometry of the thread itself is not explicitly modeled. Instead, both parts have a circular cross-shape with the nominal diameter of the thread in the relevant region. Now, surfaces are defined on both the chuck and the shaft to represent the thread, as well as for the contact zone. For the latter, contact is enabled but not for the two surfaces belonging to the thread. A detailed description of the contact formulations follows in the next chapter and is not elaborated here. Finally, couplings and the connector function represent the “clamping” mechanism of the screw thread. The

procedure is the same as for the ball bearings in Chapter 5.2.2: For each surface, the coupling function links the DOFs of the surface nodes to a single master-node. A connector element then links the two master-nodes, allowing one to apply a clamping force in the axial direction of the thread. The following analytical formula approximates the amount of the clamping force F_{VM} according to the tightening torque T_A [152]:

$$F_{VM} = \frac{T_A}{\frac{d_2}{2} \cdot \tan(\alpha + \sigma') + \mu_k \cdot \frac{d_k}{2}} \tag{5.10}$$

in which the other variables have the following meaning:

- d_2 thread pitch diameter,
- α thread pitch angle,
- σ' thread angle of friction (depending on surface conditions and lubrification),
- μ_k coefficient of friction of the support area,
- d_k effective diameter of friction in the screw head pad.

The simplified modeling approach does not use the contact, coupling and connector, but merely ties the two surfaces used for the contact.

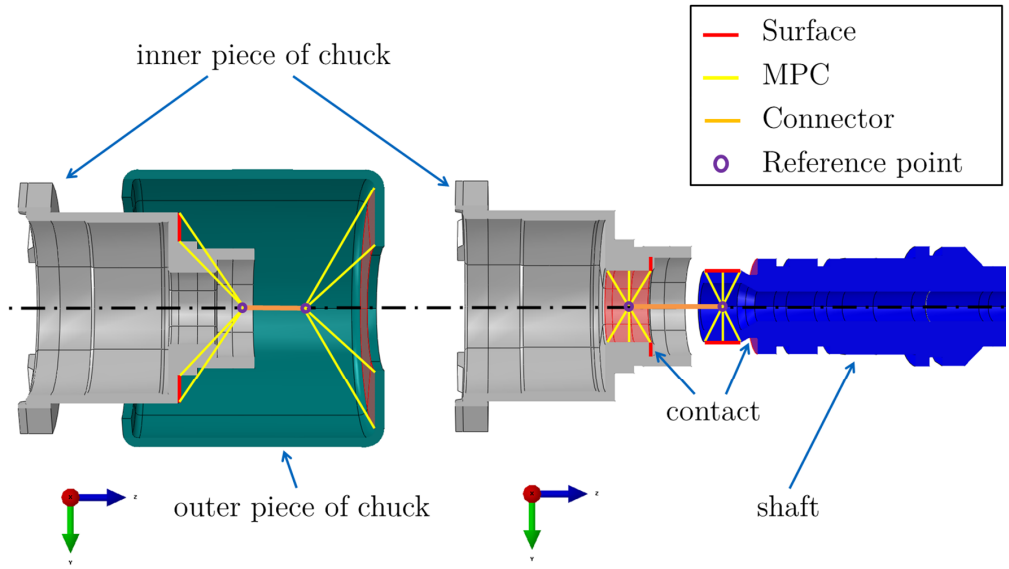

Figure 5.7: Schematic diagram of the interfaces between chuck and shaft

5.2.3.2 Contact Between Core Bit and Chuck

Figure 5.8 contains a sectional view of the region around the chuck. For the interaction between the connecting end of the core bit and the two-piece chuck, contacts are defined at the relevant areas of the different components, as indicated in Figure 5.8, and in a more detailed way in Figure 5.9.

Contacts are defined between

- the outer piece of the chuck and the connecting pins of the core bit,
- the connecting pins of the core bit and the sockets of the inner piece of the chuck,
- and between the outer diameter of the connecting end of the core bit and the bore of the inner piece of the chuck. (In undeformed configuration there is radial clearance between these two contact partners).

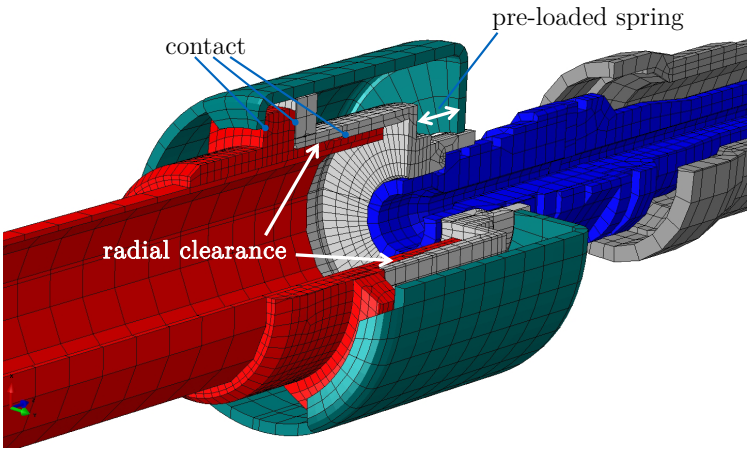

Figure 5.8: Sectional view of the FE-model of the force-locked chuck

Selecting the surfaces that are involved in a contact formulation is a crucial task with regard to the performance of a model. Enforcing contacts and constraints causes significant computational effort. ABAQUS automatically creates internal nodes for the necessary calculations. Depending on the problem, the number of these internally generated nodes can easily exceed the number of nodes defined by the user, thereby boosting the total number of variables in the simulation and thus the computational costs to solve it. From a performance point of view, the contact surfaces should be as small as possible. However, in the example at hand, one must bear in mind that if the clamping force in the chuck is exceeded, the contact partners will undergo large relative motion during a dynamic analysis. Therefore, it is necessary to define the contact surfaces larger than the actual areas of the parts that

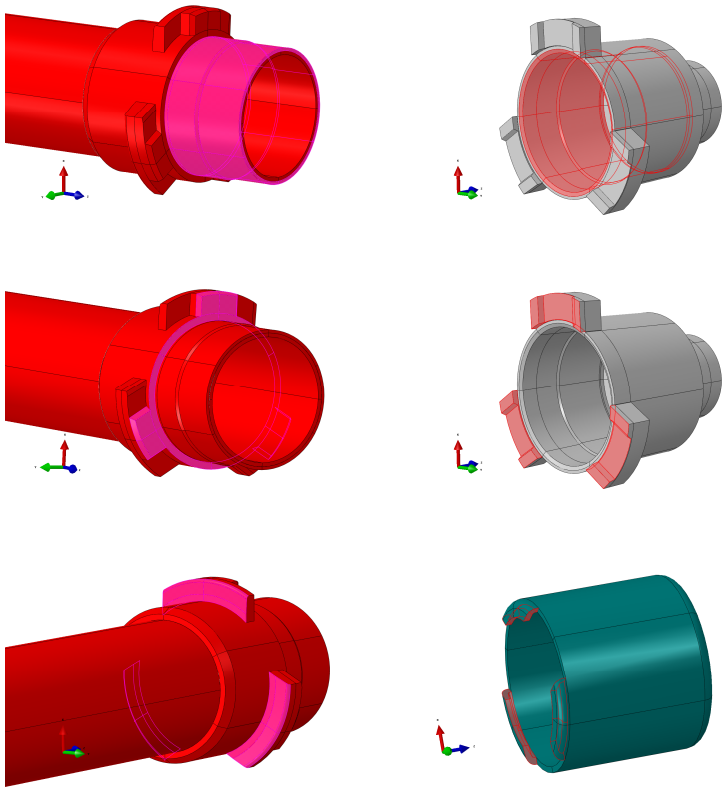

Figure 5.9: Corresponding contact surfaces in the force-locked chuck

touch each other in undeformed configuration. Any surfaces that could come into contact during a possible relative motion need to be included in the contact formulations. Otherwise, the contact situation might be wrongly represented in the model, causing the contact partners to penetrate each other without resistance. Another typical error that might occur when specifying the contact surfaces too small, is that nodes of one of the surfaces "hang" over the rim of the other surface, causing no or only slow convergence. In the current case, the surfaces engaged in contact formulation are selected as small as possible but as large as necessary.

ABAQUS offers a wide range of contact formulations, which provides different choices for

- the way of contact discretization,
- the contact tracking approach,
- and the assignment of master and slave roles to the contact surfaces.

The simulation model of the example at hand uses

- solely surface-to-surface contact discretization,
- finite sliding as a tracking approach,
- and an assignment of master-slave contact pairs as shown in Figure 5.9.

Another important issue to consider when dealing with contacts in FE-simulations is the method that enforces the contact constraints. Here, for both normal and tangential behavior, a penalty method is selected. In the normal direction, the pressure-overclosure relationship is regarded as a "hard" contact, enforced by a linear penalty method. The tangential behavior contains friction in which the friction coefficient is taken from [152] according to the combination of materials. In addition to the friction, a small amount of damping is added to the contact behavior. It is only a small value to represent a physical damping effect. The presence of damping significantly increases the convergence.

5.2.3.3 Clamping Mechanism

As described in Chapter 3.2.3, a set of disk springs ensures the clamping force that holds the core bit in the chuck. In the simulation model, the clamping mechanism is represented with basically the same methods as the ball bearings from Chapter 5.2.2.1. Figure 5.7 offers a schematic diagram. A connector element stands for the set of disk springs that are not explicitly modeled as a 3D solid object. In reality, a spanner flat at the rear end of the chuck with a clearance fit between the inner and the outer piece allows axial movement, but constrains translational movement perpendicular to the spinning axis of the drive shaft, as well as torsional movement. Therefore, in the model, the connector has a DOF in the axial direction of the drive shaft and in the 2 rotational DOFs perpendicular to the spinning axis. All other DOFs, however, are constrained. The mass of the disk spring is considered as a point mass with moments of inertia and is placed at one of the reference points of the connector. Distributed couplings link the reference points of the connector with the inner and with the outer piece of the chuck. The pre-load of the spring is measured in a compression-tension machine according to Figure 5.10. In the model, the load-displacement curve is idealized to represent an elastic spring connected to perfectly rigid adjacent bodies. As can be seen, the ratio between displacement and the reaction force will change significantly once the pre-load is exceeded, creating strong nonlinear behavior. This characteristic of the force-locked chuck and the consequences for the overall dynamics will be discussed in-depth in Chapter 7.4.1.

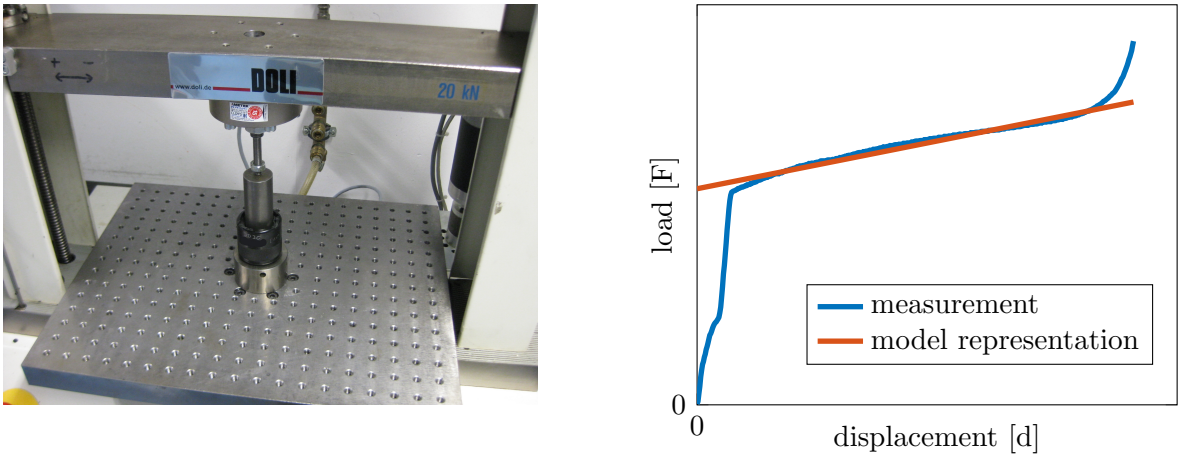

(a) measurement setup

(b) load-displacement curves

Figure 5.10: Measured and idealized load-displacement curve of the force-locked chuck

5.2.4 Power Train

The power train contains components that need to be addressed in the model because of their elastic behavior, as well as components that are important because of their mass and inertia properties.

The **two toothed belts** elastically interconnect the three rotors of the system. This interconnection contains a torsional as well as a translational component. The tensile stiffness of the belts is measured externally by the manufacturer in a static procedure according to the setup in Figure 5.11. Apart from a slightly nonlinear behavior at low forces, the belts show an almost perfectly linear stiffness behavior up to the breaking point. Since the belts are pretensioned in the machine, the small nonlinearity is ignored and the belts are represented as linear springs in the model. The connector function allows one to consider the pretension of the belts.

Despite – or, more precisely, because – the purpose of the model is to study a bending resonance during run-up, the torsional behavior of the system is just as important as the bending. In rotor dynamics, there are several effects that couple the torsional and lateral movement of a rotor: Large bending vibrations might excite torsional vibrations [100], while, the other way around, a fluctuating drive torque could lead to lateral instability [90]. In the current simulation model, in addition to a model representation as lateral springs, the belts are represented as elastic torsion springs, using the connector functionality of ABAQUS. The torsional stiffness is calculated from the tensile stiffness of the belts, which is measured as described above.

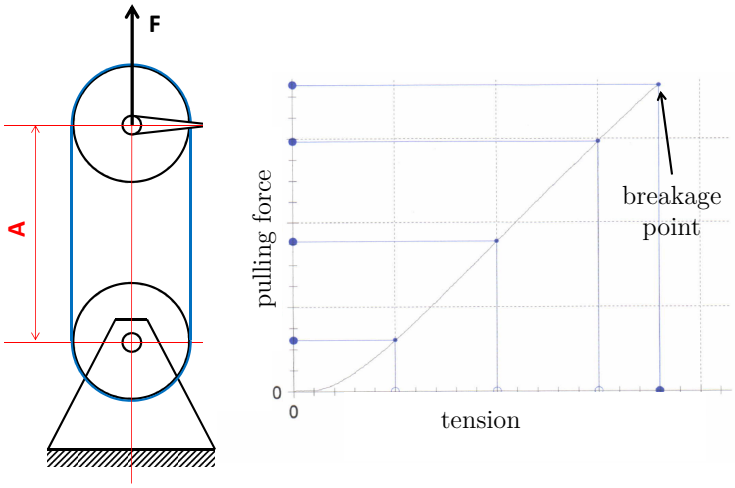

Figure 5.11: Setup to measure the stiffness of the belts

The **rubber joint** that compensates the tumbling movement while transferring the torque to the drive shaft is represented in the model as an elastic spring-damper system for both the lateral and the torsional direction. The stiffness and damping values are measured in a static substitute test.

The **slip clutch** and the **two toothed belt disks** show no local modes in the frequency range of interest and can be considered rigid bodies. In contrast to the components forming the drive shaft and the tumble sleeve, the slip clutch and the belt disks are not represented in the model using 3D solid modeling. Instead, they are taken into account by introducing point masses with inertia properties. MPCs interconnect these point masses to their corresponding mounting positions. The MPCs are applied at the surface of the corresponding bearing seats of the slip clutch and the belt disks, thereby taking into account the stiffening effect resulting from the press fit between shaft and bearing ring. The stiffness of the ball bearings themselves is ignored in this case, as it is more than a dimensions higher than the bending stiffness of the drive shaft or of the tumble sleeve.

The **electric engine** has to be considered in a double manner. First, with regard to its mechanical stiffness and mass parameters, and, second, with regard to the torsional stiffness of the magnetic field between rotor and stator. The latter might become important in a transient run-up or run-down when the vibration amplitudes grow large while crossing the bending resonance. With regard to the mechanical properties of the drive, one has to be aware that the electric engine is designed so that it is operated subcritically, meaning well below its first bending resonance. Therefore and to save simulation effort, it is represented in the simulation model as a point mass with inertia properties.

When directing one's attention towards modeling the torsional behavior of an electric engine, one can distinguish between three levels of model refinement:

1. On the simplest level, energy is transferred to the drive by applying kinematic boundary conditions to the rotor of the electric engine.
2. In a more advanced model approach, a drive torque acts on the rotor, which is, however, not influenced by the response of the mechanic system.
3. On level three, the electric engine is part of the mechanical model, taking into account the response of the system to the drive torque.

As described in Chapter 4.2.1, in the experiment, the supply voltage of the electric engine is ramped-up linearly, resulting in an almost linear run-up slope of the rotational speed of the rotor system. Accordingly, the most convenient and intuitive way to realize the run-up in the simulation would be to choose model level one, which means applying a corresponding displacement, or more precisely, a velocity boundary condition, to the electric drive. This very simplified modeling approach, however, strongly influences the dynamic behavior of the simulation model, as it causes two effects: First, it treats the stiffness of the magnetic field between rotor and stator as rigid, causing the dynamic system to lose one degree of freedom, which might be important, as large bending resonances also mean a torsional excitation of a rotor system, as described above. Second, in terms of energy balance, modeling the drive as a simple velocity boundary condition means supplying an energy source of unlimited power. Doing so could result in severely disturbing the energy balance, creating higher bending amplitudes in the model than in the real-world system.

A model approach from level two could be realized by recording the current consumption during the experiments and calculating the torque of the electric engine from it. Therefore, the magnetic constant k_m must be known [129]. Unfortunately, the electric engine of the machine acting as a working example does not operate on its natural characteristic, but is software controlled, thereby preventing a simple calculation of the effective moment. For safety reasons, the controller could not be deactivated completely for the current research. One option would be to chose a model approach from level three, which means to include the electric engine and the controller in the model. Theoretically, this is possible in ABAQUS, using customized user subroutines [23]. Practically, however, the effort of such an approach is out of the scope of this thesis.

The good thing about the controller being active is the fact that in normal operating conditions, as described in Chapters 7.1 and 7.3, the rotational velocity is almost perfectly

proportional to the supply voltage. In this case, there is nothing wrong with simply applying a velocity boundary condition to the electric engine in the model (level one). Only when the bending amplitudes grow large very suddenly is the power of the electric engine insufficient to keep up the linear ramp-up of the rotational velocity. This happens if the clamping force is exceeded, as shown in Chapter 7.4, accompanied by a *Sommerfeld-Effect*, as described above. In this case, a velocity boundary condition would partly prevent the occurrence of the effect in the model. Therefore, the model approach for applying the drive torque is chosen so that the velocity boundary condition is not applied directly on the rotor of the electric engine, but rather to the open side of a torsional spring, which, in turn, is attached to the rotor. This way, the model is still capable of representing the relevant dynamic effects, such as the mode-locking in Chapter 7.4.3, without the need of an expensive model approach from level three.

5.2.5 Mechanical Sealing

Due to the mechanical sealing described in Chapter 3.2.1, the shaft is in permanent contact with a non-rotating part fixed to the housing of the machine. In rotordynamics, any rotor-to-stator contact should be eyed very carefully. The effects can range anywhere from negligible to malfunction all the way to catastrophic failure due to self-excited vibrations. Thorough information on the topic can be found, amongst others, in [7, 8, 15, 16, 29, 95, 97, 124, 153].

In the current case, the friction of the mechanical sealing as well as the overall stiffness is smaller by dimensions than the bending stiffness of the shaft. Furthermore, the sealing is positioned directly next to a bearing. In this case, no significant influence of the sealing can be expected. Experiments with and without the presence of the mechanical sealing revealed no significant influence, neither on the vibrational amplitudes, nor on the drag torque represented in the time for coasting-down. Therefore, the mechanical sealing is simply ignored in the simulation model. It should be mentioned, though, that if the seal showed a significant influence, the chosen modeling approach would be well suited to deal with the effect. The seal could be represented in a pragmatic way as a connector element containing a (nonlinear) friction load to speed relationship. In the most refined model approach, the seal could be represented including contact formulations for the two rings. This would, however, be very costly in the sense of computational effort.

5.2.6 Human Hand-Arm System (Operator)

Since most measurements are performed while the power tool is hand-held, the simulation model must be able to adequately represent the influence of the human operator on the dynamic system behavior; a task that primarily requires one to somehow model the bio-dynamic characteristics of the human hand–arm system. In the literature, a vast amount of research is available that deals with hand–arm vibrations. An overview of models for applications to hand-held power tools can be found in [112] and more recently in [2]. To characterize the dynamic response and energy absorption of the human hand-arm system, these modeling approaches consist of lumped-parameter models or of continuous models based on beam theory. Lumped parameter models even found their way into industrial standards, as in ISO 10068 [58] and DIN 45677 [25]. Even today, research is still ongoing to experimentally derive stiffness, mass and damping parameters in order to improve these models [68–70, 75, 150]. More recent approaches regard the human hand-arm system as a non-uniform, nonlinear, anisotropic and composite system that requires FE modeling for reliable identification of the resonant frequencies and mode shapes [3].

Although a large number of different model approaches and research exists, the usefulness of the models mentioned previously for the simulation task of the underlying thesis is rather limited. The primary purpose of the models described above is not to provide boundary conditions in dynamic analyses of hand-held tools, but rather to study the injurious effects of hand-transmitted vibrations, causing vascular, sensorineural and musculoskeletal disorders, known as *Raynaud's phenomena* or more generally as *hand-arm vibration syndrome* [10, 135]. Openly available models with reasonable effort of implementation provide only translational DOFs, neglecting the rotational stiffness and moments of inertia of the hand-arm system. Most electric power tools designed for drilling operations are equipped with a main handle positioned in the symmetry plane and a side-handle positioned outside of the symmetry plane to compensate the drilling torque. Neglecting the rotational stiffness of the operator's hands, the model can never correctly describe the reaction of the tool to excitation forces resulting from the drilling process, or simply from rotational forces during a free run-up, which is the main focus of interest of this thesis. Furthermore, any passive mechanical model neglects the human control behavior, which consists of changing the stiffness characteristics of the hand-arm system as well as applying forces to correct or hold the position of the power tool. For instance, when applying Model 1 of ISO 10068 to the test setup described in Chapter 4.2.1 and in Figure 4.5, the tool would hang down in a skewed 30 degree angle due to gravity, while an operator of average constitution is able to easily hold the tool horizontally by applying

correctional forces.

In general, the challenge in modeling the hand-arm system consists of adequately representing the stiffness, mass and damping effect over a wide frequency range, as the mechanical impedance of the human hand-arm system strongly depends on the frequency. The main task of the model developed in this thesis is to correctly describe the dynamic system behavior when crossing a bending resonance during run-up or run-down. As a consequence, the frequency range of interest is rather limited. In this case, the hand-arm system can be modeled as a simple spring-damper system with added mass, in which the parameters are accordingly tuned. However, one must be aware that the model will yield accurate results only in the frequency range of interest and that the error, especially at very low frequencies, can be significant. Since the latter is acceptable in the current case, the hand-arm system is represented as a spring damper-system in this thesis. Modal measurements, as described in Chapter 4.2.2, are performed at non-rotating condition to identify the stiffness, mass and damping parameters. In theory, the approach would allow one to identify the relevant parameters in all 6 DOFs for each of the two hands. In total, this would add up to 36 unknown parameters that need to be identified. However, since the underlying mechanical system is mechanically rather complicated and therefore the model already contains quite some assumptions and uncertainties, the quality of the results can be doubted. Therefore, instead of identifying the parameters for each hand separately, the added mass of the hand-arm system is simply surcharged to the mass and inertia parameters of the machine, while the stiffness and damping parameters of the two hands are combined to a single spring-damper system which acts on the center of gravity of the rotor system.

6 Model-Updating in Non-Rotating Condition Using Modal Analysis

As mentioned at the beginning of the previous section, model development starts with the definition of the *focus of interest*, followed by the creation of a conceptual model. The next steps consists of the *parameter identification* of the necessary model parameters and *implementation* of the computer model. Before the model can be used to predict the dynamic behavior of the rotor system, *verification* and *validation* is needed. Although there seems to be no common understanding of the terminology in the area of verification and validation [74], a number of authors, i.e. [104, 117, 136], adopt the definitions used in an AIAA Guide from 1998 [4]:

- Verification is the process of determining that a model implementation accurately represents the developer's conceptual description of the model and the solution to the model.
- Validation is the process of determining the degree to which a model is an accurate representation of the real world from the perspective of the intended use of the model.

When it comes to *verification* of the computer model, according to [104], two different types of actions should be recognized: *Code verification* focuses on how correctly the numerical algorithms are implemented in the code, while the primary goal of *solution verification* is to estimate the numerical accuracy of a given solution, involving, amongst others, studies of the spatial or temporal convergence rate. Once the simulation model is verified, it still needs *validation*, which means an assessment of the accuracy of the simulation by comparing the outcomes to experimental data. The following sections describe the verification and validation strategy of the current work.

In the underlying application example, the focus of interest is on the dynamic behavior of the rotor system when crossing a bending resonance during run-up or run-down. The model approach described in Chapter 5 is that of an elastic multi-body simulation in which the rotating parts are represented as elastic 3D solid models. They are interconnected either by spring-damper systems with non-linear stiffness characteristics, as in the case of the bearings, or by contact definitions, as in the case of the force-locked chuck. The non-rotating parts, like the machine housing as well as the sensor rig, are considered rigid bodies that are represented as lumped masses.

Implementing this computer model requires the identification of a large number of parame-

ters. For example, the decision to represent the driving-belts of the shaft and of the tumble sleeve as elastic lateral and torsional springs requires one to identify the stiffness of these springs. This is done in a substitute experiment as described in Chapter 5.2.4. To give another example: Modeling the rotating parts as elastic bodies requires information regarding the geometric and material properties. While the latter is from the literature, the former makes use of the CAD model. The fact that the geometry can be taken directly from existing CAD-data is one of the major advantages of the current model approach over using beam-element models.

Once the model parameters are identified and the model is implemented, it needs to be verified and validated. As described above, verification consists of code and solution verification. In the underlying thesis, ABAQUS is used to implement the simulation model. The current model solely uses available standard finite elements formulations and program functions, such as MPCs, contact definitions, or the connector function, which have been intensively verified and documented in [23]. Therefore, no further activities are triggered to verify the code. With regard to solution verification and validation of the model, one must be aware, that the model is quite complex and contains a large number of parameters and components. Validating the model could, for example, mean comparing the outcomes of the simulation to experimental data acquired during a run-up, as described in Chapter 4.2.1. Due to the size and complexity of the model, it will most certainly be difficult to trace back a possible deviation between simulation and experiment on the responsible subcomponent of the model. In addition, even if the simulation model matched the experimental results upon the first try, the possibility cannot be ruled out that the model contains more than one error, which by chance compensate each other. In that case, the model might be able to correctly describe the given experiment, but still it is not able to correctly predict any changes to the rotor system. Thus, a model of the given complexity should be verified and validated from the bottom up, meaning to start with single components instead of the whole simulation model at once.

A powerful tool to verify and validate the model is to perform modal analysis. The following sections describe how modal analysis is performed first on single components and thereafter on the whole system. The goal is to verify, validate and update the model in non-rotating condition, as well as to identify certain parameters, such as the damping of the bearings and the dynamic parameters of the human operator. Since not all missing parameters can be identified in non-rotating condition, Chapter 7.2 deals with the procedure to identify the overall drag torque and the imbalance of the core bit from operational measurements.

6.1 Single Components

In what follows, the steps to verify, validate and update the model representation of the diamond core bit will be described as an example of the rotating components modeled as elastic bodies.

On the one hand, the diamond core bit appears to be a rather simple structure in the sense of structural dynamics, consisting mainly of a hollow tube. On the other hand, the geometry at the connecting end towards the chuck is rather complex, and the whole component is made out of four different materials. The very tip is made out of a sinter metal, containing the industrial diamonds as cutting material, the actual tube is made out of steel, and the connecting end consist of aluminum which is mounted around the steel tube in a casting process. For a 3D solid modeling approach, none of the before mentioned things is imposing a real challenge. The core bit is decomposed into different sections and the corresponding material parameters are applied. At the boundaries between the different sections, tie constraints are introduced, while at the same time the mesh is setup such, that the nodes are congruent within the joint patches as far as possible.

6.1.1 Mesh-Grid Convergence Study

To verify the numerical solution, a mesh-grid convergence study is performed using the natural frequencies of the first ten modes in free boundary conditions as a criterion to evaluate the error. The study starts with a very coarse mesh, which is refined in subsequent steps until the numerical solution converges. Important parameters for the mesh refinement are the element size and the number of elements per corner arc. Since the lower modes are completely dominated by the tube-like part of the core bit and since the connecting end needs a much finer mesh anyway due to the contact formulations with the chuck, the mesh is changed only on the tube. Table 6.1 contains an overview of the results, while Figure 6.1 shows different levels of mesh refinement as well as pictures of typical mode shapes.

The first ten modes contain four different types of modes: Bending modes, ovalization modes, which are typical for a hollow structure, and finally a torsional and even a longitudinal mode. Both the bending and the ovalization modes appear as double modes due to the (cyclic) symmetry of the structure. The largest influence of refining the mesh shows itself in the ovalization modes, while other mode types are less affected. After the fifth iteration, there are no more recognizable changes in the natural frequencies and the solution has converged.

Table 6.1: Model-updating of the core bit

			mode shape and natural frequencies									
			1st bending	1st ovalization	2nd ovalization	**2nd bending**	3rd ovalization	1st torsion	4th ovalization	5th ovalization	**3rd bending**	1st longitudinal
	measurement											
	natural frequency	[Hz]	**408**	960	1054	**1115**	1260	1293	1454	1767	**2065**	2145
	damping ξ_i	%	**0.08**	0.1	0.08	**0.08**	0.05	-	0.05	0.06	**0.07**	-
	simulations											
1	element size n. elements p. corner arc: 2	[Hz]	**414**	1026	1120	**1128**	1323	1300	1509	1842	**2086**	2157
	rel. error	%	**1.4**	6.9	6.3	**1.1**	5.0	0.5	3.8	4.3	**1.0**	0.6
2	element size n/2. elements p. corner arc: 3	[Hz]	**414**	1006	1099	**1128**	1298	1301	1482	1811	**2087**	2158
	rel. error	%	**1.4**	4.8	4.3	**1.2**	3.0	0.6	2.0	2.5	**1.1**	0.6
	changes to prior solution	%	**0.1**	-2.0	-1.9	**0.1**	-1.9	0.1	-1.8	-1.7	**0.1**	0.0
3	element size n/4. elements p. corner arc: 4	[Hz]	**414**	1002	1095	**1128**	1292	1301	1475	1802	**2087**	2158
	rel. error in	%	**1.4**	4.4	3.9	**1.2**	2.5	0.6	1.5	2.0	**1.1**	0.6
	changes to prior solution	%	**0.0**	-0.4	-0.4	**0.0**	-0.5	0.0	-0.5	-0.5	**0.0**	0.0
4	element size n/8. elements p. corner arc: 8	[Hz]	**414**	999	1091	**1128**	1288	1301	1470	1795	**2086**	2157
	rel. error in	%	**1.4**	4.1	3.5	**1.2**	2.2	0.6	1.2	1.6	**1.0**	0.6
	changes to prior solution	%	**0.0**	-0.3	-0.3	**0.0**	-0.3	0.0	-0.3	-0.4	**0.0**	0.0
5	element size n/16. elements p. corner arc: 12	[Hz]	**414**	999	1091	**1128**	1287	1301	1470	1795	**2086**	2157
	rel. error	%	**1.4**	4.1	3.5	**1.2**	2.2	0.6	1.1	1.6	**1.0**	0.6
	changes to prior solution	%	**0.0**	0.0	0.0	**0.0**	0.0	0.0	0.0	0.0	**0.0**	0.0
6	same as #3. updated outer diameter	[Hz]	**413**	966	1061	**1127**	1261	1295	1444	1778	**2086**	2149
	rel. error	%	**1.2**	0.6	0.7	**1.1**	0.1	0.2	-0.7	0.7	**1.0**	0.2
7	same as #6. E-module reduced by 1.4 %	[Hz]	**410**	959	1054	**1119**	1252	1286	1434	1766	**2071**	2133
	rel. error	%	**0.5**	-0.1	0.0	**0.4**	-0.6	-0.6	-1.3	0.0	**0.3**	-0.5

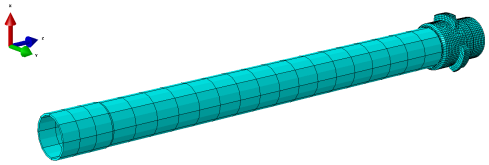

(a) simulation #1

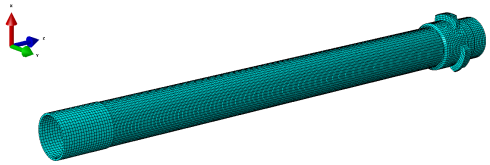

(b) simulation #5

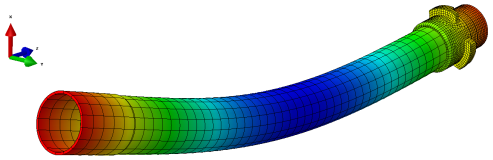

(c) 1st bending mode

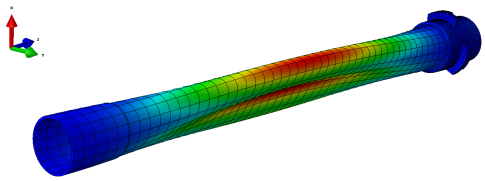

(d) 1st ovalization mode

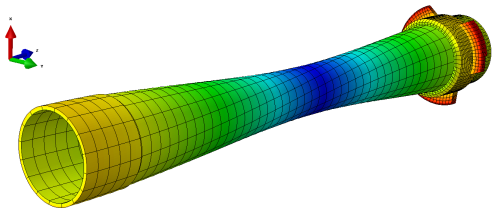

(e) 1st torsional mode

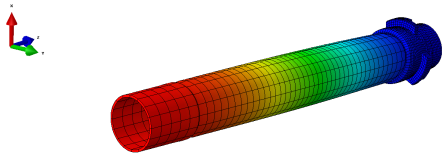

(f) 1st longitudinal mode

Figure 6.1: Varying mesh grid and mode types of the core bit

In the further course of this thesis, model #3 is used to simulate the run-up of the rotor system.

The next section will discuss validating and updating the simulation model.

6.1.2 Model-Updating Using EMA

Table 6.1 also contains the results of a validation experiment in the form of EMA, performed according to Chapter 4.2.2. A comparison to iteration #5 of the simulations reveals that although the numerical solution has converged, there are still deviations of more than four percent between simulation and experiment. The model quality might profit from analyzing and possibly eliminating the causes of variance.

Taking a closer look at the results of the mesh-grid convergence above reveals that the natural frequencies of all ten modes are higher in the simulation than in the experiment, regardless of mesh refinement. This is an indication that the cause of the deviation most likely lies in global parameters, such as geometric or material properties. At the same time, the magnitude of deviation is not the same over the four different mode types. In ovalization modes, the deviation is significantly higher than with the other mode types. Taken together, the two findings imply that the discrepancies between simulation and experiment are most likely caused by deviations in more than one global parameter. A straightforward way to validate an FE-model intended for dynamic analysis, is to check the mass. In this case, the comparison between the model and the physical component of the core bit revealed, that the model shows a slightly higher mass. The next step consists of checking the geometric dimensions of the physical core bit. The outer diameter of the steel tube turns out to be a few hundreds of a millimeter smaller than the nominal value used to build up the model, still being within the specified manufacturing tolerance, though. While the deviation is minimal, in such a slender cross-section as that of the steel tube, it has a noticeable influence on the natural frequencies. Simulation #6 contains the updated geometry and already shows a good improvement when compared to #3 and even in comparison to #5. A method to include uncertainty in geometric parameters in the calculation of natural frequencies is presented in [123] using a bladed rotor as an application example.

The correlation between experiment and simulation can be further improved by adapting the Young's modulus of the steel tube. In simulation #7, the Young's modulus is changed by approximately 1.4 % from 210 GPa to 207 GPa, resulting in an almost perfect match compared to the experimental data. According to *Langer et al.* [78, 79], 1.4 % deviation in

the Young's modulus is a reasonable range of uncertainty.

Another important parameter to validate is the damping. The current simulation model considers damping in the form of material damping and discrete viscous dampers, as in the model approach of the bearings (see Chapter 5.2.2.1), or to account for the influence of the human operator (see Chapter 5.2.6). Besides the natural frequencies, Table 6.1 also contains experimentally identified modal damping ratios ξ_i, expressed as a fraction of critical damping. In the following discussion, one should keep in mind, however that impact testing is not known to produce very accurate results with regard to modal damping. The nominal difference between the values, ranging from 0.05 % to 0.1 %, should therefore not be overestimated. A careful assessment comes to the conclusion, that the damping does not differ much between the different modes, and is in good agreement with generally accepted values [49, 152], stating a material damping of 0.1 % for steel as well as for aluminum.

ABAQUS offers several possibilities to consider material damping. In the current case, it makes most sense to assume Rayleigh damping, which treats the overall damping as a combination of mass proportional (low frequency range) and stiffness proportional (high frequency range) damping. This approach requires one to specify two Rayleigh damping factors, α_R for mass proportional damping and β_R for stiffness proportional damping. The modal damping ratios and the two damping factors stand in the following relationship [122]:

$$\xi_i = \frac{1}{2}\left[\frac{\alpha_R}{\omega_i} + \beta_R \omega_i\right] \tag{6.1}$$

in which ω_i stands for the natural (circular) frequencies. Once the modal damping ratios ξ_i are known from EMA, the two damping factors α_R and β_R can be identified by solving the overdetermined system of equations by using a least-square-error method.

As an interim summary, what can be noted is that modal analysis is a powerful tool to verify and validate the model representation of single components. Analyzing the cause of possible deviations and updating model parameters where necessary can significantly increase the confidence in the model. Verifying and validating the model from the bottom up, significantly reduces the sources of possible deviations when now turning to the full model.

6.2 Whole System

Modal measurements at non-rotating condition of the rotor system as a whole provide the reference for validating and updating the simulation model. First, the hypothesis needs to be validated, according to which the non-rotating parts of the machine, such as the housing and the additional sensor rig, can be considered rigid within the frequency range of interest, thereby allowing one to represent these parts as lumped masses in the model. This is the content of the next section, while subsequent chapters deal with how to use FRF measurements to identify the damping coefficients of the bearings and the dynamic parameters of the human operator.

6.2.1 Results of EMA

When all sensors are implemented for operational measurements, the setup lends itself to modal impact testing using the roving hammer method. This method allows one to measure a large number of DOFs with acceptable effort, without running into mass-loading effects by changing the position of the sensors during the measurements. In the model, the added mass by the sensors installed for operational measurements is accounted for. Figure 6.2 shows the average sum of all measured FRFs, both for the vertical direction (x-direction) and the horizontal direction (y-direction). In total, more than 150 DOFs have been measured. The mode shapes identified by EMA can be animated and thereby studied in detail using a wire-frame model created out of the geometry of the measured points. In a static picture, the only way of presentation possible within this thesis, a wire-frame presentations is not very comprehensible, however. Therefore, Figure 6.3 uses the results of the simulation model instead to represent selected mode shapes.

The first global structural mode is a vertical bending that occurs at 33 (normalized) Hertz. As can be seen from Figure 6.3 a), the non-rotating parts behave as a rigid body, and the mode shape consists of a counter-phase movement between the drive shaft and the rest of the rotor system. As indicated by the sectional view in Figure 6.3 c), most of the compliance comes from the shaft itself, while the chuck, the core-bit and the tumble sleeve are much stiffer in comparison and perform mainly a rigid body motion. The horizontal bending occurs at a slightly higher frequency of 34 [Hz], while for the mode shape, the same applies, as has been said for the vertical mode: It is a counter-phase movement between the drive shaft and the rest of the machine.

The next mode is a vertical bending of the sensor support rig at 97 [Hz], as indicated by

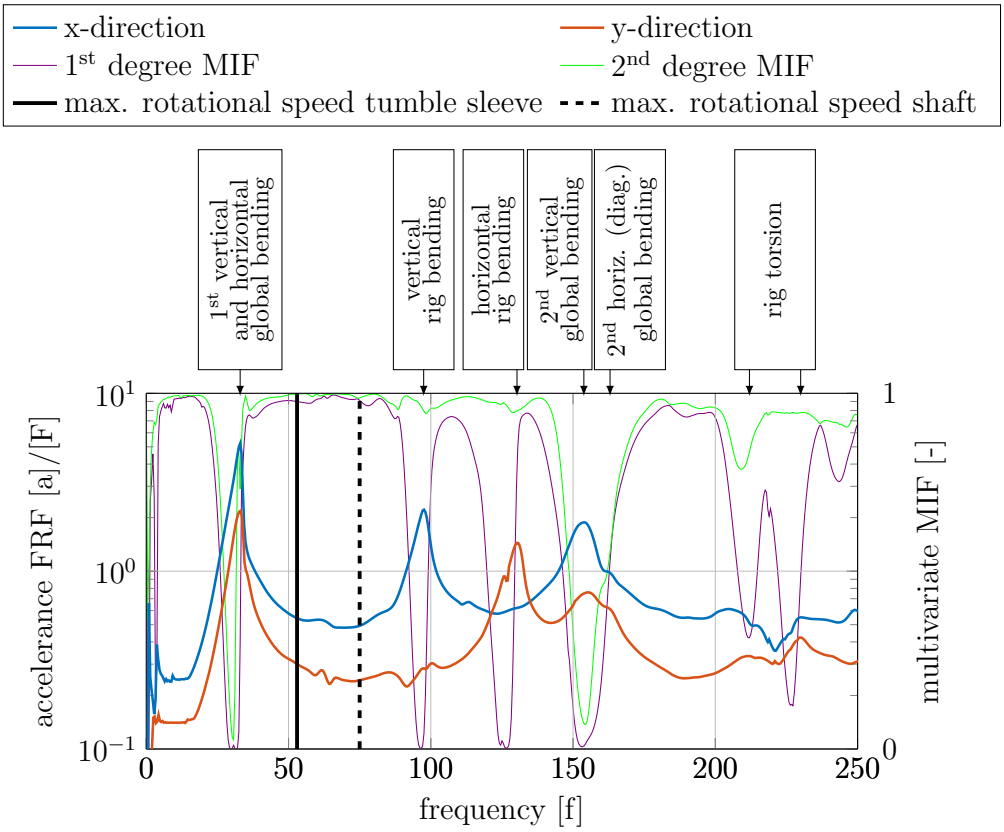

Figure 6.2: Sum-FRF of the whole rotor system including sensor support rig

Figure 6.3 d). The corresponding horizontal bending occurs at 130 [Hz]. Since the natural frequency of the rig-bending is three times higher then the bending mode of the drive shaft, the rig can be considered rigid in the model within the given maximum operational speed. Both, the natural frequency of the vertical and the horizontal rig-bending mode are located well above the range of the operational speed of the tool and are not excited during operation.

At 153 [Hz] for the vertical direction, respectively at 163 [Hz] for the horizontal direction, the second bending of the drive shaft occurs. Here, the housing deforms elastically and can no longer be considered rigid in the model. However, the natural frequency of the second bending of the drive shaft occurs way above the maximum operational frequency of the rotor system and is not excited during operation. The measurement shows further local and global modes at higher frequencies, but since they are out of interest within the current problem, they are not discussed further.

As an interim summary, one can state that the EMA of the whole system provides good information about the modal behavior that can act as a reference when updating the model. The sensor rig has been designed that it shows no local modes within the operational range

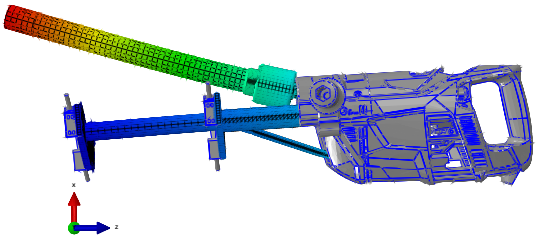

(a) 1st vertical global bending

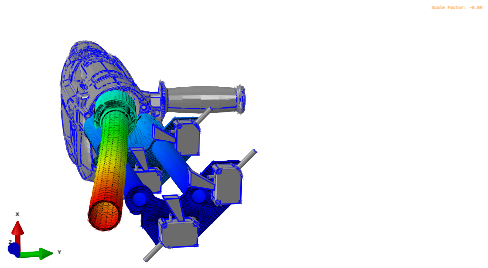

(b) 1st horizontal global bending

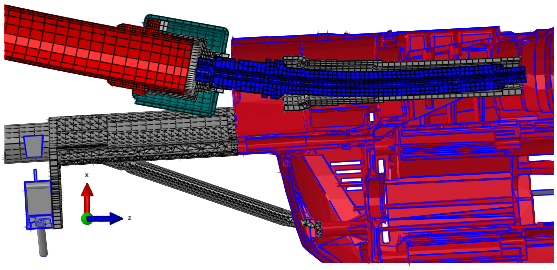

(c) sectional view of 1st vertical global bending

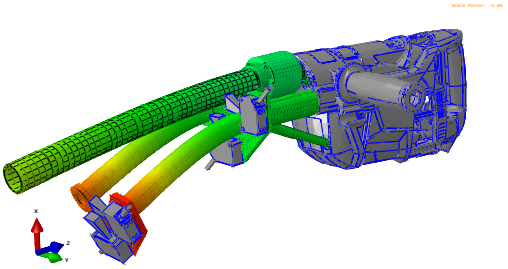

(d) vertical rig bending

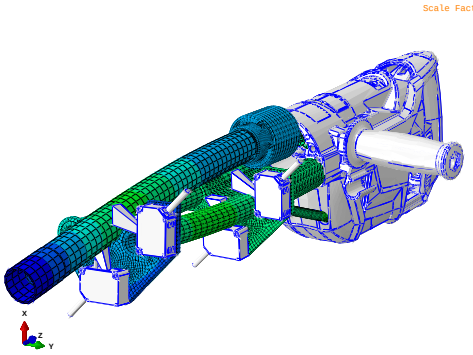

(e) 2nd vertical global bending

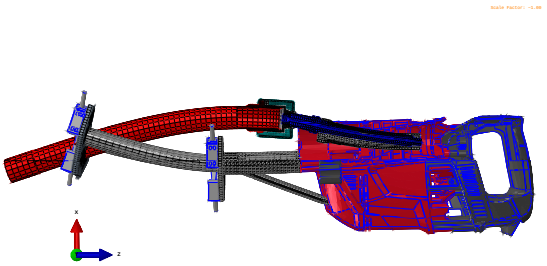

(f) sectional view of 2nd vertical global bending

Figure 6.3: Selected mode shapes of the whole rotor system

of the rotor system. The measurements confirm the computational design of the rig. The approach to represent the sensor rig and the non-rotating parts of the tool as rigid bodies is confirmed by the measurement data. In the next step, the results of the EMA will be compared to simulation data.

6.2.2 Model-Updating

The previous section showed good results from the EMA of the rotor system as a whole. In the chain of validating the model, the next logical step would be to perform a modal analysis in the simulation model and to compare the results. This comparison, however, is not as straightforward as it may seem at the first glance.

The deep-groove ball bearings and the force-locked chuck provide a nonlinear stiffness characteristic, which is represented likewise in the simulation model, as described in Chapter 5.2.2. As a consequence of the nonlinear stiffness behavior, the dynamic response of the rotor system to hammer excitation during EMA depends on the amount of force that is used. The experimental result can be interpreted as a kind of physical linearization around the working point. If the simulation model is not linearized around the same working point, the results are not comparable. In ABAQUS, the bearing stiffness is defined in a look-up table that does not directly contain stiffness values, but rather consists of a matrix that associates discrete values of displacement with corresponding levels of returning force. In a linear computation like a modal analysis, ABAQUS uses by default (like most FEM programs do) the first pair of values, which results in a stiffness that is zero or is at least close to it, since it represents the bearing play. Without corrective measures, the natural frequencies out of the simulation would be way to low when compared to those identified by measurements.

Regarding the nonlinear behavior of the force-locked chuck: In the simulation, the contact is considered “closed” in the modal simulation step by default, meaning that the surfaces in contact are tied together. In the measurements, it depends on the amount of excitation force, whether the clamping force between chuck and drill bit is exceeded or not. Chapter 7.4.1 will deal in detail with the nonlinear behavior of the force-locked chuck and its effect on FRFs. The measurement results discussed in the current chapter, however, have been obtained by using a core bit that has been soldered to the chuck, thereby eliminating the force-locked connection.

To compare and update the simulation model with the experimental results, there are now two options: Either to linearize the simulation model around the working point, or to simu-

late the response to a hammer impact using direct time integration, which allows for nonlinear system behavior. In the current thesis, both methods are used to update the model. In a first step, a set of linear stiffness parameters is identified, but instead of using linearization techniques, the parameters are obtained in an optimization process controlled by OPTIMUS. With these results, the mode shapes are checked. Alternatively, the linearization could be achieved by use of the harmonic balancing method, which is the most popular method for nonlinear problems [143, 149]. In a second step, FRFs are computed by applying the measured time history of the hammer force signal at the core bit tip to the model and solving it through implicit time integration. A comparison between simulation and measurements is shown in combination with the human hand-arm system in Figure 6.4 of the subsequent chapter.

6.2.3 Dynamic Parameters of the Human Operator

As described in Chapter 5.2.6, the human hand-arm system is modeled as a spring-damper system, while the added mass is surcharged to the inertial mass parameters of the machine. The stiffness and damping parameters, as well as the added mass is identified by performing FRF measurements of the whole rotor system at stand-still condition. In the first measurement, no operator is present and the tool is suspended in elastic strings to simulate free boundary conditions. The measurement is then repeated with the operator gripping only the side handle, then only the rear handle, and finally both handles. Since the parameters of the hand-arm system strongly depend on the gripping force of the operator, the measurement is repeated once more with the operator gripping both handles and applying excessive gripping force. Figure 6.4 shows the influence of the operator on the driving point FRFs taken at the tip of the core bit in both the vertical direction (x-direction) and in the horizontal direction (y-direction). At the time when these measurements were performed, the sensor support rig was not yet manufactured and therefore not mounted. Accelerometers at the core bit tip replace the triangulation sensors to measure the response to hammer impacts. Due to the reduced mass and moment of inertia when the sensor rig is missing, the resonance frequencies reported in Figure 6.4 are higher than those of Figure 6.2. This does not affect, however, the identification of dynamic parameters of the human operator.

The experimental results show a differentiated influence of the human hand-arm system over the frequency range as well as with regard to the directionality (vertically vs. horizontally). In the frequency range of the first bending resonance, the presence of the human operator has a noticeable influence on the dynamic behavior of the rotor system both in terms of

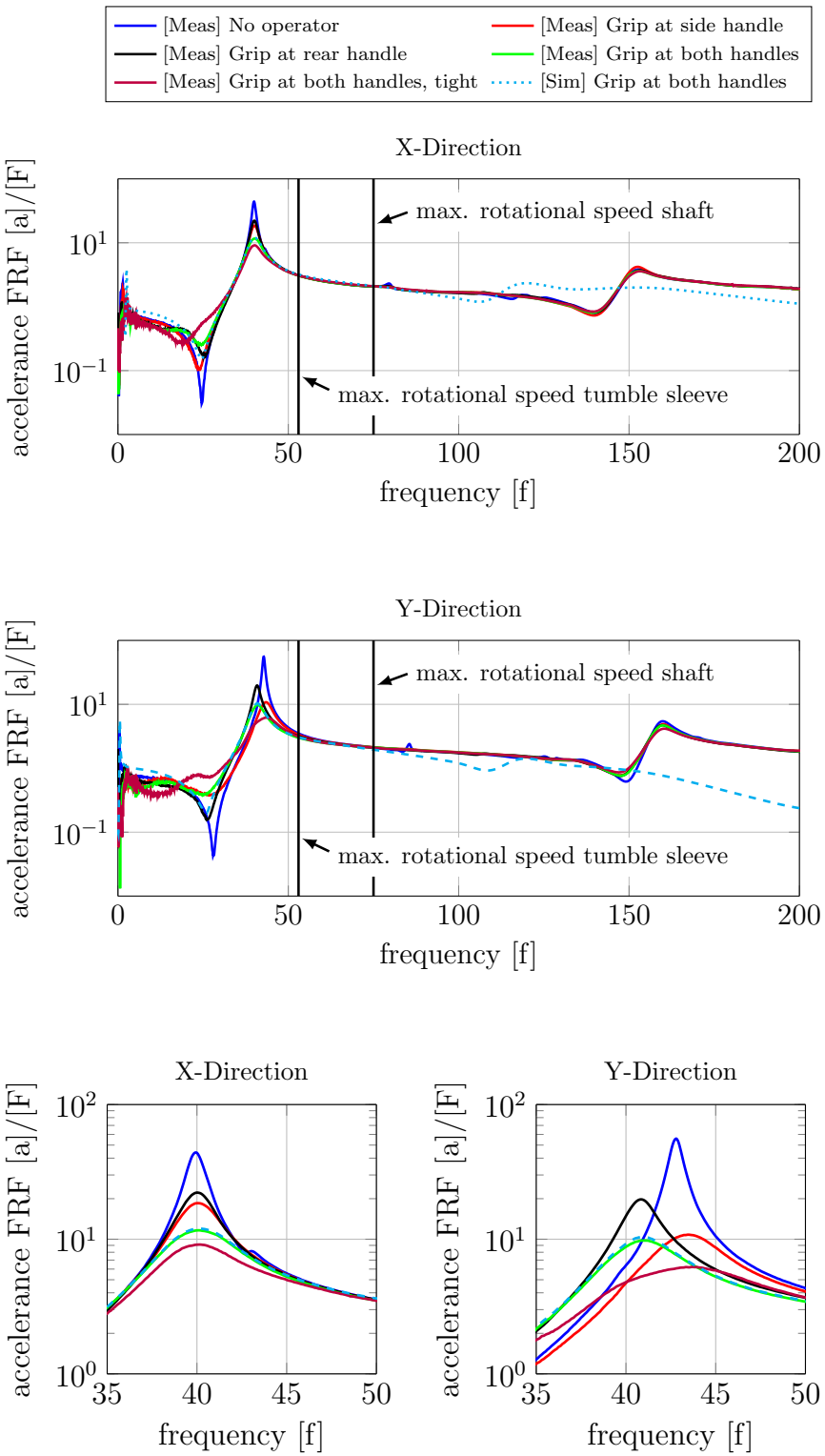

Figure 6.4: Influence of the human operator on accelerance FRF at core bit tip (sensor support rig is not mounted)

damping as well as in terms of mass and stiffness. The influence, however, is different in the vertical and in the horizontal direction, as will be discussed in the subsequent paragraph. In the frequency range above the first bending resonance, the dynamic influence of the operator is far less significant.

With regard to the first vertical bending resonance, there is no considerable influence on the frequency, while the damping is significantly increased by the presence of the operator's hands. The hand at the side handle seems to increase the damping by roughly the same amount than the hand at the rear handle. In the horizontal direction, however, the hand-arm system has a considerable influence on the frequency of the first bending resonance, while the damping effect of the hand arm-system is even stronger pronounced than in the vertical direction. In contrast to the previous results, the increase in damping in the horizontal direction is mainly caused by the operator's grip at the side handle, while the influence on the natural frequency is mainly the result of the hand at the rear handle.

Generally speaking, these results are in accordance with the works of Kinne [68–70] and Adewusi et al. [2, 3], insofar as the dynamic parameters of the left and right hand are not the same, but depend on the posture. However, the difference in the dynamic parameters between the two directions perpendicular to the forearm (x- and y-direction in the current tool coordinate system) seem to be larger than in most models, i.e. Kinne or ISO 10068. This becomes visible, when regarding the influence of the hand at the rear handle, which significantly changes the natural frequency of the horizontal bending resonance, but leaves the frequency of the vertical resonance completely unchanged.

In the next steps, the results of the modal analysis must be transferred into setting the parameters of the spring-damper system, which represents the human hand-arm system in the model. Focus of interest is the first bending mode. So far, the results have been discussed with regard to the influence on the natural frequency and damping of that mode. To transfer these results to the model, the influence of the hand-arm system on this bending mode needs to be discussed in terms of added stiffness, mass and damping.

Extracting the stiffness parameters: Without any further knowledge, the fact that the presence of the operator does not influence the natural frequency in vertical direction could be interpreted in two ways: Either there is no significant mass or stiffness effect from the hand-arm system at this frequency range at all, or the influence of the added stiffness and mass are mutually compensating each other. However, the reason why the natural frequency of the bending mode is so much higher than the rigid body modes is simply due to the fact that the bending stiffness is higher by dimension than the stiffness provided by any of the

hand-arm models mentioned in Chapter 5.2.6. This also means that the added stiffness of the human hand-arm system can be regarded as irrelevant on the bending mode. Therefore, the stiffness in the simulation model is defined in such a way that the system acts stable during the start-up phase of a run-up: To save simulation time, the system is run-up rather fast at the very beginning, as will be explained in Chapter 7.3. This creates a high torque reaction, which must be compensated by the operator. In the real world, the operator applies corrective forces and torque, to bring the tool back to its neutral position. Since openly available hand-arm models are purely passive mechanical systems, they lack this active control behavior, resulting in unrealistically large (rigid body) motion during the start-up phase. Therefore, the stiffness is defined rather high to keep the motion in a reasonable range.

Extracting the mass parameters: Experimental research presented amongst others in ISO 10068 show that the apparent hand-mass strongly decreases towards higher frequencies in which the bending mode is located. According to these references, the apparent hand mass is different in the x_h and the y_h direction of the hand-coordinate system. Since the presence of the operator's grip shows no influence on the natural frequency of the vertical bending mode, the added mass of the hand-arm system is ignored in the vertical direction and in the moment of inertia around the y-axis. In contrast, the added mass in the horizontal direction cannot be neglected. To represent it in the model, the moment of inertia of the machine around the y-axis is increased until the simulated natural frequency of the bending mode matches the measured frequency for the case in which the operator grips both handles.

Extracting the damping parameters: The presence of the hand-arm system shows a strong dampening effect on the first bending mode. In the model, this effect is represented as a damper with a viscous damping constant. The constant is adapted to match the FRF measurements at the tip of the core bit. Research has shown, however, that the dampening effect of the hand-arm system decreases towards higher frequencies. In the model, the damping constant is set so that the simulated FRFs resemble the measurements within the frequency range around the first bending mode.

Along with measurement data, Figure 6.4 also contains the results of the simulation model. Updating the model parameters as described above creates an almost perfect match between simulation and measurement within the whole frequency range that is excited during a run-up of the rotor system. At higher frequencies, however, there are significant discrepancies in the resonance frequencies as well as in the amplitudes. The difference in the resonance frequencies is a result of assuming the housing of the machine rigid, which is perfectly valid in the frequency range of interest, but not in the higher frequency range. The difference in

amplitude is a consequence of assuming viscous damping of the hand-arm system and by tuning the damping constant for the first bending frequency. This leads to an over-damping in the higher frequency range, which is totally acceptable in the current case.

7 Simulation and Experimental Results

The current chapter evaluates the quality of the simulation model, its capabilities and its limitations. At the beginning, the global dynamic system behavior during run-up and run-down is described by means of experimental data. This is necessary to understand the identification process of two missing parameters, namely the drag torque of the system and the imbalance of the core bit. The actual discussion of simulation results and a comparison to measurements is split up in two different cases: First, for so-called "normal" operating conditions in which the clamping force of the force-locked chuck is sufficient to hold the core bit in place during run-up. This is followed by the case in which the clamping force is intentionally exceeded by reducing the pre-load and by additionally increasing the imbalance of the core bit or the tumble angle of the sleeve. In the latter case, mode-locking is observed in the experiments, which can only be represented accurately in the simulation model by the use of 3D solid modeling, as shall be seen in what follows.

7.1 Global Dynamic System Behavior

To predict the dynamic behavior of a system, it is necessary to look at the natural properties like eigenfrequencies, mode shapes and damping, as well as at the excitation forces.

Starting the discussion with the excitation forces, one can state that the current rotor system contains three rotating subsystems: the drive shaft, the tumble sleeve and the electric engine. An obvious excitation mechanism is the natural imbalance of each rotor, which creates speed-dependent excitation forces. However, since the electric engine is precisely balanced and operates sub-critically, the main excitation mechanisms can be expected to arise from the natural imbalance of the drive shaft and from the tumbling movement forced by the sleeve.

Turning now to the natural behavior of the rotor system: In Chapter 5, the natural behavior of the system was evaluated in non-rotating condition. At rest, the system has a vertical (in the xz-plane) and a horizontal (in the yz-plane) bending mode in which the natural frequencies are located well within the range of rotational speed of the three spinning subsystems mentioned above. Therefore it can be expected that when the rotational frequency of one of the rotors matches the natural frequency of one of the bending modes, a resonance will occur, leading to large amplitudes. However, in a rotating system, the natural frequencies usually depend, to a smaller or larger extent, on the rotational speed. This means that the resonance frequencies during operation do not necessarily have to match the natural frequencies measured or calculated at non-rotating condition. The speed dependency of natural

frequencies depends on the ratio between the polar and the diametral moment of inertia of the rotors. In the current case, the rotating components of the diamond coring systems are relatively slender; so no large speed dependency is to be expected.

According to the results in Chapter 6.2, the mode shape of the first bending mode(s) is mainly a bending of the drive shaft against the rest of the tool, which performs an almost rigid body motion. Therefore, during operation, the largest displacement amplitudes in the case of a resonance can be expected at the tip of the core bit or at the rear handle. Figure 7.1 shows the time signal of the displacement amplitude of the core bit tip in vertical direction (x-direction) relative to the housing during a slow run-up and run-down of the system. The same plot also contains the time signals of the rotational speed of the drive shaft and the tumble sleeve. The signals are recorded according to the experimental setup described in Chapter 4.

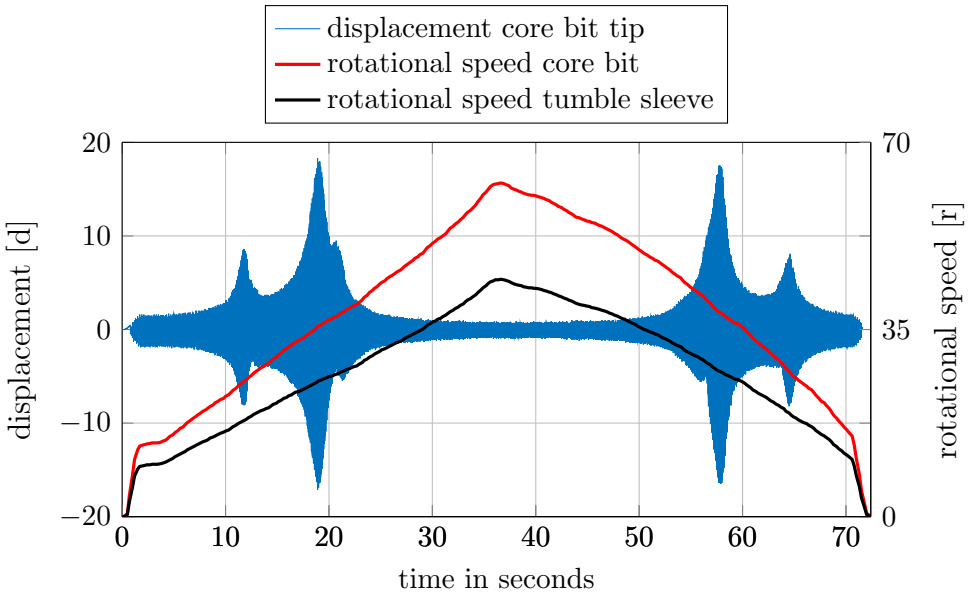

Figure 7.1: [Meas] Vertical displacement of core bit tip relative to housing during slow run-up and run-down

The plot shows two major resonance phenomena during run-up and run-down. The first, and in this case smaller peak, is caused when the rotational frequency of the drive shaft matches the natural frequency of the first bending mode. The second resonance peak occurs, when the rotational frequency of the tumble sleeve matches the natural frequency of the bending mode. Looking closely at the resonance peaks, one can see that each of them shows a smaller side peak caused by the excitation of the horizontal bending mode. The unwanted, yet in the current case unavoidable, cross-sensitivity of the triangulation lasers causes a “cross-talking” between the horizontal and vertical channels, as discussed in Chapter 4.1.1 and visualized

in Figure 4.2a. Since the horizontal bending mode has a slightly higher natural frequency, the corresponding resonance during operation appears a little delayed in time during run-up, or at a slightly higher rotational speed, respectively. During run-down it is the other way round.

Assigning the resonance peaks to a certain excitation mechanism becomes easier by plotting the data (i.e. displacement or acceleration) over rotational speed instead of time. In Figure 7.2, a vibration order analysis according to Chapter 4.3.2 has been performed to calculate the overall displacement level, as well as the share that can be assigned to the first order of the drive-shaft, the tumble sleeve and the electric engine. Since the ratio of the rotational speeds between the three different rotating subsystems is fixed, one of them can arbitrarily be chosen to act as a reference and the other two can be expressed as multiples of the reference. For example, the first order of the drive-shaft can be considered as the n-th order of the sleeve, according to Equation 3.1. This allows for the plotting of all three orders on the same scaling of the x-axis. In Figure 7.2, the tumble sleeve acts as a reference. Since no torsional oscillations between shaft and tumble sleeve could be observed in any experiment performed within the current work, the signal of the rotational speed of the core bit is simply a multiple of the signal obtained from the tumble sleeve, and is therefore redundant information. As a consequence, all further plots will present information about rotational speed using the signal of the tumble sleeve instead of using both tacho signals.

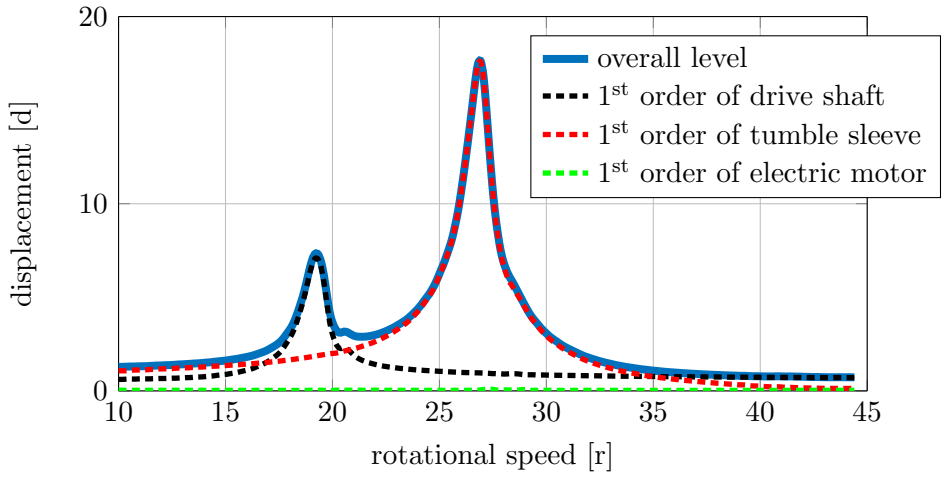

Figure 7.2: [Meas] Overall-level and order-plot of vertical displacement of core bit tip relative to housing during slow run-up

Comparing the share of the orders to the overall displacement level indicates the following with regard to the three different main excitation mechanisms :

- The first resonance occurring during run up is excited almost solely by the natural imbalance of the drive shaft.
- The second resonance is caused almost completely by the excitation through the tumble movement.
- The excitation by the first order of the electric engine (imbalance) can be neglected with regard to the dynamic displacement of the core bit.

The two resonances appear to be well separated, meaning that each resonance is dominated by only one of the excitation mechanisms, the imbalance of the drive shaft and the forced tumbling movement by the sleeve. This is confirmed when regarding the corresponding Campbell diagram in Figure 7.3: The relevant frequency of the first bending mode is clearly dominated by the two excitation mechanisms described above. The two resonances appear at the same frequency, and – interestingly – at the same frequencies as the natural bending frequencies (first vertical and horizontal bending) when the system is not rotating. This is a double indication of the fact that the natural frequencies of the first bending mode are not influenced by the rotational speeds of the rotors. The reason for this is the fact that the rotors are very slender, meaning that the polar moment of inertia is significantly smaller than the diametral one.

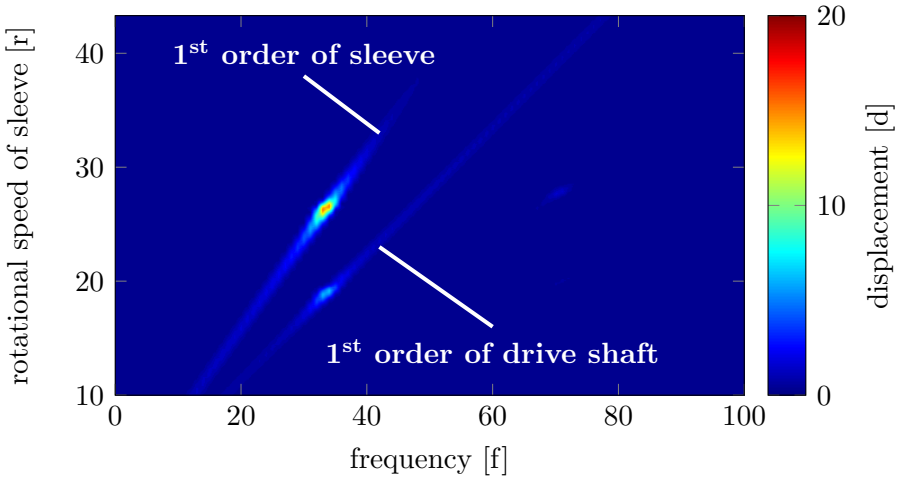

Figure 7.3: [Meas] Campbell diagram of vertical displacement of core bit tip relative to housing during slow run-up

Chapter 6.2 deals with the modal behavior of the whole system, pointing out that the first global bending mode is mainly a counter-phase movement of the core bit against the

rest of the system. In the experimental setup for operational measurements outlined in Chapter 4.1.1, the measurement position at the tip of the core bit and at the rear handle ("tool 3") mark the two extreme positions of the moving bodies with a vibration node between them. Therefore it comes as no surprise that, in a run-up, the signal of the two sensor positions may have different amplitudes due to different modal effective masses of the corresponding bodies, but, qualitatively, they show the same curves, as indicated by Figure 7.4 in the form of the overall level.

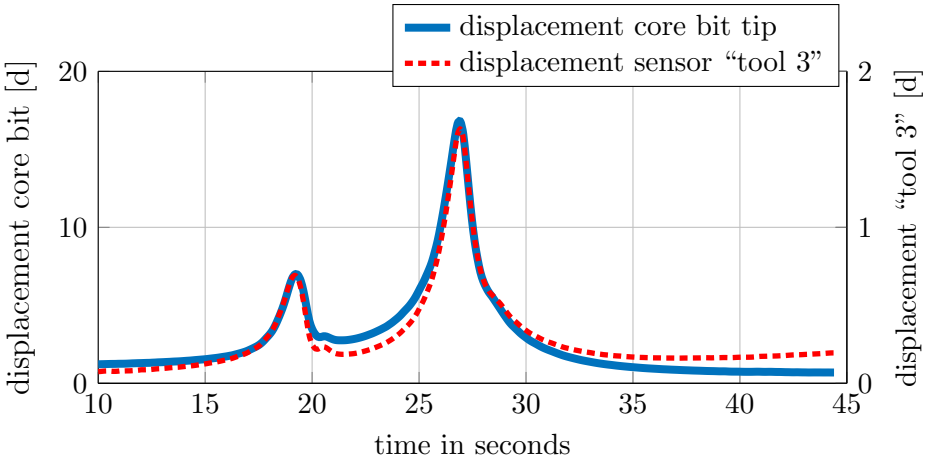

Figure 7.4: [Meas] Comparison between vertical displacement of core bit and of sensor position "tool 3" during slow run-up

7.2 Updating the Model in Rotating Condition

Not all input parameters for the simulation model can be acquired from measurements at non-rotating condition. These include the drag torque of the system and the imbalance of the core bit, which need to be identified from operational measurements, as will be explained in what follows.

7.2.1 Identifying the Imbalance of the Core Bit

As discussed above, the core bit shows a significant imbalance during operation that needs to be accounted for in the model. Identifying the imbalance of rotating systems is a task that is firmly established in industrial manufacturing processes. In the current case, however, identifying the imbalance of the core bit is not easily done.

The core bit consists mainly of a tube with a diamond crown on the drilling side and a connecting end on the other side. The imbalance, however, does not arise from an asymmetric

mass concentration, but is mainly the result of an angular misalignment between the axis of symmetry and the axis of rotation that arises at the connection between the chuck and the connecting end of the core bit. This can easily be shown by attaching the core bit to the chuck in its three possible inserting positions and performing a measurement in each position. Figure 7.5 shows the displacement of the core bit tip during run-up for all three positions. Due to a different angular misalignment in each inserting position, the resonance amplitude caused by the imbalance of the core bit varies significantly over the different inserting positions, while the resonance caused by the tumble movement remains almost unchanged. The later is another confirmation, that the two resonances, caused by the two different excitation mechanisms, are two well-separated effects.

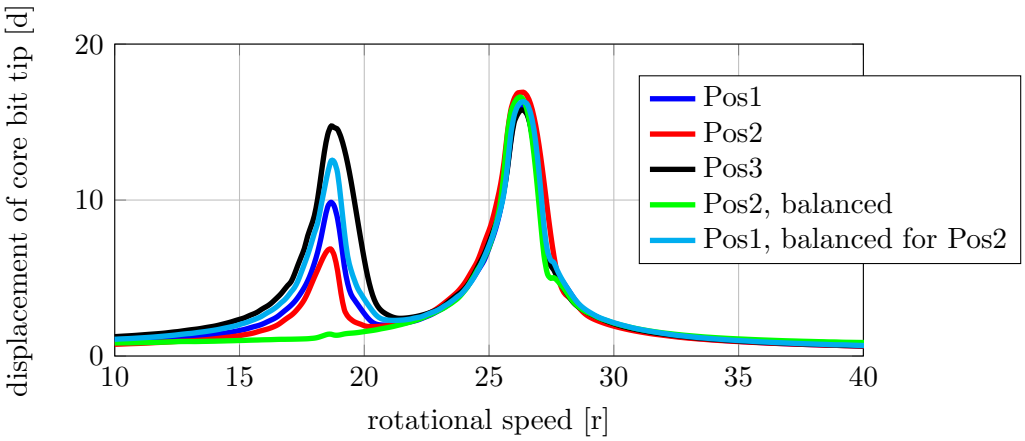

Figure 7.5: [Meas] Overall-level of vertical displacement of core bit tip in different insert positions

In the simulation model, the imbalance resulting from a misalignment of interconnected rotating parts can be represented in two different ways. The first possibility is to actually represent the misalignment in the model. However, a rotor that is not rotating around a principal axis of inertia opposes serious difficulties in the case of modal computations, as explained in Chapter 2.1. In the current case, this is of secondary importance since the drive shaft performs an additional tumbling movement anyway in addition to spinning around its axis of rotation. Furthermore, the dynamic response of the system is computed by using implicit time integration because of the transient rotor speed during run-up and the nonlinear stiffness behavior, which will be outlined in detail in Chapter 7.4. The second option to account for the imbalance of the core bit is to model it perfectly symmetrically to its spinning axis and add an according imbalance mass that is eccentrically placed with regard to the axis of rotation. In the current case, the extra mass is added as a point mass at the outer rim of the diamond crown at the tip of the core bit. In ABAQUS, the point

mass is attached to the nodes of the diamond crown using MPCs. This is of course a very simple way of representing the imbalance in the model, but, as shall be seen in what follows, it turns out to be sufficient.

So far, the cause of the imbalance of the core bit has been discussed, as well as the way of representing it in the model. What remains to be done is to identify the amount of imbalance as an input for the simulation. The preferred way would be to directly measure the imbalance with the help of an appropriate balancing machine. In the past, dozens of different procedures and devices have been developed to accomplish such a task. In the literature, an overview of balancing technology can be found, amongst others, in [121]. In the current case, the proprietary connecting end opposes a difficulty, as it requires the manufacturing of a special adapter that allows one to connect the core bit and the chuck to a balancing machine. To circumvent this problem, the balancing is done *insitu* by simply adding balancing weights at the core bit tip until the first resonance during the run-up disappears. The amount of extra mass necessary to completely balance the core bit multiplied by the radial distance to the centerline is then equal to its original imbalance. The procedure is straightforward; the only problem is determining the angular position to which the balancing weights need to be added. In the given measurement setup, the rotational speed is acquired by using an optical probe in combination with a striped tape as described in Chapter 4.1. The so-called zebra tape has a butt-joint where the two ends come together, providing a reference for an absolute position in addition to the rotational speed (see Chapter 4.3.1). Following the model approach of considering the imbalance as a point mass at the tip of the core bit, this reference allows one to identify the angular position of the existing imbalance. By attaching small weights with known masses at the opposite side, the core bit can be perfectly balanced, while simultaneously identifying the imbalance needed as an input parameter for the simulation model. The green curve in Figure 7.5 shows the results of such an experiment. Insert position 2 is chosen as a starting point because it contains the smallest natural imbalance of all three position and therefore requires the least amount of balancing weights. As can be seen, the first resonance peak during run-up completely disappears with the right amount of balancing weights. However, the balancing as well as the amount of identified imbalance is valid only for this one inserting position. The navy blue curve in Figure 7.5 shows the results for putting the core bit back to insert position 1 after balancing it in position 2: Now the resonance peak is even higher than in the first place. This means that to identify the imbalance of the insert positions other than position 2, the extra weights need to be removed and the procedure needs to start anew.

In the current thesis, the extra weights are removed for further measurements once the amount and the angular position of the imbalance is identified. Another option would be to leave them on, meaning to start with a perfectly balanced core bit and add another extra weight at a specific angular position of interest.

7.2.2 Run-Down to Identify the Drag Torque

An important parameter with regard to transient rotational speed and with regard to the torsional behavior of the rotor system is the drag torque. Chapter 5.2.2.3 describes the considerations and the modeling approach. The idea is now to derive the overall drag torque experimentally from a run-down of the system and to approximate it by a combination of a speed-dependent term and a constant frictional torque, as described in Equations 5.6 to 5.8.

The corresponding experiment consists of running up the rotor system, holding it at maximum speed for a few seconds to stabilize, then shutting off the power supply and letting the system coast down. Figure 7.6 shows the measurements of the rotational speed, also indicating the part of the signal that is used for the identification of the drag torque. Based on the rotational speed Ω, the rotational acceleration $\dot{\Omega}$ is computed by numerical differentiation. Due to the imperfect butt-joint correction in the rpm-signal described in Chapter 4.3.1 and due to general noise in the measurements, the signal of $\dot{\Omega}$ requires some smoothing before further processing can continue. Once $\dot{\Omega}$ is known, the drag torque can be computed with the following formula,

$$T_d = \Theta_t \cdot \dot{\Omega} \tag{7.1}$$

in which Θ_t stands for the moment of inertia of the whole rotor system, transformed on the rotor at which the rotational speed is measured.

In the next step, a curve-fitting operation is used to approximate the parameters of the drag torque out of the measured data. According to the assumption mentioned above, in which the overall drag torque consists of a combination of a constant frictional torque and a part that linearly depends on rotational speed, the fitting function is simply

$$T_d = b\Omega + c \quad . \tag{7.2}$$

Figure 7.6 shows a plot over time of the run-down, containing the overall drag torque reconstructed out of the measurements as well as the fitted drag torque, and finally the frictional and speed-dependent part of the fit. The simple assumption of a constant and a linearly

speed-dependent component in the drag torque seems to be confirmed, as the correlation between the fit result and the measured value is very close.

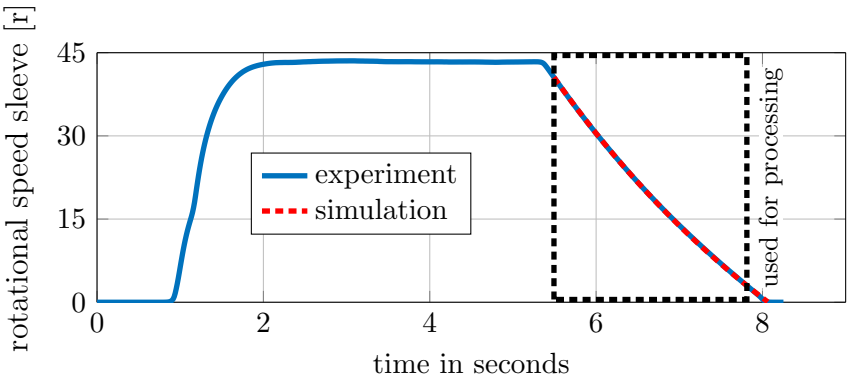

Figure 7.6: Run-down to identify the drag torque

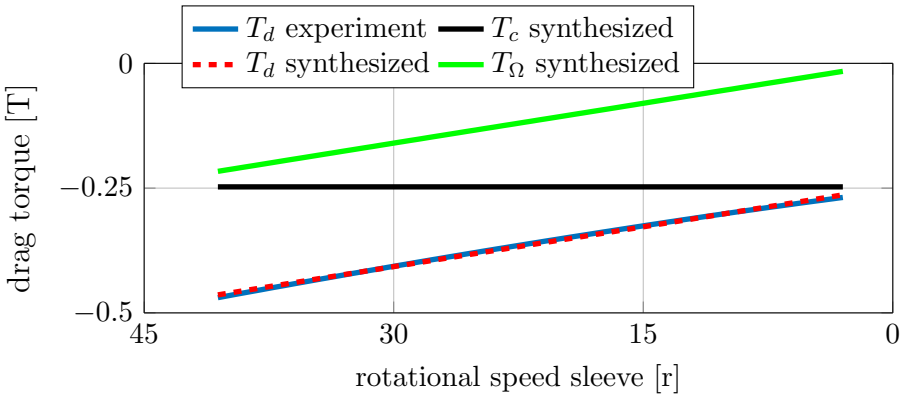

Figure 7.7: Measured and synthesized drag torque

In the next step, parameters b and c need to be translated into values that can be used in the ABAQUS model. According to Chapter 5.2.2.3, the energy dissipation caused by the drive belts is ignored; their share of damping is surcharged on the bearings. In total, there are eight ball bearings. Constant c, which represents the friction independent from rotational speed, is distributed evenly on the eight rolling bearings (two each for the electric drive, the shaft, the tumble sleeve, and finally the toothed belt disk that drives the shaft, see Figure 3.2). Constant b, which describes the speed-dependent part of the drag torque, is distributed on the eight bearings according to their speed ratio. In a more refined approach, one could think of using the diameter of the bearings, or the diameter of their rolling elements, as a weighting factor when it comes to distributing the global coefficients b and c. In the current case, this is not necessary, however. In addition to the measured rotational speed, Figure 7.6 contains the results of a simulated run-down, showing almost perfect correlation and confirming the

simplified approach described above.

7.3 Comparing Simulation Results to Experimental Data in Normal Operation

In the current section, experimental data will be compared to simulation results. The data that has been discussed so far shows the system during "normal operation", referring to a setup of the rotor system in which the clamping force of the force-locked chuck is sufficient to safely hold the core bit during run-up and run-down. It is possible to exceed the clamping force by either increasing the imbalance of the core bit, by increasing the tumble angle of the sleeve or by reducing the clamping force itself. If the clamping force is exceeded, the system shows strong nonlinear behavior leading to interesting dynamic effects that will be discussed in-depth in Chapter 7.4.

The comparison between simulation results and experimental data is carried out on the basis of the dynamic behavior when running up the rotor system. The run-up and run-down in Figure 7.1 has been performed in a very slow way in order to make the main effects directly visible in the time signal without any further post-processing. Since the simulation model uses implicit time-integration to solve the underlying equations of motion, the computational effort is directly related to the length of the physical event that is to be simulated. Simulating a run-up over 30 to 40 seconds would take weeks in real time. This is not feasible while the model might still need updating in operational condition. Moreover, the unmodified serial machine runs up much faster than shown in Figure 7.1. Therefore, the comparison between experimental data and simulation results, shown in Figure 7.8 uses a shorter run-up time. In addition, the system is run-up a little faster in the simulation at the beginning to save computational time. In the beginning of the run-up, the frequency of excitation falls on a quasi-static range of the system and no significant effects occur that need to be covered by the model. The measurements are performed with a different core bit than the one used beforehand. The current core bit has, by chance, a larger imbalance; however, it is a coincidence that in the experiment from Figure 7.8, the first resonance peak, which is caused by the natural imbalance of the core bit, has almost the same amplitude as the second resonance peak, which is caused by the forced tumbling movement of the sleeve.

The comparison between simulation and experiment shows good consistency. Significant effort was spent beforehand when setting up the model, i.e. to gain the non-linear stiffness characteristic of the deep-groove ball bearings and to identify the imbalance of the core bit.

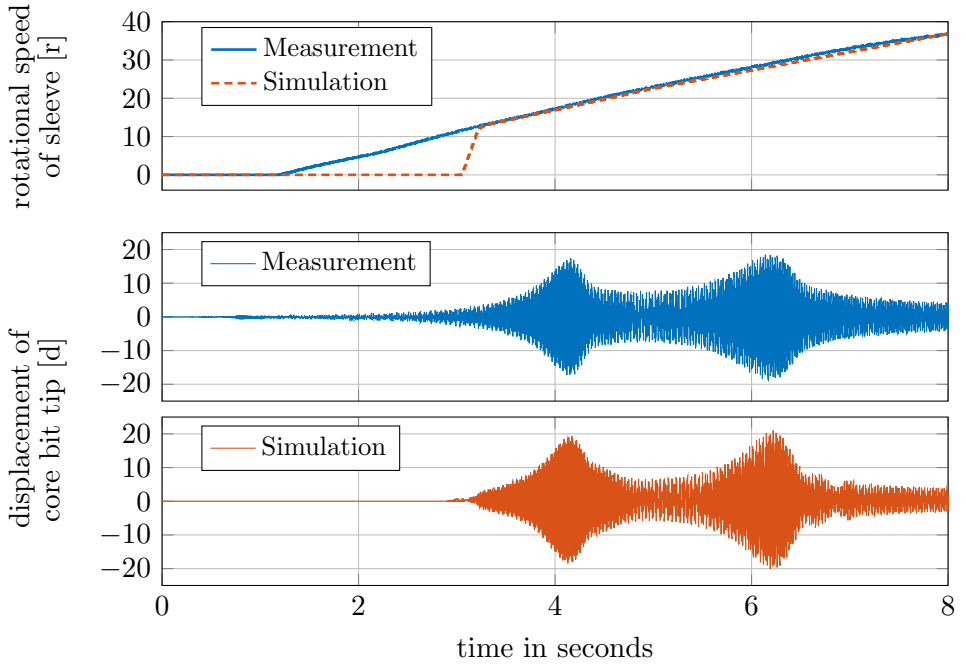

(a) amplitude over time

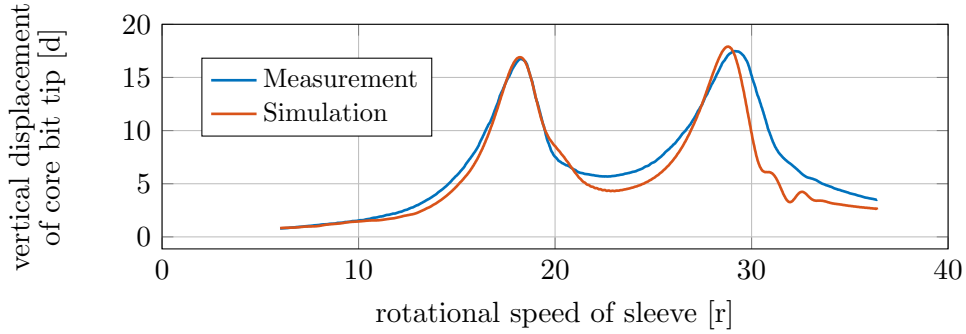

(b) amplitude over rotational speed

Figure 7.8: Comparison between simulation and experimental results at the core bit tip

This effort is now paying out. The frequency of the bending resonance is well met by the simulation model without any further updating. At this point, it is helpful that the shaft provides the largest compliance in the elastic system, therefore reducing the effects of errors in modeling the bearing stiffness that provide possibly the largest uncertainty in the model.

The damping of the hand-arm system that has been identified at non-rotating condition, proved to be too high at the beginning and had to be reduced. Figure 7.8 shows the results after the updating process. One can easily imagine that the damping of the hand-arm system could depend on the vibration amplitude at the handles, thereby explaining why modal measurements with comparably low amplitudes show different results than operational

measurements, in which the amplitudes are higher by at least a dimension. This is, however, not further investigated in the current thesis. Generally, it might be a good idea to identify parameters of the human hand-arm system in operational measurements at realistic loads, instead of using artificial excitation. This requires a model-based identification approach, though, for which the given diamond coring systems is too complicated and opposes too many uncertainties of other parameters than the damping of the hand-arm system.

The fact that the resonance peak caused by the imbalance of the core bit and the peak of the tumble movement are equally well met in amplitude after updating the damping indicates that the imbalance of the core bit has been identified correctly by the *insitu* approach described in Chapter 7.2.1. It also proves the applicability of the hypothesis to consider the imbalance as a single point mass at the tip of the core bit.

7.4 Nonlinear System Behavior due to Nonlinear Stiffness Characteristic

As described in Chapter 3.2.3, the mechanical design concept of the chuck that connects the core bit to the power-tool is that of a force-locked coupling. In the real-world series product, the pre-load of the clamping-spring is, in any case, sufficient to safely hold the core bit and cannot be exceeded in any operational condition. For the sake of the underlying research, the system has been heavily modified – in the sense of rotordynamics, the system is intentionally "worsened" by increasing the imbalance or the tumble angle, while at the same time reducing the clamping force – to intentionally overcome the clamping mechanism in the chuck during operation to study the rotordynamic effects that will be outlined in this chapter.

Once the clamping force of the chuck mechanism is exceeded during operation, the immanent radial play in the chuck allows the core bit to tilt and slip inside the chuck. If this happens while the system is rotating, both the natural system behavior as well as the excitation show strong nonlinear characteristics. With regard to the natural system behavior, one has to keep in mind that the clamping force is generated by a pre-loaded spring. If the spring's pre-load is overcome, the stiffness of the system will change abruptly. More generally speaking, the core bit will be able to perform relative motion with regard to the shaft and chuck, thereby changing the natural system behavior by adding additional degrees of freedom. This nonlinear stiffness characteristic of the force-locked chuck will be described in Chapter 7.4.1.

However, exceeding the clamping force of the chuck not only affects the system's response

to a given excitation, but also affects the excitation itself. Once the core bit is tilting inside the chuck, the out-of-balance forces will increase significantly. Therefore, the overall system behavior will depend on the exact relative motion of the core bit inside the chuck. To be able to simulate this particular relative motion, it is mandatory to represent the precise geometry and the exact contact situation of the relevant components in the model, which is only possible by using 3D solid modeling. This will become even more evident, when discussing the relative motion of the core bit in the chuck in Chapter 7.4.2.

As a result of the afore mentioned changes in the natural behavior and on out-of-balance forces when exceeding the clamping force during run-up, a phenomenon could be observed in which the operational deflection shape adapts to the excitation, or to the rotational speed, respectively, in order to stay in resonance. This can be described as a *mode-locking effect*. Preliminary results have been published in [67]. Essential facts will be repeated in Chapter 7.4.3, complemented by additional information.

7.4.1 Nonlinear Stiffness Characteristic of Force-Locked Chuck

As described above, the force-locked chuck has the potential to create nonlinear system behavior. If the pre-load of the clamping spring is exceeded, the axial and the bending stiffness will decrease significantly. The effect becomes visible by performing the following virtual experiment in the simulation model at non-rotating condition: A linearly increasing static force is applied to the tip of the core bit, while providing fixed boundary conditions to the inner piece of the chuck in the connecting area to the shaft. The simulation is carried out twice: first with realistic, meaning elastic, material properties, and a second time using an unrealistically high Young's modulus to simulate stiffened component behavior in order to separate elastic effects from the kinematic influence. Figure 7.9 shows the contact situation inside of the chuck at the end of the experiment, meaning at high lateral forces. Figure 7.10 contains the corresponding load-displacement curves that will be explained in what follows.

The load-displacement curve of the elastic simulation in Figure 7.10 shows two discontinuities and can be classified as "preloaded piecewise-linear" [47]. The cause for the curve progression can be explained as follows: In the outlined load case, the rotor is positioned as indicated in Figure 3.7, meaning that one pin is standing upright above the middle axis of the drive shaft, while the two other pins are positioned below the middle axis; all three pins together form a tripod. If a lateral force is now applied on the core bit tip in the direction as indicated by Figure 7.9, the topmost pin is pulled axially away from the socket in the inner piece of the chuck, therefore reducing the normal force in the contact. The two lower pins experience

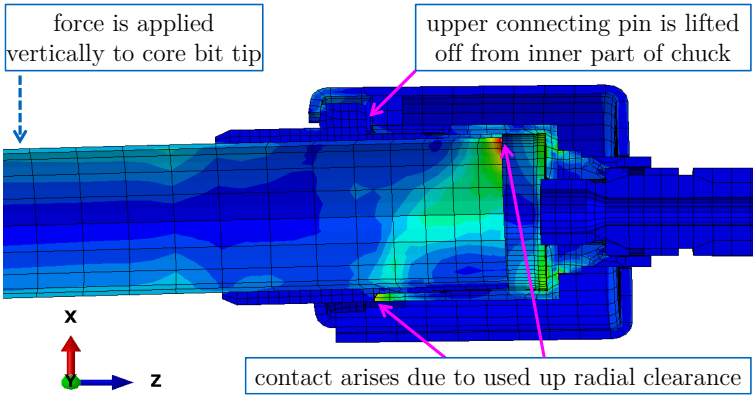

Figure 7.9: Contact situation when the rotor is tilted inside the coupling

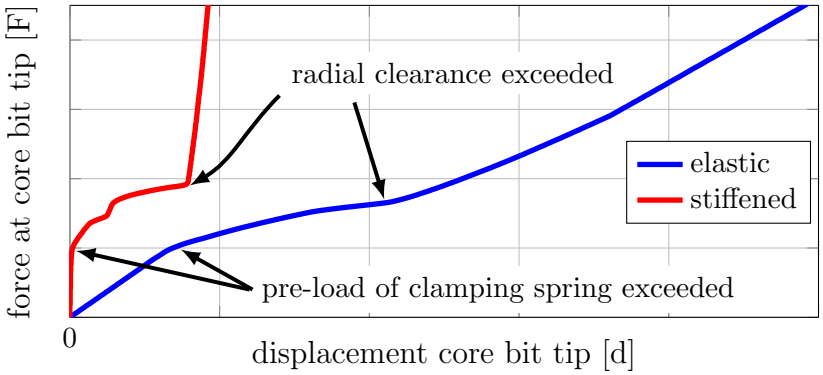

Figure 7.10: [Sim] Lateral stiffness of core bit inside the chuck (load-displacement curve)

quite the opposite, as they are pressed stronger on the sockets of the inner piece of the chuck. When the lateral force on the core bit grows large enough, at a certain point, the axially clamping force can no longer hold the topmost pin, and it is lifted off from the socket, causing the core bit and its connecting end to tilt inside the chuck. The excess of the clamping force creates the first discontinuity in the load-displacement curves. With a further increase of the lateral force, the tilting goes on until the upper rear end of the connecting end of the core bit makes contact with the inner piece of the chuck. Figure 7.9 shows the corresponding contact situation and also the stress distribution in the case of the elastic simulation. As the force increases further, the rotor will slip radially ("downward") inside the chuck until the radial clearance is used up and the lower front of the core bit's connecting end comes into contact with the inner piece of the chuck. The radial slipping creates the second discontinuity in the load displacement curves. In the curve of the stiffened simulation, the slipping can be seen

more clearly than in the elastic simulation. After that, the stiffness level is back to almost the same level as at the very beginning, as the overall stiffness is then dominated by the bending stiffness of the tube-like part of the core bit. To compute the load-displacement curves in Figure 7.10, fixed boundary conditions are applied to the chuck, neglecting the compliance of the rest of system, especially that of the shaft. By taking into account the elasticity of the whole system, the discontinuities in the presented load-displacement curve will be softened significantly, depending on the stiffness relation. However, at this point, it is important to notice that the difference between the stiffened and the realistic load-displacement curves is not only caused by the bending stiffness of the core bit and the single components of the chuck, but is rather caused by the three-dimensional interaction of the whole clamping mechanism, including slipping.

Thinking in terms of a beam-element model: If the core bit would only tilt inside the chuck, it would be conceivable to represent the force-locked chuck as an elastic link with a nonlinear stiffness characteristic. However, due to the "tripod-kinematics", the resulting stiffness depends on the angle relative to the three connecting pins under which the (lateral) load acts on the core bit. This increases the necessary effort to derive the stiffness formulations to an unrealistically high level. Furthermore, each time the core bit slips in the chuck, the kinematics change, leaving it virtually impossible to cover all possible contact situations during operation. Therefore, the connection between core bit and chuck cannot be represented by a beam-model, but rather requires 3D solid modeling due to the complex geometry and kinematics. The model approach chosen in this thesis allows one to correctly represent even large and complicated relative movement, as will be seen in subsequent sections.

So far, the nonlinear stiffness characteristic has been discussed under the use of a purely statical virtual experiment. Another way to research nonlinear behavior in the current case is to perform a linearity test using i.e. hammer excitation while the system is not rotating. Figure 7.11 shows accelerance FRFs taken at the core bit tip using different levels of impact force. Applying increasing force levels to the tip of the core bit results in splitting up a former single resonance peak into two peaks, one at a higher and one at a lower frequency than the original peak. The corresponding mode shapes of the two peaks are identical and do not differ from the shape at a very small force. This dynamic behavior matches the nonlinear but piecewise-linear lateral stiffness characteristic of the chuck-rotor-subsystem well, which is reported in Figure 7.10.

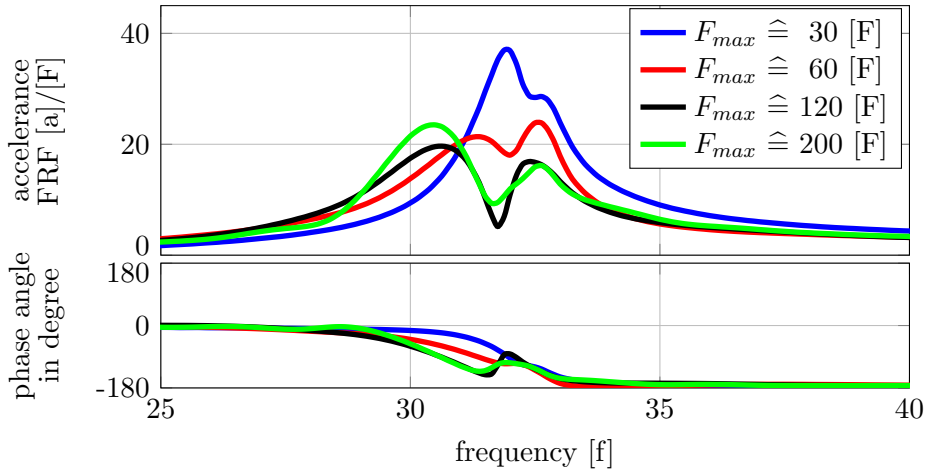

Figure 7.11: [Sim] Accelerance FRFs taken at the rotor tip with varying levels of excitation force

7.4.2 Nonlinear System Behavior Due to Relative Motion of the Core Bit in the Chuck During Operation

The previous section deals with the nonlinear stiffness characteristic of the force-locked chuck in general and shows that the core bit can tilt inside of the chuck under the presence of lateral forces, thereby creating a significant misalignment between the axis of rotation and the center line of mass distribution. So far, the discussion was limited to non-rotating conditions. The current chapter addresses the question of what will happen, if the clamping force is exceeded and the tilting occurs while the system is undergoing a run-up, or more generally speaking, while the system is under rotation.

As already discussed in Chapter 2.1, any lateral displacement with regard to the spinning axis of a rotor will even further increase the out-of-balance forces. This means that any real-world rotor is nonlinear to a greater or lesser extent. What makes the current rotor system so special is the strongly nonlinear stiffness characteristic in the lateral direction, which can result in a tilting movement of the core bit, thereby causing a “jump” in the lateral displacement and, at the same time, in the out-of-balance forces. To provoke the tilting of the core bit in the chuck, the pre-load and the stiffness of the disk spring pack is significantly reduced. By doing so, this also reduces the amount of a lateral force needed to overcome the axial clamping force on the connecting pins of the core bit. The lateral force can now be tuned by increasing the tumble angle φ of the sleeve or by adding additional imbalance-mass at the tip of the core bit. For the following experiment, the latter was done. Figure 7.12a shows the results of a slow run-up by plotting in the upper graph time signals

of the vertical displacement of the rotor tip relative to the housing, as well as the rotational speed of the drive shaft. The corresponding orbit plot (as seen from the housing towards the core bit) for the marked time window is presented in Figure 7.12b.

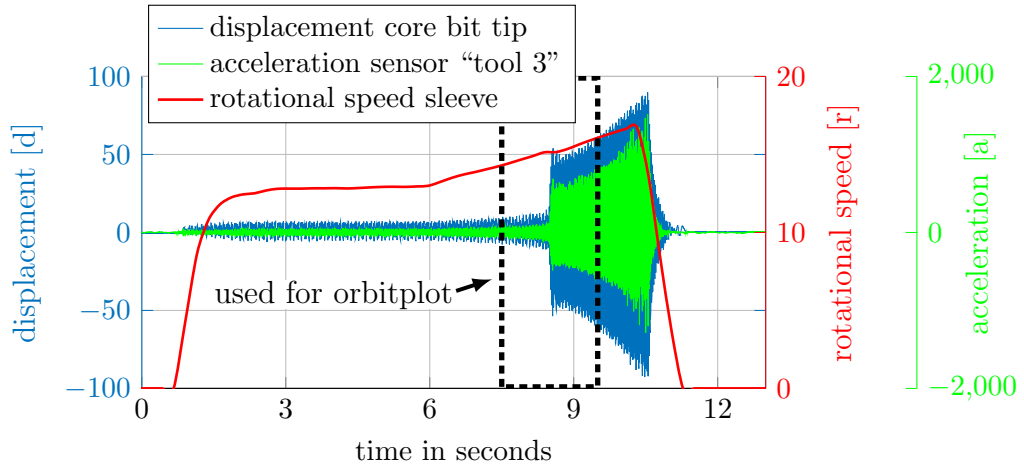

(a) time signal

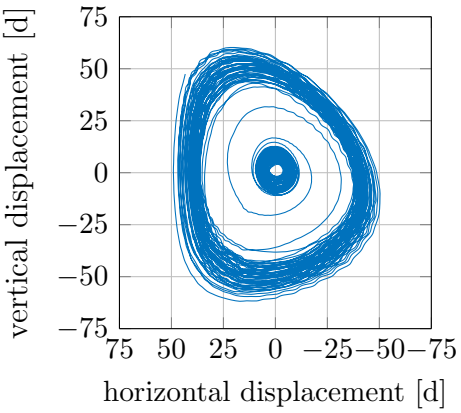

(b) orbitplot as seen from the tool towards the core bit

Figure 7.12: [Meas] Vertical displacement of core bit tip relative to housing during slow run-up with additional imbalance mass at tip

The course of events is as follows: The machine is started and held at low rpm, meaning well beneath the first critical speed. The rotational speed is held constant for a few seconds until the rotor system has stabilized. Then, the actual (slow) run-up starts. As can be expected, the displacement amplitude at the core bit tip increases with increasing rpm as a result of the imbalance excitation. At a certain rotational speed, the imbalance force, acting laterally on the core bit, has reached a level at which the clamping mechanism can no longer hold the core bit in place. It tilts until the radial clearance is used up. The tilting occurs very

abruptly; the whole event takes place in only two rotations, as can be seen in the orbit plot. The result of the tilting event is a massive increase in the displacement amplitude of the core bit tip; the increase is roughly around the factor of four. When comparing the displacement of the core bit tip to the acceleration at the rear handle, it becomes evident that the increase in amplitude of the core bit is not due to kinematics, but rather is the system's response to a significant increase in the out-of-balance forces, as the acceleration amplitude at the rear handle increases by the same amount as that of the core bit. After the tilting occurred, the rpm is further increased, leading to an increase in amplitude, as can be expected from an imbalance excitation. The system does not return to its original configuration and the run-up needs to be aborted because the amplitudes grow too large and endanger the structural integrity.

Before looking at further experimental or simulation results of the current rotor system, the effects of such a discontinuity in the lateral displacement shall be discussed on a more abstract level by using the model representation of a flexible jeffcott rotor exposed to imbalance excitation while running up through a bending resonance. For the sake of simplicity, the jeffcott rotor is supposed to show no gyroscopic behavior.

As outlined in Chapter 2.1, a small imbalance can be treated under certain circumstances as an external force in which the amplitude is equal to the amount of imbalance times the square of the rotational speed. The rotor response to an arbitrarily chosen imbalance $\hat{U_0}$ is represented by the blue curve in Figure 7.13. In a rotor with linear stiffness, ten times the amount of imbalance $\hat{U_0}$ would simply result in a response that is ten times higher, represented by the dashed red curve. If, however, the lateral stiffness of the jeffcott rotor contained a similar discontinuity as the current working example of the diamond coring system, the radial displacement would suddenly increase when reaching the corresponding rotational speed. To keep a linear model representation, the simplest way of dealing with the sudden shift in radial displacement is to interpret it as an increase in imbalance. In Figure 7.13, the dotted red line marks the corresponding rotor response curve, assuming that the initial imbalance of ten times $\hat{U_0}$ doubles due to the shift in radial displacement. As a result, a rotor with imbalance $10 \cdot \hat{U_0}$ would start the run-up on the corresponding curve (dashed red) and would jump to the response curve of a rotor with $20 \cdot \hat{U_0}$ (dotted red) when reaching the threshold in lateral stiffness. The combined response curve is represented by the solid red line. In this specific case, the rotor would never return to its original configuration once the radial shift (or tilting) has occurred, because even in the overcritical speed range where self-centering occurs, the resulting displacement and therefore the out-of-balance forces

are still above the threshold line of the returning forces. This is exactly what happened in the experiment presented in Figure 7.12, in which the run-up had to be aborted in order not to endanger the structural integrity of the rotor system.

The idea for further experiments on the diamond coring system is to tune the lateral forces so, that during the resonance-crossing, the clamping force of the chuck is exceeded and, at the same time, stays within a reasonable range of elastic bending to ensure the safety of the tool and the human operator. Furthermore, in the overcritical range, the out-of-balance forces shall fall below the threshold line, as indicated by the green and teal curves in Figure 7.13. The question is how the core bit will behave in such a case and whether it will return to its original configuration in the chuck. Even more important than that are the questions of whether the simulation model is capable to correctly represent this strong nonlinear dynamic behavior and whether a commercial standard FEM code is capable of dealing with the rather complex contact situation under rotation. This will be the focus of the next section. As can be expected, the behavior of the real-world diamond-coring system is a little more complicated than the theoretical considerations made above.

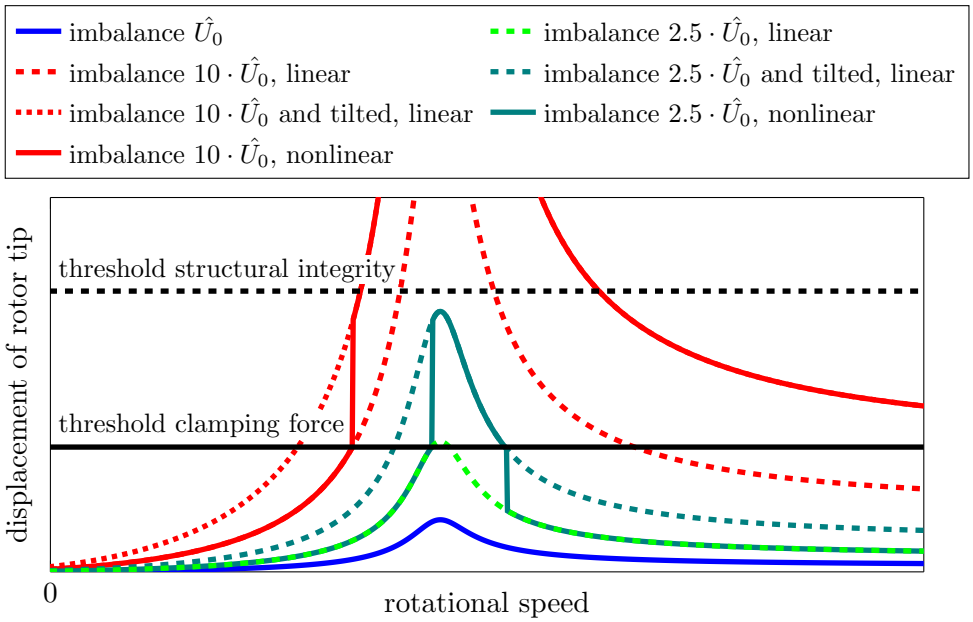

Figure 7.13: Theoretical imbalance response of a Jeffcott rotor with nonlinear lateral stiffness

7.4.3 Mode-Locking Effect

For the following experiments, either the imbalance of the core bit or the tumbling angle of the sleeve, as well as the stiffness and pre-load of the chuck's clamping spring, have been

carefully tuned in such a way that the pre-load will be exceeded upon crossing the first critical rpm, causing the core bit to tilt inside the chuck, as described above. But when leaving the critical speed, the axial force on the chuck is meant to fall below the pre-load of the clamping spring, allowing the chuck to "close" again, thereby returning the core bit to its original position. The idea behind the experiment is to create strong nonlinearities that cause jump-behavior, as described in previous sections, that can act as a test case for the simulation approach. However, it turned out that the core bit "refuses" to return to its original position once the tilting occurred and instead performs a certain relative motion inside the chuck, which allows it to stay in resonance even if the rotational speed no longer matches the natural frequency of the system. This is a phenomenon known only in nonlinear rotordynamics, and which some authors call *mode-locking* [140]. As will be seen, the 3D solid modeling approach is even capable of correctly representing both effects, the tilting of the core bit and the mode-locking. However, before discussing the results, the next paragraph describes a necessary change in the experimental setup.

When deliberately exceeding the clamping force in the chuck during run-up, the line between creating the intended effect and turning the system unstable is very thin. The presence of the sensor support rig constitutes another problem in this context, as it limits the available space for the core bit to deflect laterally. If the core bit touches the rig during operation, the result is a catastrophic failure of the rotor system. Therefore, the measurement setup with the sensor support rig is considered too dangerous for experiments with increased imbalance or increased tumble angles φ. As a consequence, the sensor support rig is removed and the tool is no longer hand-held during the run-up, but is held by a mechanical support, as shown in Figure 4.4 of Chapter 4.1.2. The lasers that measure the core bit motion are placed "on the ground", allowing for a larger distance to the rotating core bit. As a consequence, the lasers now measure the displacement in the inertial reference, instead of the machine coordinate system. Of course, one could always transfer the results into each other, as the movement of the machine is synchronously measured by several accelerometers. However, using absolute coordinates has the advantage that the mode-locking effect shows a better visual appearance in the data, as shall be seen.

7.4.3.1 Mode-Locking Effect Due to Increased imbalance

Figure 7.14 shows, in the familiar plot shape, the relative displacement of the core bit when running through the first critical speed with an added imbalance mass at the core bit tip. Crossing the resonance influences both, the displacement amplitude as well as the rotational

speed of the rotor system. With the help of the simulation model, the data can be interpreted as follows: When the pre-load is exceeded at a certain rotational speed, the rotor is tilting inside the inner piece of the chuck until the radial clearance is used up. The discontinuity in the lateral stiffness, in combination with the sudden increase of rotor imbalance due to the now heavily misaligned core bit, causes a jump in the displacement of the rotor, leading to a large increase in amplitude. Although the electric engine driving the machine is relatively stiff, the sudden rise of the drive shaft's moment of inertia causes the rotational speed to drop significantly due to the principle of conservation of angular momentum. Since the voltage of the electric engine is linearly increased during the run-up, the rotational speed stabilizes and starts to increase again. When the rotational speed is about to exit the resonance area around the critical rpm, the displacement of the rotor slowly starts to decrease and then suddenly collapses, followed by a modulation that slowly dies out with a further increase of the rotational speed. The decreasing lateral rotor displacement leads to a decrease in the moment of inertia, causing the rotational speed to overshoot. The phenomenon of the fluctuating rotational speed during the crossing of a bending resonance is known as the *Sommerfeld Effect* [28] and is caused by the principal of conservation of angular momentum in combination with a nonrigid electric engine. In the case outlined here, the effect is amplified by the tilting of the core bit and by the return into its original position. The sudden collapse of the displacement amplitude happens as planned when the axial force on the connecting pins of the core bit once again becomes small enough for the clamping force to pull it back to its original position. However, the appearance of the modulation is quite surprising and calls for further discussion.

At first glance, the modulation in Figure 7.14 reminds of a known beating phenomenon that occurs when a rotor with gyroscopic behavior is run up through the first critical speed. Figure 7.15 shows the results of an academic example. "The beating phenomenon arises because the gyroscopic effects cause the lowest pair of resonances to split. In steady state, the imbalance excites only the forward-whirling mode; however, during the run-up, the steady state is never achieved, so both modes are excited" [33]. Disregarding the Sommerfeld-Effect, which is neglected in the academic example, the two Figures 7.14 and 7.15 appear to be quite similar, at least in a qualitative way. However, the modulation of the rotor system regarded in the underlying thesis is not caused by mode-splitting but has a different origin.

Due to the tilting, one connecting pin of the core bit is lifted off from its socket in the inner peace of the chuck, as shown in Figure 7.9 for a statical situation. Which of the three pins gets lifted off during operation depends on the angular position of the (artificially increased)

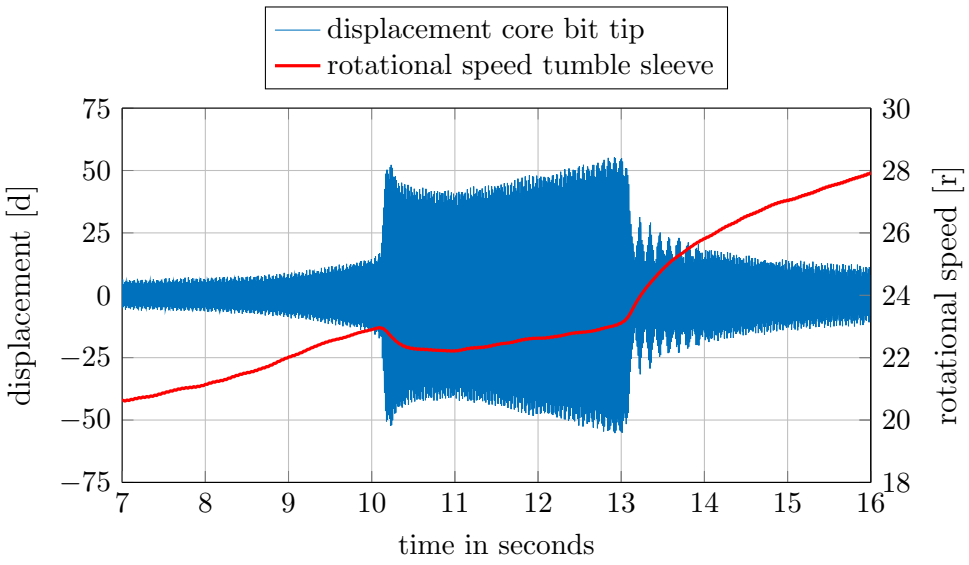

Figure 7.14: [Meas] Vertical displacement of rotor tip relative to housing during slow run-up with additional imbalance mass at core bit tip

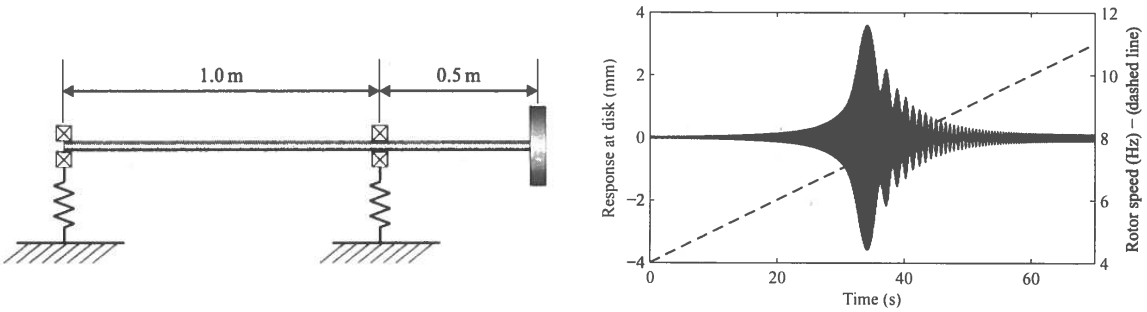

rotor and bearing parameters

shaft diameter	25 mm	mass density	7810 kg/m^3
disk diameter	250 mm	modulus of elasticity	211 GPa
disk thickness	40 mm	Poisson's ratio	0.3
imbalance	10^{-3} kg·m	vertical bearing stiffness	10 MN/m
run-up speed	10 Hz/s	horizontal bearing stiffness	20 MN/m
		bearing damping	400 kNs/m

Figure 7.15: Academic example of a beating phenomenon during run-up of an overhung rotor on anisotropic supports (from [33] with permission of Cambridge University Press)

imbalance. Due to the imbalance excitation, the rotor is in forward whirling motion when approaching the critical rpm, the whirling frequency being equal to the rotational frequency of the drive shaft. During the forward whirling, the drive shaft does not see alternating bending cycles. This means that in a coordinate system that is rotating with the shaft, an observer would see a purely statical bending. The gap between the lifted off connecting pin and its corresponding socket, is not breathing. One could also say, that the whirling frequency of the drive shaft is the same over its entire length. This is changed at a certain rotational speed, marked by the occurrence of the modulation in Figure 7.14, at which the core bit suddenly starts to perform a relative movement inside of the chuck. In a coordinate system that is fixed to the chuck, the core bit starts to perform a backward-whirling motion. This relative motion consist of an elastic bending of the core bit, but also includes a rolling motion of the connecting end inside of the chuck. During that relative backward-whirling, the gap between connecting pin and socket travels tangentially from one pin to the next, in opposite direction of the sense of rotation of shaft and chuck. However, the core bit is not twisting against the chuck. The relative backward-whirling motion of the core bit creates a situation, at which all components of the drive shaft are still rotating at the same rotational speed, but the whirling frequency is no longer the same over the entire length. Shaft and chuck perform a forward-whirling motion with a whirling frequency that is equal to the rotational frequency. In an inertial coordinate system, the motion of the core bit is a combination of the forward-whirling forced by the chuck and the relative backward-whirling inside of the chuck. The relative backward whirling of the core bit appears at a much lower frequency than the forward whirling of shaft and chuck. As a result, the overall motion of the core bit in the inertial frame is still forward-whirling, but at a lower speed than the whirling frequency of shaft and chuck, which is equal to the rotational speed of the drive shaft. In fact, it turns out that the backward-whirling frequency of the core bit relative to the chuck is equal to the difference between the variable rotational frequency of the shaft and the constant natural bending frequency of the whole rotor system. This means that the core bit is still moving with the resonance frequency of the rotor system, although the rotational speed has already increased to a higher level. The combination of the two movements – the rotation of the chuck and the relative backward-whirling motion of the core bit within the chuck – allows the rotor system to stay in resonance, even if the spin speed of the shaft no longer matches the natural bending frequency. The two different whirling frequencies of the different components are the cause for the beating phenomenon, or modulation, as it is called above. In other words: the operational deflection shape adapts to the excitation frequency to stay in resonance. As mentioned before, this phenomenon can be called a

mode-locking effect [140]. The modulation frequency is given by the difference between the constant whirling frequency of the core bit (in the inertial reference) and the increasing rotational frequency of shaft and chuck, therefore increasing likewise. The mode-locking effect is best observable in a Campbell diagram. Figure 7.16 provides the relevant plot of the rotor displacement (measured data), showing the resonance staying on, even when the rotational speed no longer matches the natural frequency of the first bending mode.

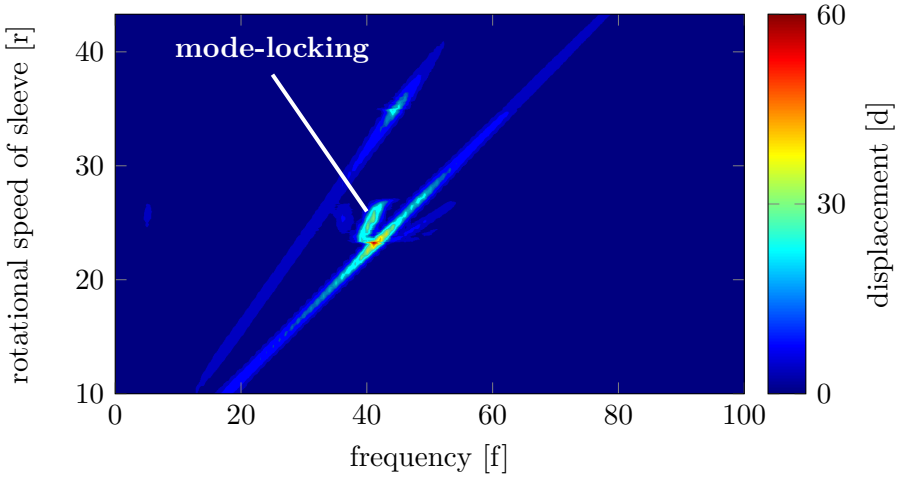

Figure 7.16: [Meas] Campbell diagram of vertical displacement of rotor tip (absolut) during slow run-up with additional imbalance mass at rotor tip

7.4.3.2 Mode-locking effect due to increased tumble angle φ

For the occurrence of the mode-locking effect, it is essential to temporarily exceed the clamping force in the force-locked chuck. In the previous section, the mode-locking effect has been provoked by using an additional imbalance mass at the tip of the core bit. Apart from adding an imbalance to the core bit tip, the clamping force can also be exceeded by increasing the tumble angle φ of the sleeve. As will be seen, this leads to basically the same effect as described in the previous section.

Figure 7.17 shows the results of the experiment in the form of a Campbell diagram, yet as mentioned in the previous paragraph, there are two important differences compared to Figure 7.3. First, the measurements in the current experiment are carried out without the additional sensor test rig. Therefore, the mass and the moment of inertia of the non-rotating part of the system is smaller, resulting in a higher natural frequency of the first bending mode. The second difference to the experiment in Chapter 7.1 is the following: While Figure 7.3 shows the displacement of the rotor tip *relative* to the housing of the

machine, the displacement in Figure 7.17 is measured in an *absolute* coordinate system. This makes the visual appearance of the mode-locking effect much clearer. If the mode-locking effect occurs during run-up, the system stays in resonance, even if the excitation frequency – in this case, the rotational speed of the tumble sleeve – no longer matches the natural bending frequency. In an absolute coordinate system, this effect appears as a vertical line in the Campbell diagram, as can be clearly seen in Figure 7.17. Once the mode-locking occurs and the spin speed is further increased, the speed of the backward-whirling increases likewise – making the backward-whirling frequency the difference between the spin speed of the tumble sleeve and the natural bending frequency of the whole rotor system. The backward-whirling frequency is supposed to appear at the top left of the Campbell diagram as a line parallel to the first order of the sleeve, but with an rpm offset equal to the critical rpm. In Figure 7.17, one can only imagine the line of the backward-whirling, because it is overlaid by low frequency motion resulting from rigid body movement of the machine inside of the support.

Speaking about the influence of the changed support conditions of the machine: Figure 7.17 shows a resonance at around 17 (normalized) Hertz that was not present while the tool was hand-held. This is a resonance of the machine on the mechanical support. The reason why no support resonances have shown up in the Campbell diagram so far, while the system was operated hand-held, is the following: The machine's electric engine cannot operate stably at very low rotational speed, which can also be seen in Figure 7.1. The support resonances of the hand-held machine are below the stable minimum operational speed and are therefore crossed rather fast, whereby no large resonance amplitudes occur. This is why they have not shown up in the Campbell diagram so far. But with the stiffened support, the frequency of a rigid body mode lies close to the stable minimum operational speed, causing comparatively large amplitudes, which can be seen in the lower left of Figure 7.17. However, the structural resonances – caused by the imbalance of the core bit and by the tumbling movement – are left almost unaffected by the changed support conditions, since they are more then two times higher in frequency.

7.4.4 Evaluation of the 3D FE-Simulation

Representing the mode-locking effect and the relative motion between the connecting end of the core bit and the chuck in the simulation model presents a challenge in many ways. First of all, the model must be able to correctly describe the global dynamic system behavior, which is confirmed in Chapter 7.3.

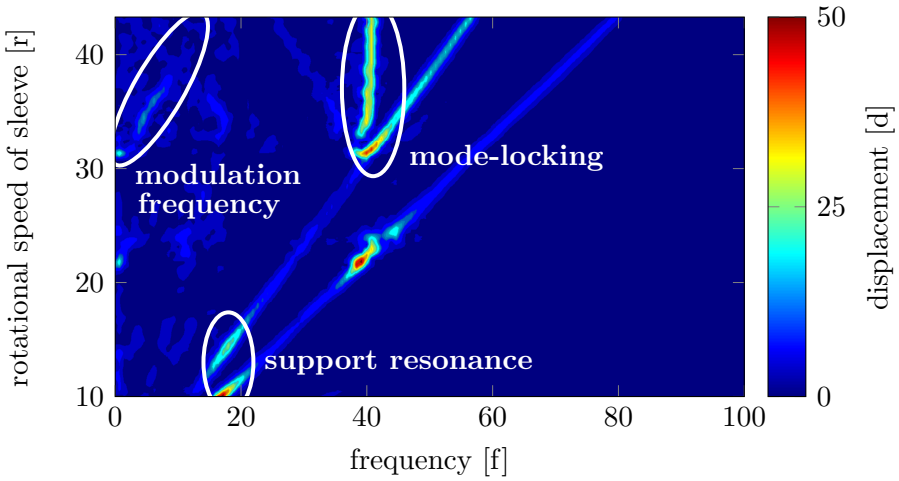

Figure 7.17: [Meas] Campbell diagram of vertical displacement (absolute) of rotor tip during run-up with increased tumble angle φ

Second, an adequate model approach must be found for the connection between chuck and core bit. In the current case, the model of the chuck consists of a mixed approach that contains 3D solid parts of the inner and outer piece, while the disk spring pack is represented by lumped masses and a massless spring using the connector functionality in ABAQUS. Contact definitions are established between the two-piece chuck and the connecting end of the core bit. Implementing the model requires the correct identification of several parameters, like the pre-tension force of the disk spring pack as well as the friction coefficients and damping values in the contact definition.

The third challenge arises from the immense computational effort resulting from the contact algorithms: When the clamping force is exceeded and the core bit performs a relative movement inside the chuck, the real time needed to solve the model for a single run-up almost doubles. This creates a problem insofar as it limits the number of computational cycles that can reasonably be used to improve the quality of the results by updating the model with data obtained in operational measurements.

Especially because of the last point, the model has been developed from the bottom up, meaning that the model representation of single parameters, components or sub-systems have been validated individually to minimize the uncertainty in the model. This rather elaborate approach has now paid off, as the simulation results represent the mode-locking effect well and enables one to study the phenomenon in a detailed way, which would not be possible with solely experimental data. This is due to the fact that the rather small size of the chuck and its high rotational speed during operation simply do not allow one to place

enough and adequate sensors to catch the exact relative movement between the two-piece chuck and the connecting end of the core bit – at least not without changing the system behavior due to the added mass. Due to these limitations in experimental observability of the relative movement between core bit and chuck during the mode-locking effect, a final quality assessment of the simulation model is not a simple task. However, the global behavior – expressed by the displacement of the tip of the core bit, for example – seems to be represented quite well by the model, as will be described in what follows.

Figure 7.18 offers a comparison between the simulation and experiments for the case in which the clamping force is exceeded by added imbalance at the core bit tip. The plot compares rotational speed and the (vertical) displacement of the core bit tip relative to the housing during a run-up with increased imbalance. The simulation model represents the effects that are observable in the measurements well. One criterion to evaluate the quality of the simulation model is the rotational speed at which the pre-load of the chuck is exceeded and the core bit starts to tilt inside the chuck. The tilting in the simulation occurs at the same rotational speed as in the measurements and the modulation in displacement of the core bit due to the relative backward whirling motion is well addressed by the model.

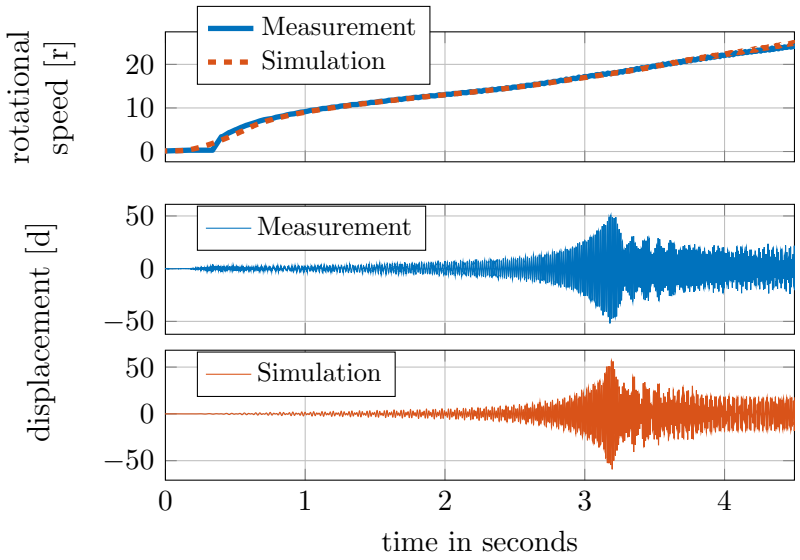

Figure 7.18: Comparison between simulation and experimental results at the core bit tip with additional imbalance mass

However, there are some minor differences between simulation and experiment: The resonance amplitudes are slightly larger in the simulation and the tilting of the core bit occurs more abruptly. The most obvious explanation lies in the model simplification of the pre-loaded disk-spring pack providing the axial clamping force of the chuck. In the model,

the load-displacement curve is idealized by representation in the form of a linear elastic, pre-loaded spring connected to perfectly rigid adjacent bodies. This creates a linear load-displacement curve with a vertical offset in the amount of the pre-load. In reality, however, such a sharp edge in the load-displacement curve does not exist, as indicated for the case of the axial stiffness of the chuck by Figure 5.10, which contains measurements on a compression-tension machine. More uncertainty arises from the friction coefficients, which are taken from the literature according to the combination of materials.

Another reason for discrepancies might be the fact that the FE-model is based on the nominal geometry, while the real-world parts are subjected to tolerance variations. A small variation in either the inner diameter of the inner piece of the chuck or in the outer diameter of the connecting end influences the radial play between the two parts. Due to the nonlinearity of the system, small changes in the range of a few hundreds of a millimeter could lead to observable changes in amplitude.

Other than adding imbalance mass to the core bit, an increase of the tumble angle of the sleeve can also lead to exceeding the clamping force of the chuck. In this case, it makes sense to perform the comparison between simulation and experiments in the frequency domain by using a Campbell diagram. Figure 7.19 shows the simulation results corresponding to the measurement data in Figure 7.17. The plotted physical quantity is the vertical displacement of the core bit tip – this time measured in an absolute coordinate system. Since the simulation is run-up faster at the beginning due to computational resources, the resonances of the supporting stand are crossed so fast that no recognizable amplitudes occur. Apart from that, the simulation results are again in good accordance with the measurements and the mode-locking effect is clearly visible. Differences are a result of the fact that after crossing the resonance, which is caused by the tumble excitation, the amplitudes in the simulation are higher than in the measurements, but the mode-locking fades out faster and terminates at lower rotational speed. Tolerance variations in the geometry of the real parts compared to the nominal shape in the model could be part of the explanation, as mentioned above. Another source for discrepancies could be the friction coefficient used for the contact between the connecting end of the core bit and the coupling, which was taken from the literature according to the combination of materials.

Confidence in the simulation model is further increased when certain marks at the connecting end of the core bit are analyzed after experiments in which mode-looking occurred. During the relative backward-whirling motion, the pins of the connecting end of the core bit are lifted off from the inner piece of the chuck and returned back, according to the whirling. In

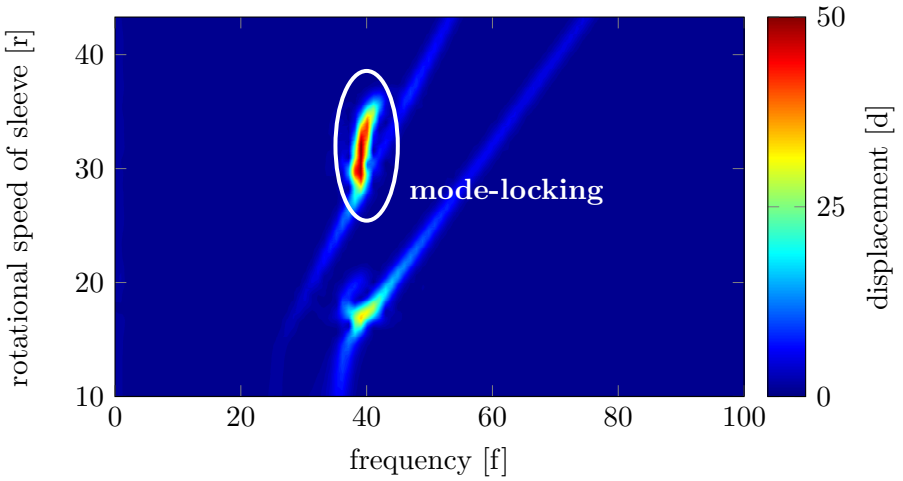

Figure 7.19: [Sim] Campbell diagram of vertical displacement (absolute) of rotor tip during run-up with increased tumble angle φ

doing so and in accordance to the simulation, the pins can eventually hit the chuck during the backward whirling as indicated in Figure 7.20, in which the edge of the pin makes contact with the skew surface of the corresponding socket of the chuck. After the experiment, marks were found at the rotor pins that can only result from the described contact situation. This is a strong indication that the simulation appears to correctly describe the overall system dynamics during the mode-locking effect.

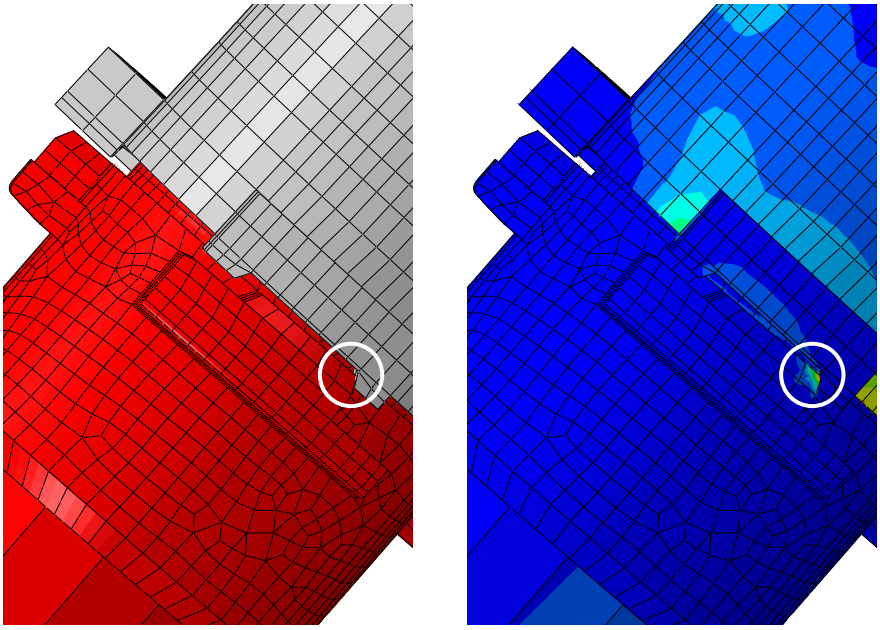

Figure 7.20: Contact situation between core bit and chuck during relative backward whirling

Apart from minor differences between experimental data and simulation, the fact that the

simulation model is capable of describing the relative backward-whirling motion of the core bit inside of the chuck during the mode-locking effect proves the real value of 3D solid modeling against using classical beam models. In the latter, the interface between core bit and chuck needs to be formulated as a three-dimensional joint. The geometry of the parts involved (the connecting end of the core bit and the two-piece chuck), however, is rather complicated, containing lots of slants and chamfers, while, at the same time, the relative motion is a mixture of rolling and sliding, continuously changing the contact situation and constituting highly nonlinear system behavior. This makes it virtually impossible to derive the stiffness and damping matrices describing the interface as a three-dimensional joint in a beam-model in a sufficiently precise manner.

The material behavior in the current simulation model is purely elastic, but could be extended to plastic material behavior at the expense of higher computational costs. A finer mesh at the contact zone would then also be necessary, further increasing computational costs. However, even at the current state, the model is able to represent the complete loss of the core bit during a run-up due to excessively added imbalance or increased tumble angle, thereby creating reacting forces that the system cannot handle anymore. A beam model would not be able to represent this amount of nonlinear behavior. Generally speaking, the stability of the contact algorithms turns out to be astonishing. This creates the possibility to evaluate different variants of interface between core bit and chuck with regard to "fail-safe design" [151] in a fully virtual design loop, using 3D solid modeling.

While the 3D model is capable of representing the nonlinear system behavior between chuck and core bit in the first place, the accompanying effort is quite high. This statement does not only refer to the computational effort that increases dramatically as soon as the clamping force of the chuck is exceeded and relative motion occurs. Since the key to correctly describing the overall system behavior during the mode-locking effect lies in an appropriate model representation of the contact situation between chuck and core bit, the geometry of the parts involved need to be represented with high geometric accuracy. Small slants and chamfers that are usually ignored in the model need to be taken into account in full-scale, thereby significantly increasing the effort of adequately meshing the geometry. Theoretically, it is possible to combine the calculation of the system response and the stress distribution needed for lifetime-calculation into a single simulation run. Practically, the computational effort needed for the current application example is near or maybe even over the edge of what is currently possible with regard to computational resources.

8 Summary and Conclusions

The starting point of the present thesis is the fact that validating the mechanical design of rotating machinery typically requires the creation of two different models to fulfill various tasks: A shaft-line model is still the most common approach to ensure functionality, while lifetime prediction requires a 3D solid FE-model. The current research investigates the question of whether current general purpose FE-codes are capable of performing demanding rotordynamic analyses using a 3D solid modeling approach. The idea behind it is to save the cumbersome creation of an additional shaft-line model and, at the same time, to overcome its limitations in accurate representation of complex rotor geometries in a dynamic analysis. An industrial diamond coring system acts as an application example, providing sophisticated mechanical design and strongly nonlinear behavior. The course of investigation and major findings will be summarized in what follows.

Chapter 2 outlines how rotordynamic effects are represented in the equations of motion and what the impacts are on the computational solution techniques. Generally speaking, rotordynamic analyses can be performed in the frequency and in the time domain. A solution in the frequency domain requires time-independent system matrices and is only possible with linear or linearized systems operating in steady state. Depending on the reference frame, rotordynamic effects are represented by a gyroscopic matrix or by a matrix containing coriolis forces. Since both matrices are unsymmetrical, extracting the eigenvalues and mode shapes requires a complex eigensolver. When solving the equations of motion through direct time integration, efficient algorithms are required containing numerical damping to suppress unphysical high-frequency content in order to keep a reasonably large time increment and to ensure numerical stability. Chapter 2 also addressed the current state of knowledge regarding the use of FEM for rotordynamics, ranging from 1D shaft-line models to 2D axisymmetric elements and full 3D solid modeling. The conclusion is that only 3D solid modeling is capable of accurately representing complex geometry and providing a fully coupled rotordynamic analysis, including geometric nonlinearities such as centrifugal stiffening or spin-softening. General purpose FE-codes nowadays offer extended rotordynamic capabilities by having the necessary element formulations in combination with complex eigensolvers for solutions in the frequency domain, as well as efficient and numerically stable integration schemes for solutions in the time domain. Most programs, however, have acquired those capabilities only quite recently within the last few years, which is the reason why applications are still very limited.

Chapter 3 introduces the industrial diamond coring system, which provides the fundamental hardware to act as an application example within the current research. With regard to rotordynamic analysis, the coring system presents a number of challenges. First, it contains a rather sophisticated mechanical design with complex geometry and many interacting parts involved. It is a two-level rotor system, in which the drive shaft is supported within a hollow sleeve that also rotates. The bore of the sleeve is inclined to its own axis of rotation, forcing the shaft and the core bit not only to perform a spinning motion, but to overlay a tumbling motion to increase drilling performance. Another challenge arises from the fact that the chuck connecting the core bit to the drive shaft is force-locked, allowing for relative movement of the core bit inside the chuck when the clamping force is exceeded during operation. While this cannot happen in the serial configuration of the tool, for the purpose of academic research the system is modified by reducing the clamping-force and by either artificially increasing the imbalance of the core bit or by increasing the amount of tumbling movement. The goal was to intentionally exceed the clamping force during run-up through a bending resonance, which results in strong nonlinear system behavior and, finally, in a mode-locking phenomenon. Further challenges arise from the nonlinear stiffness characteristics of the rolling element bearings and from the fact that the tool is operated hand-held, requiring one to somehow represent the human operator within the model.

Chapter 4 explains the experimental setup to acquire measurement data in order to validate the simulation model. Several three-axial accelerometers record the movement of the tool, while the elastic deformation of the shaft and the tumble sleeve relative to the tool is monitored by inductive sensors. To track the motion of the core bit, the water collector is replaced by a rig supporting four triangulation lasers. When measuring a curved object like the core bit, single spot lasers show relatively strong cross-sensitivity regarding movement perpendicular to their measurement direction. Laser line fork light barriers would be the preferred choice to measure the lateral movement of the core bit, but in the current case they are significantly too heavy for the hand-held measurement setup. The rotational speeds of the different rotor subsystems is recorded by optical encoders in combination with striped tape that is wrapped around the rotating bodies. The main advantage in the current case is that virtually no weight is added to the relatively lightweight rotors and no extra space is needed. The unavoidable measurement error resulting from the discontinuity at the joint of the tape can be corrected in a post-processing operation. In total, up to 60 channels are used, providing a good insight into the dynamic behavior of the diamond coring system.

Chapter 5 introduces the simulation model implemented in ABAQUS. The general approach

is a flexible MBS using 3D solid finite elements for elastic components, point masses containing inertia properties for components behaving rigidly in the frequency range of interest, and elastic joints to represent certain connecting elements. Since high fidelity rotordynamic models are a challenge with regard to computational costs, this approach offers the chance for significant model reduction, while, at the same time, maintaining accuracy where needed. In the current work, only those parts are fully represented by 3D solid finite elements that undergo noteworthy elastic deformation. This includes most of the rotating parts, while the non-rotating parts are represented as point masses with inertia properties. The interaction between certain components is addressed in different levels of detail. In the case of the force-locked chuck, interaction between the connecting end of the core bit and the two-piece chuck is taken into account by fully including the exact geometry in the FE model and by establishing contact definitions between the relevant surfaces. With regard to the disk-spring pack that provides the clamping force, however, there is no need to represent the exact contact situation in full detail. Therefore, it is simply modeled as a discrete pre-loaded spring, where pre-load and spring stiffness are obtained from a static experiment. The same procedure is used for components of the drive train, such as the toothed belts. The deep grove ball bearings are represented likewise as elastic joints, with the difference being that deriving the nonlinear stiffness characteristics is far more complex. First, the compliance of the machine casing supporting the bearings of the tumble sleeve is calculated from a high fidelity FE-sub-model. Next, the exact geometry, such as diameter and curvature of the raceways, is determined on a highly precise tactile measurement machine and another substitute model of the ball bearings is established, including contact between rolling elements and raceways. The geometry is updated by taking into account the deformation of the bearing rings due to the press fit by analytic formulas based on thick ring theory. Finally, the nonlinear stiffness characteristic is calculated by successively applying static loads in all relevant DOFs. This quite elaborate approach allows one to accurately determine the tilting stiffness of the bearings, which presents a challenge for openly available analytical methods. In the current case, the tilting stiffness of the bearings is of increased importance due to the uncommonly high lateral displacement resulting, for instance, from artificially increasing the imbalance of the core bit. Apart from modeling the diamond coring system itself, the simulation must also be capable of representing the human operator holding the tool. Although a vast amount of research and models is available that address the hand-arm system, their use to act as a boundary condition in a simulation like this is rather limited. Openly available models are too soft and neglect the human control behavior. Since the frequency range of interest, the bending resonance occurring during run-up, lies significantly higher than the frequency

range that is strongly affected by added mass and stiffness of the hand-arm system, the human operator is represented by a simple spring-damper system. The parameters are obtained through modal measurements at non-rotating condition, resulting in a model that yields accurate results in the frequency range of interest, but might show significant errors elsewhere, especially at low frequencies. In the current case, this is totally acceptable.

Chapter 6 goes into the details of validating and updating the simulation model in non-rotating condition using the results from modal analysis or FRFs as a criterion for correlation. The model is established from the bottom up, meaning that each component is validated separately in free boundary conditions before assembly. The validation process first consists of a mesh-grid convergence study followed by a comparison to the results of EMA. Geometric and material properties are used to update the model. When components contain very slender geometry, such as the tube of the core bit, small deviations from the nominal geometry might play an important role, even if they are within the specified manufacturing tolerance. Verifying and validating the model from the bottom up significantly reduces the sources of possible deviations when assembling the single components to the whole system. In the further course of validating and updating the model, EMA on the rotor system as a whole is used to identify the damping parameters of the bearings as well as the dynamic properties of the human operator. For the latter, measurements without the operator are compared to measurements when the operator is successively gripping just one of the two handles and, finally, both handles. In general, the results are in good accordance with existing research: The dynamic properties of the human hand-arm system strongly depend on both the frequency range and the specific posture of the operator. Here, the dynamic properties are set so that they match the behavior in the frequency range of interest. Since direct time integration in a high fidelity rotordynamic simulation is computationally very costly, using EMA and FRF-measurements at non-rotating condition can achieve significant cost and time savings in contrast to directly comparing simulation results to operational measurements. One major disadvantage of using EMA or FRF-measurements is that artificially applied excitation forces are typically smaller than operational forces, resulting in possible errors when the system shows nonlinear, or more generally speaking, amplitude-dependent behavior. In such a case, updating the model with operational data might still be necessary.

Chapter 7 finally evaluates the quality of the simulation model by comparing the results of a run-up to measurement data. The diamond coring system has a natural bending mode that needs to be crossed during run-up. The relevant excitation mechanisms are the imbalance of the core bit and the tumbling motion generated by the tumble sleeve. Both excitations

are speed-dependent, and since their rotational speeds stand in a fixed ratio, they cross the bending mode one after the other, creating two resonances when running the tool up or down. Due to the fact that the rotating subsystems are relatively slender, there is no detectable influence of rotation on the natural frequency of the bending mode. Before starting the comparison between simulation and measurements, two more parameters need to be identified to update the model. One is the imbalance of the core bit that arises mainly from misalignment towards the chuck and not from asymmetric mass concentration in the core bit itself, thereby complicating the measurement process on a standard balancing machine. As a consequence, the imbalance is determined *insitu* by adding appropriate balancing weights to the core bit, whereby the correct position can be identified from the large amount of available sensor data. The second parameter obtained from operational measurement data is the drag torque of the bearings, which is identified from coast-down tests. The updated model is then evaluated in two different operational cases: First, in "normal" condition, in which the clamping force is sufficient to hold the core bit in place during run-up, and, second, when the clamping force is intentionally exceeded by reducing the pre-load of the disk-spring pack and by either artificially increasing the imbalance of the core bit or by increasing the amount of tumbling movement. In both cases, the simulation model is capable of accurately representing the dynamic behavior: The resonances occur at the same rotational speeds and with the same amplitudes. In the case in which the clamping force is exceeded, strong nonlinear behavior occurs, resulting in a *mode-locking* phenomenon, in which the core bit performs a relative motion inside the supporting chuck in order to stay in resonance, even if the rotational speed no longer matches the original frequency of the bending resonance. This creates a situation in which all components of the inner rotor subsystem still rotate at the same rotational speed, but the whirling frequency is no longer the same over the entire axial length. The relative motion between core bit and chuck is a combination of sliding and rolling, permanently changing the contact situation. Such a complex interaction with several parts involved requires one to take into account the exact geometry of the interfaces and can only be represented correctly by using 3D solid modeling. The stability of the contact algorithms turns out to be astonishing in this context. However, while the model is capable of representing the nonlinear system behavior between chuck and the core bit in the first place, this comes at the price of significantly increased computational costs and modeling effort when meshing the exact geometry of the interfaces.

Taken together, the considerations above and the good consistency between experimental data and simulation results with regard to the application example lead to the conclusion that general purpose FE codes at their current state are capable of performing challenging

rotordynamic analyses using 3D solid modeling. Today's extended MBS capabilities of such programs offer the chance for significant model reduction, while, at the same, maintaining accuracy where needed. Thus, limitations of classical beam-element models, such as lack of accuracy in mathematical and physical model representation, can be overcome. In the current case, a precise representation of the mode-locking effect and the corresponding interactions within the multi-piece rotor system is simply not possible by using shaft-line models. Another important, if not decisive, advantage of 3D solid modeling is the reuse of already existing CAD-data instead of creating a further model in a manual and cumbersome process. In connection with the current application example, quite a vast number of substitute models was necessary to derive certain parameters. Most of those auxiliary calculations could be performed with the same model that was used for the actual rotordynamic analysis.

Besides investigating the suitability of general purpose FE-codes for rotordynamic analyses, the current thesis was also motivated by the question of whether a 3D solid model can be used to ensure the functionality of a rotor system, while, at the same time, applying a mesh fine enough for accurately calculating the stress distribution as an input for lifetime calculation. In this context, the current work demonstrated limitations of the approach. High fidelity models in rotordynamic simulations generate enormous computational costs when nonlinear characteristics or transient behavior require a solution through direct time integration. With regard to the current application example, using one and the same mesh for a rotordynamic analysis and a lifetime calculation will reach the limit of what is computationally possible at the moment. This would make the approach unsuitable for parameter studies or optimization procedures. As a consequence, it still appears more reasonable to calculate the local stress in an extra (static) analysis. However, when using 3D solid modeling for rotordynamics analyses, performing a lifetime calculation simply requires remeshing and is thus more effective than the classical procedure that needs to set up two different types of models.

Although one can safely assume that computing power will continue to increase in the future, it is still worth thinking about techniques to reduce the model size. An interesting strategy was recently proposed by *Tannous et al.* in [133, 134]. The authors investigate rotor-stator contact in turbines, which requires 3D solid modeling to gain accurate results. The simulation starts with a linear 1D beam-element model and is switched to a nonlinear 3D solid representation once the contact occurs – or slightly before, to be precise, in order to exclude non-linearity. The general idea of switching the model at a certain event could possibly be adapted for the current problem, where exceedance of the clamping force in

the chuck would mark the switching point. However, one should keep in mind the special kinematics of the diamond coring system presented here as an application example: It is a two-level rotor system in which the inner subsystem does not rotate about a principal axis of inertia. This prevents model representation by finite beam-elements, even for operational conditions in which the clamping force is not exceeded. For the same reason, it is out of the question to use a hybrid model in which the rotating parts are represented by beam-elements and only the interface between core bit and chuck is addressed in full detail by 3D continuum finite elements. So, instead of switching from a 1D to a 3D model, in the current case, it might still be possible to start with a model in which the contact definitions are replaced by tie constraints, thereby significantly reducing the number of DOFs.

In the end, it is computational resources that set the limits when using 3D solid modeling for rotordynamic problems. And as computing power has increased significantly since the first use of FEM, so has the problem size and, hence, the demand for it. Today, 3D solid modeling in combination with direct time integration of the underlying force equilibrium equations can solve astonishingly complex problems – but sometimes the process is still "painfully slow" [17].

References

[1] AbuBakar, A.R., Ouyang, H.: Complex eigenvalue analysis and dynamic transient analysis in predicting disc brake squeal. *International Journal of Vehicle Noise and Vibration*, 2(2):143–155, 2006

[2] Adewusi, S., Rakheja, S., Marcotte, P.: Biomechanical models of the human hand-arm to simulate distributed biodynamic responses for different postures. *International Journal of Industrial Ergonomics*, 42(2):249–260, 2012

[3] Adewusi, S., Thomas, M., Vu, V., Li, W.: Modal parameters of the human hand-arm using finite element and operational modal analysis. *Mechanics and Industry*, 15(6):541, 2014

[4] AIAA: Guide for the Verification and Validation of Computational Fluid Dynamics Simulations. Technical Report AIAA-G-077-1998, American Institute of Aeronautics and Astronautics, Reston, VA, USA, 1998

[5] Bachschmid, N., Pennacchi, P., Tanzi, E., Audebert, S.: Transverse crack modeling and validation in rotor systems, including thermal effects. *International Journal of Rotating Machinery*, 9(2):113–126, 2003

[6] Bathe, K.J.: *Finite Element Procedures*. K.J. Bathe, Watertown, MA, 2nd edition, 2014

[7] Bently, D.E., Goldman, P., Yu, J.J.: Full annular rub in mechanical seals, Part II: Analytical study. *International Journal of Rotating Machinery*, 8(5):329–336, 2002

[8] Bently, D.E., Yu, J.J., Goldman, P., Muszynska, A.: Full annular rub in mechanical seals, Part I: Experimental results. *International Journal of Rotating Machinery*, 8(5):319–328, 2002

[9] Blough, J.R.: A survey of DSP methods for rotating machinery analysis, what is needed, what is available. *Journal of Sound and Vibration*, 262(3):707–720, 2003

[10] Bovenzi, M.: Exposure-response relationship in the hand-arm vibration syndrome: An overview of current epidemiology research. *International Archives of Occupational and Environmental Health*, 71(8):509–519, 1998

[11] Brandt, A., Lago, T., Ahlin, K., Tuma, J.: Main principles and limitations of current order tracking methods. *Journal of Sound and Vibration*, 39(3):19–22, 2005

[12] Chatelet, E., D'Ambrosio, F., Jacquet-Richardet, G.: Toward global modelling approaches for dynamic analyses of rotating assemblies of turbomachines. *Journal of Sound and Vibration*, 282(1):163–178, 2005

[13] Chatelet, E., Lornage, D., Jacquet-Richardet, G.: A three dimensional modeling of the dynamic behavior of composite rotors. *International Journal of Rotating Machinery*, 8(3):185–192, 2002

[14] Chen, W.J.: *Practical Rotordynamics and Fluid Film Bearing Design*. Trafford Publishing, 2015

[15] Chen, Y., Yao, G., Jiang, J.: The forward and the backward full annular rubbing dynamics of a coupled rotor-casing/foundation system. *International Journal of Dynamics and Control*, 1(2):116–128, 2013

[16] Childs, D.W.: Rub-induced parametric excitation in rotors. *Journal of Mechanical Design*, 101(4):640–644, 1979

[17] Childs, D.W.: *Turbomachinery Rotordynamics: Phenomena, Modeling, and Analysis*. John Wiley & Sons, New York, 1993

[18] Chung, J., Hulbert, G.M.: A time integration algorithm for structural dynamics with improved numerical dissipation: The generalized-α method. *Journal of Applied Mechanics*, 60(2):371–375, 1993

[19] Combescure, D., Lazarus, A.: Refined finite element modelling for the vibration analysis of large rotating machines: Application to the gas turbine modular helium reactor power conversion unit. *Journal of Sound and Vibration*, 318(4):1262–1280, 2008

[20] Cook, R., Malkus, D.S., Plesha, M.E., Witt, R.J.: *Concepts and Applications of Finite Element Analysis*. John Wiley & Sons, New York, 4$^{\text{th}}$ edition, 2007

[21] Coulomb, C.A.: *Théorie des machines simples: en ayant égard au frottement de leurs parties et à la roideur des cordages*. Bachelier, Paris, 1821

[22] Dassault Systèmes: *ABAQUS Product Documentation: Abaqus Release Notes 6.12*, 2012

[23] Dassault Systèmes: *ABAQUS Product Documentation: Abaqus Analysis User's Guide, Release 6.14*, 2016

[24] Dimond, T., Younan, A., Allaire, P.: A review of tilting pad bearing theory. *International Journal of Rotating Machinery*, 2011(1):1–23, 2011

[25] DIN: Mechanische Eingangsimpedanz des menschlichen Hand-Arm-Systems. DIN 45677:2001, Deutsches Institut für Normung, Berlin, 2001

[26] Dresig, H., Fidlin, A.: *Schwingungen mechanischer Antriebssysteme: Modellbildung, Berechnung, Analyse, Synthese*. Springer, Berlin Heidelberg New York, 2014

[27] Dresig, H., Holzweißig, F.: *Maschinendynamik*. Springer, Berlin Heidelberg New York, 8$^{\text{th}}$ edition, 2012

[28] Eckert, M.: Der Sommerfeld-Effekt: Theorie und Geschichte eines bemerkenswerten Resonanzphänomens. *European Journal of Physics*, 17(5):285, 1996

[29] Ehrich, F.F.: The dynamic stability of rotor/stator radial rubs in rotating machinery. *Journal of Engineering for Industry*, 91(4):1025–1028, 1969

[30] Eschmann, P., Hasbargen, L., Weigand, K.: *Ball and Roller Bearings: Theory, Design and Application*. Oldenbourg, Munich, 2$^{\text{nd}}$ edition, 1985

[31] Ewins, D.J.: *Modal Testing: Theory, Practice, and Application*. Mechanical engineering research studies: Engineering dynamics series. John Wiley & Sons, New York, 2$^{\text{nd}}$ edition, 2000

[32] FAG: *FAG Wälzlager Katalog*, 2014

[33] Friswell, M.I., Penny, J.E.T., Garvey, S.D., Lees, A.W.: *Dynamics of Rotating Machines*. Cambridge Aerospace Series. Cambridge University Press, Cambridge, 2010

[34] Fritz, F.: *Modellierung von Wälzlagern als generische Maschinenelemente einer Mehrkörpersimulation*. Ph.D. thesis, Karlsruher Institut für Technologie (KIT), Germany, 2011

[35] Gasch, R., Nordmann, R., Pfützner, H.: *Rotordynamik*. Springer, Berlin Heidelberg New York, 2006

[36] Genta, G.: Consistent matrices in rotor dynamic. *Meccanica*, 20(3):235–248, 1985

[37] Genta, G.: *Dynamics of Rotating Systems*. Springer, Berlin Heidelberg New York, 2005

[38] Genta, G., Delprete, C., Bassani, D.: DYNROT: A finite element code for rotordynamic analysis based on complex co-ordinates. *Engineering Computations*, 13(6):86–109, 1996

[39] Genta, G., Gugliotta, A.: A conical element for finite element rotor dynamics. *Journal of Sound and Vibration*, 120(1):175–182, 1988

[40] Genta, G., Silvagni, M.: Three-Dimensional FEM Rotordynamics and the So-Called Centrifugal Softening of Rotors. In *Meccanica dei Solidi*, volume 36. Accademia delle Scienze di Torino, 2012

[41] Genta, G., Silvagni, M.: On centrifugal softening in finite element method rotordynamics. *Journal of Applied Mechanics*, 81(1):011001, 2014

[42] Genta, G., Tonoli, A.: A harmonic finite element for the analysis of flexural, torsional and axial rotordynamic behaviour of discs. *Journal of Sound and Vibration*, 196(1):19–43, 1996

[43] Genta, G., Tonoli, A.: A harmonic finite element for the analysis of flexural, torsional and axial rotordynamic behavior of blade arrays. *Journal of Sound and Vibration*, 207(5):693–720, 1997

[44] Géradin, M., Cardona, A.: *Flexible Multibody Dynamics: A Finite Element Approach*. John Wiley & Sons, New York, 2001

[45] Geradin, M., Kill, N.: A new approach to finite element modelling of flexible rotors. *Engineering Computations*, 1(1):52–64, 1984

[46] Girard, A., Roy, N.: *Structural Dynamics in Industry*. John Wiley & Sons, New York, 2010

[47] Göge, D., Sinapius, M., Füllekrug, U., Link, M.: Detection and description of nonlinear phenomena in experimental modal analysis via linearity plots. *International Journal of Non-Linear Mechanics*, 40(1):27–48, 2005

[48] Greenhill, L.M., Bickford, W.B., Nelson, H.D.: A conical beam finite element for rotor dynamics analysis. *Journal of Vibration, Acoustics, Stress, and Reliability in Design*, 107(4):421–430, 1985

[49] Grote, K.H., Feldhusen, J. (editors): *Dubbel: Taschenbuch für den Maschinenbau*. Springer, Berlin Heidelberg, 24$^{\text{th}}$ edition, 2014

[50] Guillaume, P., Verboven, P., Vanlanduit, S., Van Der Auweraer, H., Peeters, B.: A poly-reference implementation of the least-squares complex frequency-domain estimator. In *Proceedings of IMAC*, pp. 183–192. 2003

[51] Guo, Y., Parker, R.G.: Stiffness matrix calculation of rolling element bearings using a finite element/contact mechanics model. *Mechanism and Machine Theory*, 51:32–45, 2012

[52] Hagedorn, P., Heffel, E., Lancaster, P., Müller, P.C., Kapuria, S.: Some recent results on MDGKN-systems. *ZAMM-Journal of Applied Mathematics and Mechanics / Zeitschrift für Angewandte Mathematik und Mechanik*, 95(7):695–702, 2014

[53] Hambric, S.A., Shepherd, M.R., Campbell, R.L., Hanford, A.D.: Simulations and measurements of the vibroacoustic effects of replacing rolling element bearings with journal bearings in a simple gearbox. *Journal of Vibration and Acoustics*, 135(3):031012, 2013

[54] Harris, T.A., Kotzalas, M.N.: *Essential Concepts of Bearing Technology*. Rolling Bearing Analysis. CRC Press, Boca Raton, FL, 5$^{\text{th}}$ edition, 2006

[55] Hilber, H.M., Hughes, T.J., Taylor, R.L.: Improved numerical dissipation for time integration algorithms in structural dynamics. *Earthquake Engineering and Structural Dynamics*, 5(3):283–292, 1977

[56] Horst, H.G., Wölfel, H.P.: Active vibration control of a high speed rotor using PZT patches on the shaft surface. *Journal of Intelligent Material Systems and Structures*, 15(9-10):721–728, 2004

[57] Hughes, T.J.: *The Finite Element Method: Linear Static and Dynamic Finite Element Analysis*. Dover Publications, Mineola, NY, 2012

[58] ISO: Mechanical vibration and shock – Mechanical impedance of the human hand-arm system at the driving point. ISO 10068:2012, International Organization for Standardization, Geneva, Switzerland, 2012

[59] Jacobson, B.: The Stribeck memorial lecture. *Tribology International*, 36(11):781–789, 2003

[60] Jacquet-Richardet, G., Ferraris, G., Rieutord, P.: Frequencies and modes of rotating flexible bladed disc-shaft assemblies: A global cyclic symmetry approach. *Journal of Sound and Vibration*, 191(5):901–915, 1996

[61] Janssens, K., Van Vlierberghe, P., Claes, W., Peeters, B., Martens, T., D'Hondt, P.: Zebra tape butt joint detection and correction algorithm for rotating shafts with torsional vibrations. In *Proceedings of ISMA*, pp. 20–22. 2010

[62] Jones, A.B.: A general theory for elastically constrained ball and radial roller bearings under arbitrary load and speed conditions. *Journal of Fluids Engineering*, 82(2):309–320, 1960

[63] Jones, S.: *Finite element for the analysis of rotor-dynamic systems that include gyroscopic effects*. Ph.D. thesis, Brunel University, London, UK, 2005

[64] Kandil, M.A.: *On rotor internal damping instability*. Ph.D. thesis, Imperial College London (University of London), UK, 2005

[65] Kascak, A.F.: Stability of numerical integration techniques for transient rotor dynamics. Technical Paper 1092, NASA, 1977

[66] Kascak, A.F.: Direct Integration of Transient Rotor Dynamics. Technical Paper 1597, NASA, 1980

[67] Kiesel, T., Marburg, S.: Simulation of mode-locking phenomena in a complex nonlinear rotor system using 3D solid finite elements. *Proceedings of the Institution of Mechanical Engineers, Part C: Journal of Mechanical Engineering Science*, 230(6):959–973, 2016

[68] Kinne, J.: *Praxisnah ermittelte Impedanzverläufe zur Nutzung für biomechanische Modellierungen der beiden menschlichen Hand-Arm-Systeme*. Ph.D. thesis, Technische Universität Darmstadt, Germany, 2008

[69] Kinne, J.: Bestimmung der Leistungsdissipation menschlicher Hand-Arm-Systeme als Voraussetzung für die Beurteilung ihrer Ankopplung an Handmaschinen. Technical Report Gd69, Bundesanstalt für Arbeitsschutz und Arbeitsmedizin, Dortmund, Germany, 2012

[70] Kinne, J., Latzel, K., Melzig-Thiel, R., Schatte, M.: Schwingungstechnische Modellierung der beiden Hand-Arm-Systeme von Bedienpersonen für die Anwendung bei der Prüfung von Handmaschinen. Technical Report F1955, Bundesanstalt für Arbeitsschutz und Arbeitsmedizin, Dortmund, Germany, 2011

[71] Kirchgäßner, B.: Finite elements in rotordynamics. *Procedia Engineering*, 144:736–750, 2016

[72] Kirk, R.G., Gunter, E.J.: Nonlinear transient analysis of multi-mass flexible rotors-theory and applications. Contractor Report CR-2300, NASA, 1973

[73] Kirk, R.G., Gunter, E.J.: Transient response of rotor-bearing systems. *Journal of Engineering for Industry*, 96(2):682–693, 1974

[74] Kleijnen, J.P.C.: Verification and validation of simulation models. *European Journal of Operational Research*, 82(1):145–162, 1995

[75] Knez, L., Slavič, J., Boltezar, M.: A multi-axis biodynamic measuring handle for a human hand-arm system. *Strojniški vestnik-Journal of Mechanical Engineering*, 59(2):71–80, 2013

[76] Krämer, E.: *Dynamics of Rotors and Foundations*. Springer, Berlin Heidelberg New York, 1993

[77] Kraus, J., Blech, J.J., Braun, S.G.: In situ determination of rolling bearing stiffness and damping by modal analysis. *Journal of Vibration and Acoustics*, 109(3):235–240, 1987

[78] Langer, P., Maeder, M., Guist, C., Krause, M., Marburg, S.: More than six elements per wavelength: The practical use of structural finite element models and their accuracy in comparison with experimental results. *Journal of Computational Acoustics*, p. 1750025, 2017

[79] Langer, P., Sepahvand, K., Marburg, S.: Uncertainty quantification in analytical and finite element beam models using experimental data. In *Proceedings of EURODYN*, pp. 2753–2758. 2014

[80] Liew, H.V., Lim, T.C.: Analysis of time-varying rolling element bearing characteristics. *Journal of Sound and Vibration*, 283(3):1163–1179, 2005

[81] Lim, T.C., Singh, R.: Vibration transmission through rolling element bearings, Part I: Bearing stiffness formulation. *Journal of Sound and Vibration*, 139(2):179–199, 1990

[82] Lim, T.C., Singh, R.: Vibration transmission through rolling element bearings, Part II: System studies. *Journal of Sound and Vibration*, 139(2):201–225, 1990

[83] Lim, T.C., Singh, R.: Vibration transmission through rolling element bearings, Part III: Geared rotor system studies. *Journal of Sound and Vibration*, 151(1):31–54, 1991

[84] Lim, T.C., Singh, R.: Vibration transmission through rolling element bearings, Part IV: Statistical energy analysis. *Journal of Sound and Vibration*, 153(1):37–50, 1992

[85] Lindemann, S.: *Model Udating an einem biegeelastischen Rotor*. Ph.D. thesis, Universität Kassel, Germany, 2009

[86] Liong, R.T., Proppe, C.: Finite element multibody simulation of a breathing crack in a rotor with a cohesive zone model. *ISRN Mechanical Engineering*, 2013, 2013

[87] Liu, G.R., Quek, S.S.: *The Finite Element Method: A Practical Course*. Butterworth-Heinemann, Amsterdam, 2nd edition, 2013

[88] Logan, D.L.: *A First Course in the Finite Element Method*. Nelson, Toronto, 4th edition, 2007

[89] Maia, N.M.M., Silva, J.M.M. (editors): *Theoretical and Experimental Modal Analysis*. Engineering dynamics series. Research Studies Press, Baldock, Hertfordshire, 1997

[90] Markert, R.: *Strukturdynamik*. Shaker, Herzogenrath, 2013

[91] Meirovitch, L.: *Analytical Methods in Vibrations*. Macmillan, New York, 1967

[92] Miao, H., Zang, C., Friswell, M.I., Sas, P., Moens, D., Denayer, H.: Model updating and validation of a dual-rotor system. In *Proceedings of ISMA*, pp. 2723–2738. 2014

[93] Moler, C.B., Stewart, G.W.: An algorithm for generalized matrix eigenvalue problems. *SIAM Journal on Numerical Analysis*, 10(2):241–256, 1973

[94] MSC Software Corporation: *MSC NASTRAN Product Documentation: Rotordynamics User's Guide, Release 2016*, 2016

[95] Muszynska, A.: Rotor-to-stationary element sub-related vibration phenomena in rotating machinery: Literature survey. *The Shock and Vibration Digest*, 21(3):3–11, 1989

[96] Muszynska, A.: *Rotordynamics*. Mechanical Engineering. CRC Press, Boca Raton, FL, 2005

[97] Muszynska, A., Bently, D.E., Franklin, W.D., Hayashida, R.D., Kingsley, L.M., Curry, A.E.: Influence of rubbing on rotor dynamics. Technical Report NAS 8-36719, NASA, 1989

[98] Nandi, A.: On computation of response of a rotor in deformed configuration using three-dimensional finite elements. *Communications in Numerical Methods in Engineering*, 19(3):179–195, 2003

[99] Nandi, A., Neogy, S.: Modelling of rotors with three-dimensional solid finite elements. *The Journal of Strain Analysis for Engineering Design*, 36(4):359–371, 2001

[100] Nelson, F.C.: Rotor dynamics without equations. *International Journal of COMADEM*, 10(3):2, 2007

[101] Nelson, H.D.: A finite rotating shaft element using Timoshenko beam theory. *Journal of Mechanical Design*, 102(4):793–803, 1980

[102] Nelson, H.D., McVaugh, J.M.: The dynamics of rotor-bearing systems using finite elements. *Journal of Engineering for Industry*, 98(2):593–600, 1976

[103] N.N.: *ANSYS Product Documentation: ANSYS Release Notes, Release 11.0*, 2007

[104] Oberkampf, W.L., Trucano, T.G., Hirsch, C.: Verification, validation, and predictive capability in computational engineering and physics. *Applied Mechanics Reviews*, 57(5):345–384, 2004

[105] Oberst, S., Lai, J.C.S., Marburg, S.: Guidelines for numerical vibration and acoustic analysis of disc brake squeal using simple models of brake systems. *Journal of Sound and Vibration*, 332(9):2284–2299, 2013

[106] Palmgren, A.: Neue Untersuchungen über Energieverluste in Wälzlagern. *VDI-Berichte*, 20(1):117–121, 1957

[107] Palmgren, A.: Ball and roller bearing engineering. Technical report, SKF Industries Inc., Philadelphia, PA, USA, 1959

[108] Peeters, B., Guillaume, P., Van der Auweraer, H., Cauberghe, B., Verboven, P., Leuridan, J.: Automotive and aerospace applications of the PolyMAX modal parameter estimation method. In *Proceedings of IMAC*, pp. 26–29. 2004

[109] Peeters, B., Van der Auweraer, H., Guillaume, P., Leuridan, J.: The PolyMAX frequency-domain method: A new standard for modal parameter estimation? *Shock and Vibration*, 11(3-4):395–409, 2004

[110] Perinpanayagam, S., Ewins, D.J.: Free-free, fixed or other test boundary conditions for the best modal test. In *Proceedings of IMAC*. 2003

[111] Prabel, B.: Some remarks on time integration of 3D rotor-stator assembly. In *Proceedings of ECCOMAS*, pp. 1–16. 2016

[112] Rakheja, S., Wu, J.Z., Dong, R.G., Schopper, A.W., Boileau, P.É.: A comparison of biodynamic models of the human hand–arm system for applications to hand-held power tools. *Journal of Sound and Vibration*, 249(1):55–82, 2002

[113] Rao, J.S.: *History of Rotating Machinery Dynamics*. Springer Science & Business Media, Dordrecht, 2011

[114] Rao, J.S., Sreenivas, R.: Dynamics of a three level rotor system using solid elements. In *Proceedings of the ASME Turbo Expo 2003, collocated with the 2003 International*

Joint Power Generation Conference, pp. 601–606. American Society of Mechanical Engineers, 2003

[115] Rao, J.S., Sreenivas, R.: Dynamics of asymmetric rotors using solid models. In *Proceedings of the International Gas Turbine Congress*, pp. 2–7. 2003

[116] Rouch, K.E., Kao, J.S.: A tapered beam finite element for rotor dynamics analysis. *Journal of Sound and Vibration*, 66(1):119–140, 1979

[117] Roy, C.J., Oberkampf, W.L.: A complete framework for verification, validation, and uncertainty quantification in scientific computing. In *Proceedings of the 48th AIAA Aerospace Sciences Meeting Including the New Horizons Forum and Aerospace Exposition*, pp. 4–7. 2010

[118] Ruhl, R.L., Booker, J.F.: A finite element model for distributed parameter turborotor systems. *Journal of Engineering for Industry*, 94(1):126–132, 1972

[119] Sato, H.: Free vibration of beams with abrupt changes of cross-section. *Journal of Sound and Vibration*, 89(1):59–64, 1983

[120] Schaller, R.R.: Moore's law: Past, present and future. *IEEE spectrum*, 34(6):52–59, 1997

[121] Schneider, H.: *Auswuchttechnik*. Springer, Berlin Heidelberg New York, 2007

[122] Schwarz, B., Richardson, M.: Proportional Damping from Experimental Data. In *Proceedings of IMAC*, pp. 14–17. 2013

[123] Sepahvand, K., Nabih, K., Marburg, S.: Collocation-based Stochastic Modeling of Uncertain Geometric Mistuning in Bladed Rotor. *Procedia IUTAM*, 13:53–62, 2015

[124] Shang, Z., Jiang, J., Hong, L.: The global responses characteristics of a rotor/stator rubbing system with dry friction effects. *Journal of Sound and Vibration*, 330(10):2150–2160, 2011

[125] SKF: *SKF Wälzlager Katalog - PUB BU/P1 10000/2 DE Januar 2014*, 2014

[126] Stein, E. (editor): *The History of Theoretical, Material and Computational Mechanics-Mathematics Meets Mechanics and Engineering*. Springer, Berlin Heidelberg New York, 2014

[127] Stephenson, R.W., Rouch, K.E.: Modeling rotating shafts using axisymmetric solid finite elements with matrix reduction. *Journal of vibration and acoustics*, 115(4):484–489, 1993

[128] Stephenson, R.W., Rouch, K.E., Arora, R.: Modelling of rotors with axisymmetric solid harmonic elements. *Journal of Sound and Vibration*, 131(3):431–443, 1989

[129] Stölting, H.D.: *Handbuch Elektrische Kleinantriebe*. Hanser, Munich, 2006

[130] Strohschein, D.: *Experimentelle Modalanalyse und aktive Schwingungsdämpfung eines biegeelastischen Rotors*. Ph.D. thesis, Universität Kassel, Germany, 2011

[131] Sunnersjö, C.: Varying compliance vibrations of rolling bearings. *Journal of Sound and Vibration*, 58(3):363–373, 1978

[132] Tandon, N., Choudhury, A.: A review of vibration and acoustic measurement methods for the detection of defects in rolling element bearings. *Tribology International*, 32(8):469–480, 1999

[133] Tannous, M., Cartraud, P., Dureisseix, D., Torkhani, M.: A beam to 3D model switch in transient dynamic analysis. *Finite Elements in Analysis and Design*, 91:95–107, 2014

[134] Tannous, M., Cartraud, P., Dureisseix, D., Torkhani, M.: A beam to 3D model switch for rotor dynamics applications. *Engineering Structures*, 84:54–66, 2015

[135] Taylor, W.: Biological effects of the hand–arm vibration syndrome: Historical perspective and current research. *The Journal of the Acoustical Society of America*, 83(2):415–422, 1988

[136] Thacker, B.H., Doebling, S.W., Hemez, F.M., Anderson, M.C., Pepin, J.E., Rodriguez, E.A.: Concepts of model verification and validation. Technical report, Los Alamos National Lab., Los Alamos, NM, USA, 2004

[137] Tiwari, R., Lees, A.W., Friswell, M.I.: Identification of dynamic bearing parameters: A review. *Shock and Vibration Digest*, 36(2):99–124, 2004

[138] Tran, D.M.: Component mode synthesis methods using interface modes. Application to structures with cyclic symmetry. *Computers and Structures*, 79(2):209–222, 2001

[139] Tran, D.M.: Component mode synthesis methods using partial interface modes: Application to tuned and mistuned structures with cyclic symmetry. *Computers and Structures*, 87(17):1141–1153, 2009

[140] van der Heijden, G.H.M.: Mode-locking in nonlinear rotordynamics. *Journal of Nonlinear Science*, 5(3):257–283, 1995

[141] Vance, J.M., Murphy, B.T., Tripp, H.A.: Critical Speeds of Turbomachinery: Computer Predictions vs. Experimental Measurements, Part I: The Rotor MassElastic Model. *Journal of Vibration, Acoustics, Stress, and Reliability in Design*, 109(1):1–7, 1987

[142] Vest, T.A., Darlow, M.S.: A modified conical beam element based on finite element analysis: experimental correlations. *Journal of Vibration and Acoustics*, 112(3):350–354, 1990

[143] Villa, C., Sinou, J.J., Thouverez, F.: Stability and vibration analysis of a complex flexible rotor bearing system. *Communications in Nonlinear Science and Numerical Simulation*, 13(4):804–821, 2008

[144] Vollan, A., Komzsik, L.: *Computational Techniques of Rotor Dynamics with the Finite Element Method*. CRC Press, Boca Raton, FL, 2012

[145] Wagner, M.B., Younan, A., Allaire, P., Cogill, R.: Model reduction methods for rotor dynamic analysis: a survey and review. *International Journal of Rotating Machinery*, 2010, 2011

[146] Walford, T.L.H., Stone, B.J.: The measurement of the radial stiffness of rolling element bearings under oscillating conditions. *Journal of Mechanical Engineering Science*, 22(4):175–181, 1980

[147] Walford, T.L.H., Stone, B.J.: Some damping and stiffness characteristics of angular contact bearings under oscillating radial load. In *Proceedings of the 2nd International Conference on Vibrations in Rotating Machinery*, pp. 157–162. 1980

[148] Walford, T.L.H., Stone, B.J.: The sources of damping in rolling element bearings under oscillating conditions. *Proceedings of the Institution of Mechanical Engineers, Part C: Journal of Mechanical Engineering Science*, 197(4):225–232, 1983

[149] Weisheit, K., Marburg, S.: Calculation of the Response of a Periodically Excited Beam with Frictional Contact Using Harmonic Balance Method. *Procedia IUTAM*, 19:282–288, 2016

[150] Welcome, D.E., Dong, R.G., Xu, X.S., Warren, C., McDowell, T.W., Wu, J.Z.: An examination of the vibration transmissibility of the hand-arm system in three orthogonal directions. *International Journal of Industrial Ergonomics*, 45:21–34, 2015

[151] Wissner, C.: *Beiträge zum Fail-Safe-Design*. Ph.D. thesis, Karlsruher Institut für Technologie (KIT), Germany, 2010

[152] Wittel, H., Muhs, D., Jannasch, D., Voßiek, J.: *Roloff/Matek Maschinenelemente: Normung, Berechnung, Gestaltung*. Springer Vieweg, Wiesbaden, 21st edition, 2013

[153] Yu, J.J., Goldman, P., Bently, D.E., Muzynska, A.: Rotor/seal experimental and analytical study on full annular rub. *Journal of Engineering for Gas Turbines and Power*, 124(2):340–350, 2002

[154] Ziegler, H.: *Mechanik: Dynamik der Starren Körper und Systeme*. Springer, Basel, 2013

[155] Zorriassatine, F., Wykes, C., Parkin, R., Gindy, N.: A survey of virtual prototyping techniques for mechanical product development. *Proceedings of the Institution of Mechanical Engineers, Part B: Journal of Engineering Manufacture*, 217(4):513–530, 2003

A Appendix

Table A.1: Brief review of capabilities of FE-methods to model a rotating shaft-disc system [98]

	-			prismatic solid or hollow cross-section		tappered			abrupt change in cross-section	
	rotary inertia	gyroscopic effect	shear deformation	axial-symmetric	2 principal axes	solid, axial-symmetric	2 principal axes	hollow, axial-symmetric	axial-symmetric	non-axial-symmetric
Rayleigh shaft element	✓	✓	✗	✓	✓	✗	✗	✗	✗	✗
Conical shaft element based on Timoshenko beam	✓	✓	✓	✓	✗	✓	✗	✗	✗	✗
Modulus corrected elements	✓	✓	✓	✓	✓	✓	✓	✓	✓	✗
Axial-symmetric finite element	✓	✓	✓	✓	✗	✓	✗	✓	✓	✗
3D solid FEM	✓	✓	✓	✓	✓	✓	✓	✓	✓	✓